Australian National University

III-V Compound Semiconductor Nanowire Terahertz Detectors

Kun Peng

December 2016

A THESIS SUBMITTED FOR THE DEGREE OF DOCTOR OF PHILOSOPHY OF THE AUSTRALIAN NATIONAL UNIVERSITY

Department of Electronic Materials Engineering

Research School of Physics and Engineering

College of Physical and Mathematical Sciences

The Australian National University

Declaration

This thesis, to the best of my knowledge, does not contain any materials previously published by another person or submitted for a degree or diploma at any university except where specific reference is made in the text.

Kun Peng

December 2016

Acknowledgements

First of all, I would like to express my sincere gratitude to all my supervisors, collaborators and colleagues. This thesis would not have been possible without their continuous support, help and guidance.

Specifically, I would want to thank my supervisors: Prof. Chennupati Jagadish and Prof. Hark Hoe Tan. They are the most supportive mentors. Their insightful comments and encouragement on my research and my personal career have been priceless. I particularly appreciate Jagadish for having trust in me and supporting me to visit to Oxford for my PhD study.

The greatest thanks go to my primary supervisor: A/Prof. Lan Fu. Words cannot express how grateful I am to her for offering me the opportunity to join Jagadish's Group. I would like to thank her for teaching me in all the time of my research as well as taking care of me. She is like family to me. I really want to express my appreciation for her generosity in support of my research and my overseas visits.

Special thanks go to my supervisor: Dr. Patrick Parkinson. He is a dedicated supervisor, who always provides me with insightful questions and invaluable advice on my project. I would like to thank him for always being there for me, for being patient with my work and for allowing me to grow as a research scientist.

Also, I would like to express my thanks to my UK collaborators: Prof. Michael B. Johnston and his terahertz photonics group (including Dr. Hannah Joyce, Dr. Rebecca Milot, Dr. Marco Zerbini, Dr. Callum Docherty, Dr. Mingzhen Liu, Ms. Jessica Boland, Mr. Christopher Davies, Mr. Adam Wright, etc.) as well as Prof. Laura Herz and her semiconductors group (including Dr. Christian Wehrenfennig, Dr. Chris Menelaou, Ms. Juliane Gong, Ms. Elisabeth Parrott, Mr. Jay Patel, Mr. Waqaas Rehman, etc.) in the University of Oxford. I have visited Oxford twice during my PhD. If I missed anyone's name in this acknowledgement, I hope she/he would not mind. It is a very precious and enjoyable experience working with these brilliant people and learning from them. I especially want to thank Prof. Michael B. Johnston. In a sense, he is also one of my supervisors, who taught me about the terahertz time-domain spectroscopy technique and spent time with me on my experiments, data analysis and writing.

In addition, I would want to acknowledge my collaborators in the Australian National University (including Dr. Qiang Gao, Dr. Sudha Mokkapati, Dr. Philippe Caroff, Dr. Ziyuan Li, Dr. Nian Jiang, Dr. Ya-Nan Guo, Dr. Fan Wang, Dr. Qian Gao, Mr. Yesaya C. Wenas, Mr. Zhe Li, Dr. Xiaoming Yuan), colleagues (including Dr. Aruni Fonseka, Dr. Amira Ameruddin, Dr. Dhruv Saxena, Mr. Tim Burgess, Ms. Bijun Zhao, Mr. Naiyin Wang, Mr. Parvathala Reddy and all other younger PhD, Masters and Honours students in the Research School of Physics and Engineering) and staffs (including Prof. Robert Elliman, A/Prof Jennifer Wong-Leung, Prof. Jiandong Ye, A/Prof. Fangfang Ren, Dr. Fouad Karouta, Dr. Kaushal Vora, Dr. Li Li, Dr. Mykhaylo Lysevych, Dr. Naeem Shahid, Dr. Xinjun Liu, Mr. Dennis Gibson, Mr. Joshua Carr, etc.). I would like to thank them for their useful discussion and generous help. Without them, I would not have been able to get through the difficult times. I wish we could collaborate again in the future.

Moreover, I would like to extend my sincerest thanks to our lovely administrators in the Australian National University: Ms. Julie Arnold, Ms. Karen Nulty and Ms. Liudmila Mangos, who are the most warm-hearted administrators in the world. They have incredible patience to students (particularly to the international students like me), and always prioritise the students' needs above anything else.

Finally, I would like to address my endless gratitude to my parents, some close relatives and friends. I'm a lucky person, who has been loved a lot. I cannot thank my parents enough for all the sacrifices that they have made for me. As their only child, my parents never stopped me from perusing my dream. They unconditionally supported me to continue my study in Australia. Even it means that I have to be thousands of miles away from them. I would like to deeply thank my two elder cousins (Jie Peng and Fang Peng), who always inspire me to strive towards my goals, and encourage me to see the world. Also, I would want to thank my aunts and uncles for their loves. At the end, I would want to give my big thanks to some important friends: Qian Gao, Tian Wang, Fan Cheng and Cuijie Yuan. They know me well and have shared the ups and downs of my research. Another reason for me able to complete this thesis is that they all have a faith in me. Thanks for the supports!

Abstract

III-V semiconductor nanowires have emerged over the past decade as promising nano-components for future electronic and optoelectronic devices and systems, including field-effect transistors, light-emitting diodes, photodetectors, lasers and solar cells. Recently, III-V semiconductor nanowires have been considered as ideal candidates for photoconductive terahertz (THz) detection, as they possess many desirable properties, such as a direct and tunable band gap, good carrier mobility and short carrier lifetime (on the picosecond to nanosecond timescale). Due to the one-dimensional structure and nanoscale size, such III-V nanowire THz detectors are promising as building blocks for advanced THz systems with compact configuration and enhanced functionalities (i.e. sub-wavelength resolution and high polarisation sensitivity).

This dissertation presents the first attempt to examine the suitability of III-V semiconductor nanowires for their applications as photoconductive THz detectors. At first, a series of GaAs/AlGaAs core-shell nanowires were grown (using Au-catalyst metalorganic vapour phase epitaxy technique), characterised and compared for selection to detect the THz signal in a THz time-domain spectroscopy (THz-TDS) system. The fabricated GaAs/AlGaAs single nanowire THz detectors exhibited a pA-level THz response with good signal-to-noise ratio and high polarisation sensitivity however a narrow detection bandwidth (in the range of 0.1-0.6 THz). The origin of the narrow bandwidth for single nanowire detectors was thoroughly investigated using finite-difference time-domain (FDTD) simulations, revealing that the limited bandwidth arose from the strong low frequency resonance caused by the specific device geometry design (rather than the nanowire itself). By adjusting and optimising the nanowire detector geometry, broadband (0.1-1.6 THz) GaAs/AlGaAs single nanowire THz detectors were demonstrated. Furthermore, due to the nanoscale active material fabricated on an insulating substrate (z-cut quartz), single nanowire photoconductive THz detectors showed a very low dark current and a resultant low-noise nature when compared with the traditional (bulk) photoconductive THz detectors. This relaxes the ultra-short carrier lifetime requirement for the (semiconductor) detection material for photoconductive THz detection, since in traditional photoconductive detector the detection material has to have a carrier lifetime of a few picoseconds to minimise

the noise current. Therefore, nanowires with longer carrier lifetime can also be used for photoconductive THz detection. Based on above findings, the high-quality core-only InP nanowires (grown by selective-area metalorganic vapour phase epitaxy technique) were investigated for photoconductive THz detection. With previously optimised device geometry and superior optoelectronic properties of InP nanowires, InP single nanowire THz detectors were fabricated and found to exhibit a broadband response (0.1-2.0 THz) and excellent sensitivity, which were then used to measure the transmission spectra for real material characterisation with performance comparable to the traditional (bulk) detectors. A longer time-domain sampling window (compared to the traditional bulk detectors) and thus a higher spectral response resolution were obtained for the InP single nanowire THz detectors, which have been ascribed to the small active material volume and thick THz-transparent z-cut quartz substrate, enabling the single nanowire detector to have less Fabry-Pérot reflections in measured signal. Furthermore, it was found that the contact quality significantly affects THz detector performance and is particularly crucial for the performance and reliability of single nanowire detectors due to their large surface-to-volume ratio. In the final part of this work, an axial n^+-i-n^+ InP nanowire structure was designed and investigated for use in nanowire THz detectors. The improved contact quality (due to contact doping) has led to further improvement of the nanowire THz detector performance particularly in its signal-to-noise ratio.

In summary, this thesis demonstrates a series of photoconductive THz detectors fabricated from different III-V semiconductor nanowire materials and structures, showing excellent bandwidth and sensitivity, approaching that of the conventional THz detectors. The nanowire device design, fabrication, characterisation and related optical simulations described in this work have provided deep insights into the characteristics of the single nanowire THz detectors, which may serve as a useful guidance for future development of nano-device based THz systems.

Publications

Journal Papers

[1] K. Peng, P. Parkinson, Q. Gao, J. L. Boland, Z. Li, F. Wang, S. Mokkapati, L. Fu, M. B. Johnston, H. H. Tan and C. Jagadish, 'Single n^+-i-n^+ InP nanowires for highly sensitive terahertz detection'. Nanotechnology, vol. 28, 125202, 2017.

[2] K. Peng, P. Parkinson, J. L. Boland, Q. Gao, Y. C. Wenas, C. L. Davies, Z. Li, L. Fu, M. B. Johnston, H. H. Tan, and C. Jagadish, "Broadband phase-sensitive single InP nanowire photoconductive terahertz detectors," Nano Letters, vol. 16, pp. 4925-4931, 2016.

[3] K. Peng, P. Parkinson, L. Fu, Q. Gao, N. Jiang, Y.N. Guo, F. Wang, H.J. Joyce, J.L. Boland, H.H. Tan, C. Jagadish, M.B. Johnston, 'Single nanowire photoconductive terahertz detectors'. Nano Letters, vol. 15, pp. 206-210, 2015.

[4] F. Wang, Q. Gao, K. Peng, Z. Li, Z.Y. Li, Y.N. Guo, L. Fu, L.M. Smith, H.H. Tan, C. Jagadish, 'Spatially resolved doping concentration and nonradiative lifetime profiles in single Si-doped InP nanowires using photoluminescence mapping'. Nano Letters, vol. 15, pp. 3017-3023, 2015.

[5] Z. Zhong, Z. Li, Q. Gao, Z. Li, K. Peng, L. Li, S. Mokkapati, K. Vora, J. Wu, G. Zhang, Z. Wang, L. Fu, H. H. Tan, and C. Jagadish, 'Efficiency enhancement of axial junction InP single nanowire solar cells by dielectric coating,' Nano Energy, vol. 28, pp. 106-114, 2016.

[6] Z. Li, X. Yuan, L. Fu, K. Peng, F. Wang, X. Fu, P. Caroff, T. P. White, H.H. Tan, C. Jagadish, 'Room temperature GaAsSb single nanowire infrared photodetectors,' Nanotechnology, vol. 26, 445202, 2015.

Conference Papers

[1] K. Peng, P. Parkinson, Q. Gao, J. L. Boland, Z. Li, F. Wang, Y. C. Wenas, C. L. Davies, L. Fu, M. B. Johnston, H. H. Tan, C. Jagadish, 'Broadband single-nanowire photoconductive terahertz detectors,' CLEO Laser Science to Photonic Applications: 2017, San Jose, California, USA.

[2] K. Peng, P. Parkinson, Q. Gao, J. L. Boland, Z. Li, F. Wang, S. Mokkapati, L. Fu, M. B. Johnston, H. H. Tan and C. Jagadish, ‘Single n-i-n InP nanowires for improved terahertz detection,’ Conference on Optoelectronic and Microelectronic Materials and Devices 2016, Sydney, NSW, Australia.

[3] K. Peng, J. L. Boland, Q. Gao, Y. C. Wenas, C. L. Davies, Z. Y. Li, P. Parkinson, L. Fu, M. B. Johnston, H. H. Tan and C. Jagadish, ‘Broadband single-InP-nanowire photoconductive terahertz detectors,’ International Conference on Nanoscience and Nanotechnology 2016, Canberra, ACT, Australia.

[4] K. Peng, P. Parkinson, L. Fu, Q. Gao, N. Jiang, F. Wang, Y.N. Guo, Y. C. Wenas, H. J. Joyce, J. L Boland, M. B. Johnston, H. H. Tan and C. Jagadish, ‘Single GaAs/AlGaAs nanowire photoconductive terahertz detectors with tunable bandwidth,’ 2015 Materials Research Society Fall Meeting & Exhibit, Boston, Massachusetts, USA.

[5] K. Peng, P. Parkinson, L. Fu, Q. Gao, N. Jiang, Y.N. Guo, F. Wang, H. J. Joyce, J. L. Boland, M. B. Johnston, H. H. Tan and C Jagadish, ‘Single nanowire terahertz detectors with tunable bandwidth,’ Australian National Fabrication Facility 2015 Annual Research Showcase Program, Brisbane, QLD, Australia.

[6] K. Peng, P. Parkinson, L. Fu, Q. Gao, N. Jiang, Y.N. Guo, F. Wang, H. J. Joyce, J. L. Boland, M. B. Johnston, H. H. Tan and C Jagadish, ‘Single nanowire terahertz detectors,’ CLEO Laser Science to Photonic Applications: 2015, San Jose, California, USA.

[7] K. Peng, P. Parkinson, L. Fu, Q. Gao, N. Jiang, Y.N. Guo, F. Wang, H. J. Joyce, J. L. Boland, M. B. Johnston, H. H. Tan and C Jagadish, ‘Single GaAs/AlGaAs-nanowire photoconductive terahertz detectors,’ Conference on Optoelectronic and Microelectronic Materials and Devices 2014, Perth, WA, Australia.

[8] K. Peng, P. Parkinson, L. Fu, Q. Gao, F. Wang, Y.N. Guo, Y. C. Wenas, H. J. Joyce, M. B. Johnston, H. H. Tan and C. Jagadish, ‘Single nanowire terahertz detectors,’ 8th Advanced Materials Processing 2014, Gold Coast, QLD, Australia.

List of Acronyms and Symbols

AC	alternating-current
AsH_3	arsine
CW	continuous-wave
DC	direct-current
DLWL	direct-laser writing lithography
DR	dynamic range
EBL	electron beam lithography
FDTD	finite-difference time-domain
I-V	current-voltage
LT-GaAs	low-temperature GaAs
MOCVD	metalorganic chemical vapour deposition
MOVPE	metalorganic vapour phase epitaxy
OPTP	optical pump-terahertz probe
PCA	photoconductive antenna
PL	photoluminescence
SAE	selective area epitaxy
SA-MOVPE	selective-area metalorganic vapour phase epitaxy
SEM	scanning electron microscopy
Si	silicon
SI-GaAs	semi-insulating GaAs
SiH_4	silane
SNR	signal-to-noise ratio
TEM	transmission electron microscopy
THz	terahertz
THz-TDS	terahertz time-domain spectroscopy
TMAl	trimethylaluminium
TMGa	trimethylgallium

TMIn	trimethylindium
TRPL	time-resolved photoluminescence
UV	ultraviolet
VLS	vapour-liquid-solid
WZ	wurtzite
ZB	zinc-blende

List of Figures

List of Tables

Table of Contents

Chapter 1

Introduction

Terahertz (THz) radiation [1], also known as T-ray or sub-millimetre radiation, covering the frequency range between infrared light and microwaves (as shown in Figure 1.1), is known for its unique transmission properties with non-ionising and non-invasive nature. In the past, the lack of traditional materials for THz generation and detection hindered the development of THz research and applications. In the mid-1970s, the advent of femtosecond lasers accelerated advances in electronics and photonics fields, providing new materials and devices that made the THz gap widely accessible [2, 3]. This has led to an increasing interest in THz spectroscopy and imaging [4], as they have proven to be useful tools for a broad range of applications, including materials characterisation [5], biological and medical imaging [6], product inspection [7], homeland security [8] and environmental monitoring [9]. Moreover, over the last few years, THz communication has provided a high data rate option to go beyond 100 Gbps. Research interests have been focused on investigation of THz photonics and electronics for THz band communication [10], particularly designed to support compact wireless technology. As such, there is a growing demand in further developing THz materials and devices for more advanced THz applications.

THz time-domain spectroscopy (THz-TDS) is one of the most powerful THz techniques, which has developed from being a laboratory-based technique to finding a number of industrial and commercial applications [11-15] in the last twenty years, particularly in materials characterisation. As part of this development, photoconductive (Auston-type [16]) THz emitter and detector technology has advanced via the introduction of ion-damaged [17] or low-temperature grown [18] semiconductor materials, which possess specific properties including fast photoconductivity rise times, short carrier lifetimes and high carrier mobilities, and complex antenna geometries [19] for broadband operation. However, the manufacture of photoconductive emitters or detectors remains limited, owing to the challenges associated with the production of semiconductors that exhibit above desirable optoelectronic properties.

Besides, current THz-TDS techniques present many difficulties for miniaturisation due to the constraints posed by sub-millimetre wavelengths. To overcome this limitation, near-field THz spectroscopy and on-chip THz spectrometer have been proposed [20, 21], which could lead to nanoscale resolution of the system. One way to develop simple, low-cost, highly integrable emitter and detector structures for high-resolution THz-TDS applications is through the use of quasi-1D semiconductor nanowires [22] as the active elements.

III-V compound semiconductors [23-26] have been widely used as the active material for photoconductive THz emitters and detectors in THz-TDS, owing to their low cost (compared to the electro-optic materials [27, 28]) and wide material availability [16]. One-dimensional III-V semiconductor nanowires maintain many superior properties as their bulk counterparts, such as high carrier mobilities (approximate or equal to that in bulk materials [29]) and a direct and tunable band gap. In addition they have shorter carrier lifetimes (typically sub-nanosecond [29, 30]) due to the intrinsically large surface to volume ratio, and thus have been considered as ideal alternatives to traditional III-V semiconductors for use as THz frequency components. Furthermore, the nano-size dimensions and ability to grow on silicon substrates of III-V semiconductor nanowires indicate a promising prospect for their integration with CMOS electronics to realise complex, highly-integrated THz systems [31].

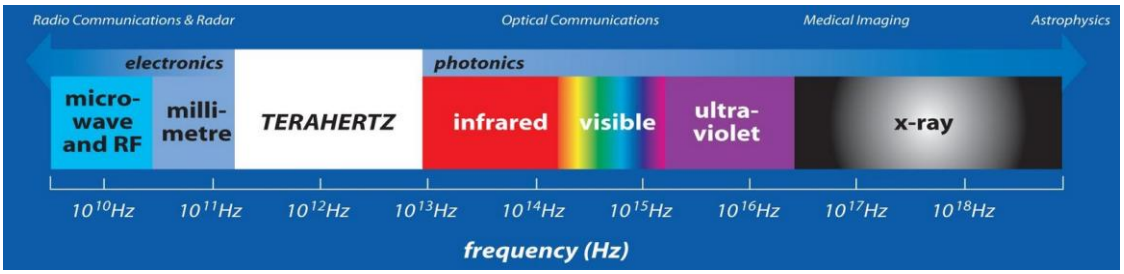

Figure 1.1: The electromagnetic spectrum.
(from http://terahertztechnology.blogspot.com.au/2013_10_01_archive.html).

1.1 III-V Compound Semiconductor Nanowires for Device Applications

To date, the maturity of various approaches for III-V semiconductor nanowire synthesis has enabled researchers to produce a wide range of nanowire materials and structures, including

core/shell, superlattice and branched structures with the desired composition, morphology and electrical properties through specific dopants incorporation and fine tuning of growth parameters. This largely extends the flexibility and functionality of nanowire-based electronic, optoelectronic and photovoltaic devices [32, 33]. In 2011, high-speed nanoscale electronic devices (both nanowire field-effect transistors and light-emitting diodes) were demonstrated for the first time using InP nanowires [34]. Subsequently, high-performance InAs/InP core-shell single nanowire field-effect transistors were reported with electron mobility reaching to 11500 cm^2/Vs at room temperature [35]. In 2013, GaN-based nanowire light-emitting diodes with industry-standard quality had been achieved and were ready to reach market [36]. In the same year, a 13.8% efficient axial p-i-n InP nanowire solar cell was demonstrated [37], while GaAs-based nanowires were shown to lase at room-temperature [38]. Most recently, InP nanowire lasers [39], GaAs/AlGaAs multiple quantum well nanowire lasers [40] and a 15.3% efficiency p-n junction GaAs nanowire array solar cell [41] were reported. The significant development of III-V nanowire synthesis, property manipulation and device fabrication over the last ten years has proven the potential of III-V semiconductor nanowires as nano-building blocks for advanced integrated electronics and optoelectronics. Therefore, it is possible to design and grow III-V nanowires, and fabricate them into nano-THz-electronics to realise advanced THz systems. For example, a single nanowire THz detector can be used as a sub-wavelength detector element for near-field imaging [42], or integrated into an “on-chip” THz spectrometer [43, 44] avoiding the need for complex optical arrangements.

1.2 III-V Compound Semiconductor Nanowires for Terahertz Applications: Advantages and Challenges

III-V nanowires have been employed for THz applications for both THz emission and detection. In 2011, single InAs nanowires were reported as nanoscale source for THz radiation [45, 46]. In 2013 and 2015 respectively, plasma-wave THz detectors based on InAs and InAs/InSb single nanowire field-effect transistors were demonstrated and exploited for THz imaging [47-49]. However, to date, semiconductor nanowires have not been incorporated into the THz-TDS technique [50] for spectroscopic detection applications (which can provide both

amplitude and phase information of the measured THz signal), partly due to challenges in materials design and nanowire-based device fabrication.

It is known that semiconductors for photoconductive THz detection require having both ultra-short charge carrier lifetime and reasonable carrier mobility, where a compromise needs to be reached to ensure a sufficient response level while minimising current noise. To achieve these properties in traditional (bulk) semiconductors, low-temperature growth by molecular beam epitaxy [51, 52] and/or post-growth processing steps, such as ion-implantation and annealing [53, 54], have to be used. The low yields and challenges in reproducibility of low-temperature growth as well as complicated multiple-step fabrication procedures give researchers a motivation to further explore advanced semiconductor materials and structures for photoconductive THz detection. III-V semiconductor nanowires offer many desirable material properties: a direct and tunable band gap, good carrier mobility close to that of bulk materials [29], and short carrier lifetime on the picosecond to nanosecond timescale [30] which can be adjusted by controlling the crystal quality [55] or surface state density [30, 56, 57]. Therefore, using III-V nanowires for photoconductive THz detection could avoid additional material processing steps after crystal growth, as well as the high yield of III-V nanowires grown on a standard wafer suggests a possible high yield of nanowire-based devices, advantageous in both reduced material cost and complexity. Moreover, due to their one-dimensional structure and nanoscale size, nanowires exhibit great promise for highly compact THz systems.

The challenges on the development of such III-V single nanowire photoconductive THz detectors include: (1) producing reliable III-V nanowires with desired properties for optimal THz detection (i.e. low dark current, high carrier mobility and short carrier lifetime); (2) forming low-noise and low-resistance contacts; (3) optimising device geometry to increase THz signal coupling and detection sensitivity; (4) incorporating nanowire-based detectors into the standard THz-TDS system with precise alignments for device testing.

1.3 Outline of the Thesis

This dissertation presents a detailed investigation on design, fabrication, characterisation and

optimisation of photoconductive THz detectors using III-V single nanowires, which has not been reported previously. Fundamentals of THz systems and techniques used in this thesis are introduced in Chapter 2. Details of the experimental and simulation methods are presented in Chapter 3. Chapter 4 demonstrates photoconductive THz detectors using single GaAs/AlGaAs core-shell nanowires as the active component, verifying the suitability of III-V nanowires for THz-TDS applications. A series of GaAs/AlGaAs core-shell nanowires produced under different growth conditions via the vapour-liquid-solid (VLS) growth [58] using metalorganic vapour phase epitaxy (MOVPE) technique were studied, and selected for optimised THz detection. Finite-difference time-domain (FDTD) simulations in THz regime are performed, indicating that a reduced response bandwidth (in the range of 0.1-0.6 THz) of the single nanowire detector arises from the resonance characteristics of the specific detector geometry (rather than the nanowire itself). Relationships between device geometry and its resonance characteristics are further studied in detail using FDTD simulations in Chapter 5. Significantly, by tailoring the detector electrode design, GaAs/AlGaAs single nanowire photoconductive THz detectors with tunable response bandwidth can be achieved. Other factors (such as THz polarisation and capping layer of the core-shell nanowire structure) that affect the detector response characteristics are also discussed. In Chapter 6, a performance-improved photoconductive THz detector developed from single InP nanowires is introduced. Unlike GaAs/AlGaAs nanowires, the InP nanowires were grown using selective-area metalorganic vapour phase epitaxy (SA-MOVPE) technique. These unpassivated InP nanowires are of high optical (~ ns minority carrier lifetime) and structural quality (stacking fault-free) with higher photosensitivity when compared with the optimised GaAs/AlGaAs nanowires. As a result, highly sensitive broadband (0.1-2.0 THz) InP single nanowire THz detectors are demonstrated, which can provide high-quality time-domain spectra for material characterisation in the THz-TDS system. The response characteristics of the InP single nanowire photoconductive THz detectors matches well with the simulation results, and are found to have a low-noise nature and a long time-domain sampling window in contrast to the traditional (bulk) THz photoconductive detectors, which will be beneficial to the future advanced THz systems for achieving higher spectral and spatial resolutions. Chapter 7 describes a further improvement in InP single nanowire photoconductive detectors by employing an axial n^+-i-n^+ InP nanowire

structure in device, as a direct result of the improved contact quality (due to contact doping). Relationships between doping concentration and nanowire growth are investigated using a locally developed novel optical technique (capable of axial profiling of doping concentration along single nanowires). The measured doping results are correlated with the electrical characterisation of corresponding nanowire devices, to further examine the relationship between the doping concentration and device contact quality, providing guidance for design of the axial n^+-i-n^+ nanowire structure. The n^+-i-n^+ InP single nanowire detectors are shown to be good alternatives to the undoped single InP nanowire detectors for the THz-TDS system, which exhibit comparable signal-to-noise ratio to that of traditional (bulk) semiconductor detectors despite of having only pA-level response current. All the results indicate that single III-V semiconductor nanowire photoconductive THz detectors are highly promising for future applications in advanced THz systems. Finally, conclusions and suggestions for future work are presented in Chapter 8.

References

[1] M. Perenzoni and D. J. Paul, Eds., *Physics and Applications of Terahertz Radiation* (Springer Series in Optical Sciences 173). Springer Netherlands, 2014.

[2] B. Ferguson and X. C. Zhang, "Materials for terahertz science and technology," *Nature Materials,* vol. 1, pp. 26-33, 2002.

[3] M. Tonouchi, "Cutting-edge terahertz technology," *Nature Photonic*s, vol. 1, pp. 97-105, 2007.

[4] K. E. Peiponen, A. Zeitler, and M. Kuwata-Gonokami, Eds., *Terahertz Spectroscopy and Imaging* (Springer Series in Optical Sciences 171). Springer Berlin Heidelberg, 2013.

[5] M. Naftaly and R. E. Miles, "Terahertz time-domain spectroscopy for material characterization," *Proceedings of the IEEE,* vol. 95, pp. 1658-1665, 2007.

[6] T. Ouchi, K. Kajiki, T. Koizumi, T. Itsuji, Y. Koyama, R. Sekiguchi, O. Kubota, and K. Kawase,"Terahertz imaging system for medical applications and related high efficiency terahertz devices," *Journal of Infrared Millimeter and Terahertz Waves,* vol. 35, pp.

118-130, 2014.

[7] G. Ok, K. Park, H. J. Kim, H. S. Chun, and S. W. Choi, "High-speed terahertz imaging toward food quality inspection," *Applied Optics*, vol. 53, pp. 1406-1412, 2014.

[8] W. R. Tribe, D. A. Newnham, P. F. Taday, and M. C. Kemp, "Hidden object detection: security applications of terahertz technology," *Terahertz and Gigahertz Electronics and Photonics III*, vol.5354, pp. 168-176, 2004.

[9] N. Born, D. Behringer, S. Liepelt, S. Beyer, M. Schwerdtfeger, B. Ziegenhagen, and M. Koch, "Monitoring plant drought stress response using terahertz time-domain spectroscopy," *Plant Physiology*, vol. 164, pp. 1571-1577, 2014.

[10] G. Ducournau, P. Szriftgiser, F. Pavanello, E. Peytavit, M. Zaknoune, D. Bacquet, A. Beck, T. Akalin, and J.-F. Lampin, "THz communications using photonics and electronic devices: the race to data-rate," *Journal of Infrared, Millimeter, and Terahertz Waves*, vol. 36, pp. 198-220, 2015.

[11] P. U. Jepsen, D. G. Cooke, and M. Koch, "Terahertz spectroscopy and imaging - modern techniques and applications," *Laser & Photonics Reviews*, vol. 5, pp. 124-166, 2011.

[12] J. Lloyd-Hughes and T.-I. Jeon, "A review of the terahertz conductivity of bulk and nano-materials," *Journal of Infrared, Millimeter, and Terahertz Waves*, vol. 33, pp. 871-925, 2012.

[13] J. A. Zeitler, P. F. Taday, D. A. Newnham, M. Pepper, K. C. Gordon, and T. Rades, "Terahertz pulsed spectroscopy and imaging in the pharmaceutical setting - a review," *Journal of Pharmacy and Pharmacology*, vol. 59, pp. 209-223, 2007.

[14] A. Markelz, A. Roitberg, and E. J. Heilweil, "Pulsed terahertz spectroscopy of DNA, bovine serum albumin and collagen between 0.1 and 2.0 THz," *Chemical Physics Letters*, vol. 320, pp. 42-48, 2000.

[15] D. Banerjee, W. Von Spiegel, M. Thomson, S. Schabel, and H. Roskos, "Diagnosing water content in paper by terahertz radiation," *Optics Express*, vol. 16, pp. 9060-9066, 2008.

[16] D. H. Auston, "Picosecond optoelectronic switching and gating in silicon," *Applied Physics Letters*, vol. 26, pp. 101-103, 1975.

[17] B. Salem, D. Morris, V. Aimez, J. Beerens, J. Beauvais, and D. Houde, "Pulsed photoconductive antenna terahertz sources made on ion-implanted GaAs substrates," *Journal of Physics: Condensed Matter*, vol. 17, pp. 7327-7333, 2005.

[18] S. Kono, M. Tani, P. Gu, and K. Sakai, "Detection of up to 20 THz with a low-temperature-grown GaAs photoconductive antenna gated with 15 fs light pulses," *Applied Physics Letters*, vol. 77, pp. 4104-4106, 2000.

[19] M. Tani, S. Matsuura, K. Sakai, and S. Nakashima, "Emission characteristics of photoconductive antennas based on low-temperature-grown GaAs and semi-insulating GaAs," *Applied Optics*, vol. 36, pp. 7853-7859, 1997.

[20] C. Wood, J. Cunningham, I. Hunter, P. Tosch, E. Linfield, and A. Davies, "On-chip pulsed terahertz systems and their applications," *International journal of infrared and millimeter waves*, vol. 27, pp. 557-569, 2006.

[21] J. Cunningham, M. Byrne, C. Wood, and L. Dazhang, "On-chip terahertz systems for spectroscopy and imaging," *Electronics Letters*, vol. 46, pp. s34-s37, 2010.

[22] N. P. Dasgupta, J. Sun, C. Liu, S. Brittman, S. C. Andrews, J. Lim, H. Gao, R. Yan, and P. Yang, "25th anniversary article: semiconductor nanowires–synthesis, characterization, and applications," *Advanced Materials*, vol. 26, pp. 2137-2184, 2014.

[23] P. U. Jepsen, R. H. Jacobsen, and S. R. Keiding, "Generation and detection of terahertz pulses from biased semiconductor antennas," *Journal of the Optical Society of America B-Optical Physics*, vol. 13, pp. 2424-2436, 1996.

[24] M. Tani, R. Fukasawa, H. Abe, S. Matsuura, K. Sakai, and S. Nakashima, "Terahertz radiation from coherent phonons excited in semiconductors," *Journal of Applied Physics*, vol. 83, pp. 2473-2477, 1998.

[25] J. Shan and T. F. Heinz, "Terahertz radiation from semiconductors," *Ultrafast Dynamical Processes in Semiconductors*, vol. 92, pp. 1-56, 2004.

[26] R. Adomavicius, A. Urbanowicz, G. Molis, and A. Krotkus, "Terahertz radiation from narrow-gap semiconductors photoexcited by femtosecond laser pulses," *Microelectronic Engineering*, vol. 81, pp. 238-242, 2005.

[27] Q. Wu, M. Litz, and X. C. Zhang, "Broadband detection capability of ZnTe electro-optic field detectors," Applied Physics Letters, vol. 68, pp. 2924-2926, 1996.

[28] A. Nahata, A. S. Weling, and T. F. Heinz, "A wideband coherent terahertz spectroscopy system using optical rectification and electro-optic sampling," *Applied Physics Letters,* vol. 69, pp. 2321-2323, 1996.

[29] H. J. Joyce, C. J. Docherty, Q. Gao, H. H. Tan, C. Jagadish, J. Lloyd-Hughes, L. M. Herz, and M. B. Johnston, "Electronic properties of GaAs, InAs and InP nanowires studied by terahertz spectroscopy," *Nanotechnology,* vol. 24, 214006, 2013.

[30] P. Parkinson, J. Lloyd-Hughes, Q. Gao, H. H. Tan, C. Jagadish, M. B. Johnston, and L. M. Herz, "Transient terahertz conductivity of GaAs nanowires," *Nano Letters,* vol. 7, pp. 2162-2165, 2007.

[31] M. Borg, H. Schmid, K. E. Moselund, G. Signorello, L. Gignac, J. Bruley, C. Breslin, P. Das Kanungo, P. Werner, and H. Riel, "Vertical III-V nanowire device integration on Si(100)," *Nano Letters,* vol. 14, pp. 1914-1920, 2014.

[32] Y. Li, F. Qian, J. Xiang, and C. M. Lieber, "Nanowire electronic and optoelectronic devices," *Materials Today,* vol. 9, pp. 18-27, 2006.

[33] H. J. Joyce, Q. Gao, Y. Kim, H. H. Tan, and C. Jagadish, "Growth, structural and optical properties of III-V nanowires for optoelectronic applications," *2007 7th IEEE Conference on Nanotechnology,* Vol 1-3, pp. 870-873, 2007.

[34] X. F. Duan, Y. Huang, Y. Cui, J. F. Wang, and C. M. Lieber, "Indium phosphide nanowires as building blocks for nanoscale electronic and optoelectronic devices," *Nature,* vol. 409, pp. 66-69, 2001.

[35] X. C. Jiang, Q. H. Xiong, S. Nam, F. Qian, Y. Li, and C. M. Lieber, "InAs/InP radial nanowire heterostructures as high electron mobility devices," *Nano Letters,* vol. 7, pp. 3214-3218, 2007.

[36] http://www.glo.se/technology.html.

[37] J. Wallentin, N. Anttu, D. Asoli, M. Huffman, I. Aberg, M. H. Magnusson, G. Siefer, P. Fuss-Kailuweit, F. Dimroth, B. Witzigmann, H. Q. Xu, L. Samuelson, K. Deppert, and M. T. Borgstrom, "InP nanowire array solar cells achieving 13.8% efficiency by exceeding the ray optics limit," *Science,* vol. 339, pp. 1057-1060, 2013.

[38] D. Saxena, S. Mokkapati, P. Parkinson, N. Jiang, Q. Gao, H. H. Tan, and C. Jagadish, "Optically pumped room-temperature GaAs nanowire lasers," *Nature Photonics,* vol. 7,

pp. 963-968, 2013.

[39] Q. Gao, D. Saxena, F. Wang, L. Fu, S. Mokkapati, Y. A. Guo, L. Li, J. Wong-Leung, P.Caroff, H. H. Tan, and C. Jagadish, "Selective-area epitaxy of pure wurtzite InP nanowires: High quantum efficiency and room-temperature lasing," *Nano Letters,* vol. 14, pp. 5206-5211, 2014.

[40] D. Saxena, N. Jiang, X. Yuan, S. Mokkapati, Y. Guo, H. H. Tan, and C. Jagadish, "Design and room-temperature operation of GaAs/AlGaAs multiple quantum well nanowire lasers," *Nano Letters,* vol. 16, pp. 5080-5086, 2016.

[41] I. Åberg, G. Vescovi, D. Asoli, U. Naseem, J. P. Gilboy, C. Sundvall, A. Dahlgren, K. E. Svensson, N. Anttu, and M. T. Björk, "A GaAs nanowire array solar cell with 15.3% efficiency at 1 Sun," *IEEE Journal of Photovoltaics,* vol. 6, pp. 185-190, 2016.

[42] Y. Kawano and K. Ishibashi, "An on-chip near-field terahertz probe and detector," *Nature Photonics,* vol. 2, pp. 618-621, 2008.

[43] C. Wood, J. Cunningham, I. C. Hunter, P. Tosch, E. H. Linfield, and A. G. Davies, "On-chip pulsed terahertz systems and their applications," *International Journal of Infrared and Millimeter Waves,* vol. 27, pp. 557-569, 2006.

[44] J. Cunningham, M. B. Byrne, C. D. Wood, and L. Dazhang, "On-chip terahertz systems for spectroscopy and imaging," *Electronics Letters,* vol. 46, pp. S34-S37, 2010.

[45] N. Erhard, P. Seifert, L. Prechtel, S. Hertenberger, H. Karl, G. Abstreiter, G. Koblmuller, and A. W. Holleitner, "Ultrafast photocurrents and THz generation in single InAs-nanowires," *Annalen Der Physik,* vol. 525, pp. 180-188, 2013.

[46] D. V. Seletskiy, M. P. Hasselbeck, J. G. Cederberg, A. Katzenmeyer, M. E. Toimil-Molares, F. Leonard, A. A. Talin, and M. Sheik-Bahae, "Efficient terahertz emission from InAs nanowires," *Physical Review B,* vol. 84, 115421, 2011.

[47] M. S. Vitiello, L. Viti, D. Coquillat, W. Knap, D. Ercolani, and L. Sorba, "One dimensional semiconductor nanostructures: An effective active-material for terahertz detection," *Apl Materials,* vol. 3, 026104, 2015.

[48] L. Romeo, D. Coquillat, M. Pea, D. Ercolani, F. Beltram, L. Sorba, W. Knap, A. Tredicucci, and M. S. Vitiello, "Nanowire-based field effect transistors for terahertz detection and imaging systems," *Nanotechnology,* vol. 24, 214005, 2013.

[49] M. S. Vitiello, D. Coquillat, L. Viti, D. Ercolani, F. Teppe, A. Pitanti, F. Beltram, L. Sorba, W. Knap, and A. Tredicucci, "Room-temperature terahertz detectors based on semiconductor nanowire field-effect transistors," *Nano Letters,* vol. 12, pp. 96-101, 2012.

[50] M. Hangyo, M. Tani, and T. Nagashima, "Terahertz time-domain spectroscopy of solids: A review," *International Journal of Infrared and Millimeter Waves,* vol. 26, pp. 1661-1690, 2005.

[51] M. C. Beard, G. M. Turner, and C. A. Schmuttenmaer, "Subpicosecond carrier dynamics in low-temperature grown GaAs as measured by time-resolved terahertz spectroscopy," *Journal of Applied Physics,* vol. 90, pp. 5915-5923, 2001.

[52] S. Gupta, J. F. Whitaker, and G. A. Mourou, "Ultrafast carrier dynamics in III-V-semiconductors grown by molecular-beam epitaxy at very low substrate temperatures," *IEEE Journal of Quantum Electronics,* vol. 28, pp. 2464-2472, 1992.

[53] E. Castro-Camus, J. Lloyd-Hughes, L. Fu, H. H. Tan, C. Jagadish, and M. B. Johnston, "An ion-implanted InP receiver for polarization resolved terahertz spectroscopy," Optics Express, vol. 15, pp. 7047-7057, 2007.

[54] T. A. Liu, M. Tani, M. Nakajima, M. Hangyo, and C. L. Pan, "Ultrabroadband terahertz field detection by photoconductive antennas based on multi-energy arsenic-ion-implanted GaAs and semi-insulating GaAs," *Applied Physics Letters,* vol. 83, pp. 1322-1324, 2003.

[55] H. J. Joyce, Q. Gao, H. H. Tan, C. Jagadish, Y. Kim, X. Zhang, Y. N. Guo, and J. Zou, "Twin-free uniform epitaxial GaAs nanowires grown by a two-temperature process," *Nano Letters,* vol. 7, pp. 921-926, 2007.

[56] N. Jiang, Q. Gao, P. Parkinson, J. Wong-Leung, S. Mokkapati, S. Breuer, H. H. Tan, C. L. Zheng, J. Etheridge, and C. Jagadish, "Enhanced minority carrier lifetimes in GaAs/AlGaAs core-shell nanowires through shell growth optimization," *Nano Letters,* vol. 13, pp. 5135-5140, 2013.

[57] N. Jiang, P. Parkinson, Q. Gao, S. Breuer, H. H. Tan, J. Wong-Leung, and C. Jagadish, "Long minority carrier lifetime in Au-catalyzed GaAs/AlxGa1-xAs core-shell nanowires," *Applied Physics Letters,* vol. 101, 023111, 2012.

[58] S. A. Fortuna and X. L. Li, "Metal-catalyzed semiconductor nanowires: a review on the control of growth directions," *Semiconductor Science and Technology*, vol. 25, 024005, 2010.

Chapter 2

Terahertz Systems and Techniques

This chapter provides the background knowledge regarding terahertz (THz) systems and techniques used in this thesis, primarily introducing THz time-domain spectroscopy (THz-TDS) and related THz sources and detectors. This chapter also describes the two common detection schemes for THz-TDS: electro-optic sampling and photoconductive sampling. The measurement characteristics of THz-TDS, including bandwidth, frequency resolution, signal-to-noise ratio and dynamic range, are introduced allowing for an evaluation of the system performance (and hence the detector performance). An example for a typical analysis of raw data from transmission measurements in THz-TDS to extract the complex optical properties of a material is provided.

2.1 Terahertz Technological Families

Technologies in the terahertz (THz) band can be categorised into two major families [1, 2] based on their operating frequency and emission mode: continuous-wave (CW) and pulsed THz systems. The CW THz systems operate quasi-monochromatically, with limited tunability in frequency band but high spectral resolution (~ hundreds of MHz), and with continuous emission. They typically provide higher THz output powers than the pulsed sources, and are suited for applications such as telecommunication [3] and non-destructive evaluation (i.e. THz imaging) [4, 5]. The pulsed THz systems are based on the generation and detection of a quasi-single cycle THz transient with duration of a few picoseconds. The THz transient typically consists of many frequencies, which can be accessed via a Fourier Transform. As opposed to CW systems, pulsed THz systems are not only able to yield intensity data, but also provide depth, time-domain or frequency-domain information in measurement, ideal for spectroscopic applications. The generation of pulsed THz radiations commonly relies on the use of femtosecond pulsed lasers [6-8].

2.2 Terahertz Time-Domain Spectroscopy

THz time-domain spectroscopy (THz-TDS) [9] is a spectroscopic technique, typically realised using a pulsed THz system, which has been explored for various THz band applications from imaging [4] to spectroscopic analysis [10]. It shows particular promise for applications in materials science, due to its ability to detect both amplitude and phase of the THz radiation interacting with a material. It can thereby provide information on the physical properties of the material represented by absorption coefficient and refractive index in the far-infrared region. Other spectroscopic techniques, for instance, traditional optical spectrometers [11] can only measure the signal intensity in near-infrared wavelength range; Fourier-transform infrared spectrometers [12] provide amplitude-only information in the mid-/far-infrared range via interferometry. In this dissertation, a laboratory THz-TDS system is used for the characterisation of all THz detectors of interest in this study. The THz related experiments were conducted at the University of Oxford (in Prof. Michael B. Johnston's laboratory).

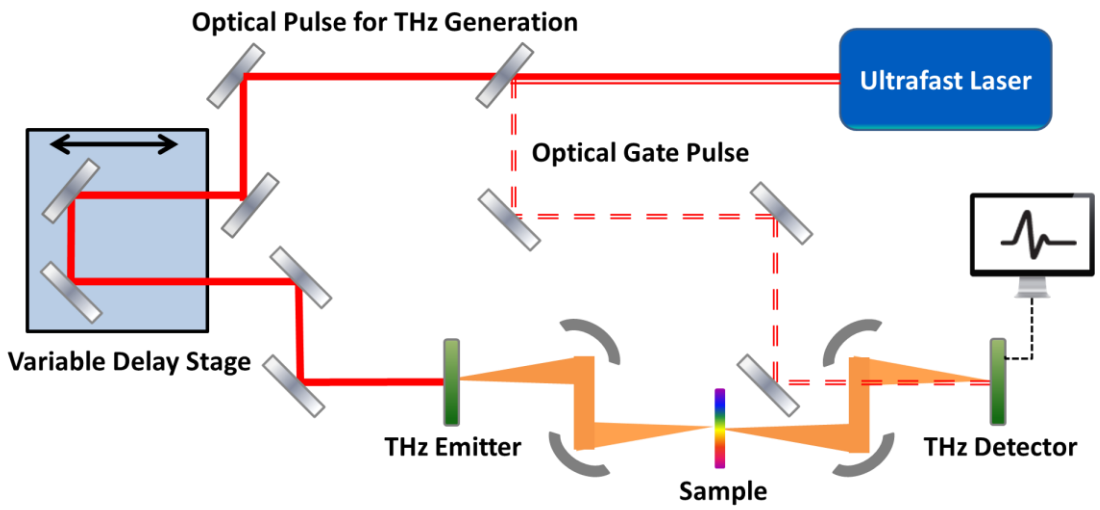

Figure 2.1: A schematic diagram of a typical pulsed THz-TDS system (operating at transmission mode).

A typical THz-TDS system is a pump-probe setup [13] as shown in Figure 2.1, in which a single cycle THz pulse (with a duration of ~ a few picoseconds) is generated from a femtosecond laser-irradiated emitter and then received by a detector that is fed with an optical

pulse from the same laser source. The THz pulse is called “probe pulse”, and the optical pulse is called “gate pulse”. An optical delay stage (controlled by a motorised translation stage) is used for one pulse to be moved in time with respect to the other, such that the waveform of the THz pulse can be mapped out as a function of the delay time between the probe and gate pulses. In applications, a sample of interest is placed in the THz path of the system, allowing the THz pulse to pass through it (or reflect from it). By measuring the change in transmitted (reflected) THz signals with and without the presence of the sample, physical constants of the sample (such as absorption coefficient and refractive index) can be extracted.

2.3 Terahertz Sources

THz radiation is accessible via black-body radiation from anything with temperatures higher than about 10 K. However, this thermal emission is incoherent and weak. Commonly used THz sources in laboratories or industry include the backward wave oscillator [14], quantum cascade laser [15], photomixing sources [16] or single cavity FIR laser [17], which produce coherent CW THz radiation throughout the THz range. Although photomixing sources have been explored for THz-quasi-TDS [18], this section focuses on introducing pulsed THz sources for typical THz-TDS, where a broadband short-pulse THz source is used.

In a THz-TDS system, the pulsed THz radiation is commonly generated from either a femtosecond laser-irradiated electro-optic material [19] (such as GaSe, ZnTe, CdTe and $LiNbO_3$) via optical rectification [20], or a femtosecond laser-irradiated photoconductive antenna (PCA) fabricated on a semiconductor with short carrier lifetime [21] (e.g. ion-bombarded InP) combined with an applied electric bias via photoconductive switching technique [22], or a femtosecond laser-irradiated narrow-gap semiconductor without applied electric field bias (e.g. InAs) via Photo-Dember effect [23], or laser-induced air plasma [24]. The emission mechanisms regarding optical rectification and photoconductive switching are described below, since they are the generation mechanisms used in this thesis.

In optical rectification, a second-order nonlinear process occurs when a femtosecond laser pulse propagates through an electro-optic material [25, 26]. A nonlinear ultra-short polarisation P is produced in the electro-optic material that is of the duration of the laser pulse (~

femtoseconds) and has the form of the pulse envelope. Based on Maxwell's equations, the ultra-short polarisation *P* will radiate off a single cycle electro-magnetic pulse in the far field with frequencies in the THz range. The emitted THz electric field in the electro-optic material is related to the polarisation, *P*, by

$$E_{(THz)} \propto \frac{\partial^2 P}{\partial t^2} \tag{2.1}$$

The bandwidth of THz pulses generated via optical rectification is limited by the laser pulse duration, THz absorption in the electro-optic material and material thickness. Conceptually, a shorter laser pulse causes a faster polarisation change in the electro-optic material which generates a shorter THz pulse consisting of more THz frequencies. The THz emission strength increases while emission bandwidth decreases with thicker material due to the phase-matching effect [27].

In photoconductive switching technique, a transient photocurrent is generated across a biased PCA when a femtosecond laser pulse (with energy above the band gap of the semiconductor) excites on it. This transient current will emit a single-cycle THz pulse, and the emitted THz electric field is related to the photo-induced current, *J*, by

$$E_{(THz)} \propto \frac{\partial J}{\partial t} \tag{2.2}$$

An important requirement for this technique is the used semiconductor substrate (emission material) has to possess some specific optoelectronic properties including a fast photocurrent rise time, high carrier mobility and short carrier lifetime. Therefore, low-temperature GaAs (LT-GaAs) [28] and semi-insulating GaAs (SI-GaAs) [29] are common materials used for photoconductive THz emission. The laser pulse duration, properties of the semiconductor (i.e. material thickness, carrier lifetime and photocurrent rise time) and resonant frequency of the antenna (electrode structure) determine the centre wavelength and spectral bandwidth of the generated THz pulse. Typically, a shorter laser pulse induces a faster current change in PCA that radiates a shorter THz pulse which is spectrally broader. The THz emission strength usually increases with increasing bias voltage and excitation laser power (if effects such as

impact ionisation and carrier-carrier scattering are not considered [7, 30]), and thus the highest strength is limited by the breakdown voltage of the PCA. The spectral bandwidth of the generated THz pulse is limited by three main factors: the laser pulse duration, resonant frequency range of the antenna [31], and THz absorption in the generation material.

2.4 Terahertz Detectors

A number of detection technologies have been developed for THz radiation over the past twenty years. Cooled THz detectors (e.g. hot electron bolometer [32]) and uncooled THz detectors (e.g. Golay cells and pyroelectric detectors [33]) are commercially available. However, not all types of THz detectors are suited for use in THz-TDS; in particular integrating detectors lose valuable information. For example, a bolometer detector is only sensitive to the "energy" of THz radiation; it is unable to measure the phase and amplitude information in THz-TDS. In Sections 2.4.1 and 2.4.2, two common detection schemes for THz-TDS are introduced, namely the electro-optical sampling and photoconductive sampling They are also the detection schemes used in this thesis.

2.4.1 Electro-Optic Sampling

Electro-optic sampling uses an electro-optic material to detect the THz pulse in THz-TDS. It is an opposite process to optical rectification in the electro-optic material, and can be viewed as a polarisation rotation measurement of a femtosecond laser pulse propagating in an electro-optic material with a linear electro-optic effect (Pockels effect [20]). The setup of the electro-optic sampling in a THz-TDS system is presented in Figure 2.2, which consists of an electro-optic crystal detector, a quarter-wavelength plate, a Wollaston prism (a type of polarising beam splitter) and a balanced photodetector. For THz detection, the THz (probe) pulse and optical (gate) pulse are allowed to collinearly propagate through the electro-optic crystal, and finally directed to the balanced photodetector after being guided over the quarter-wavelength plate and the Wollaston prism.

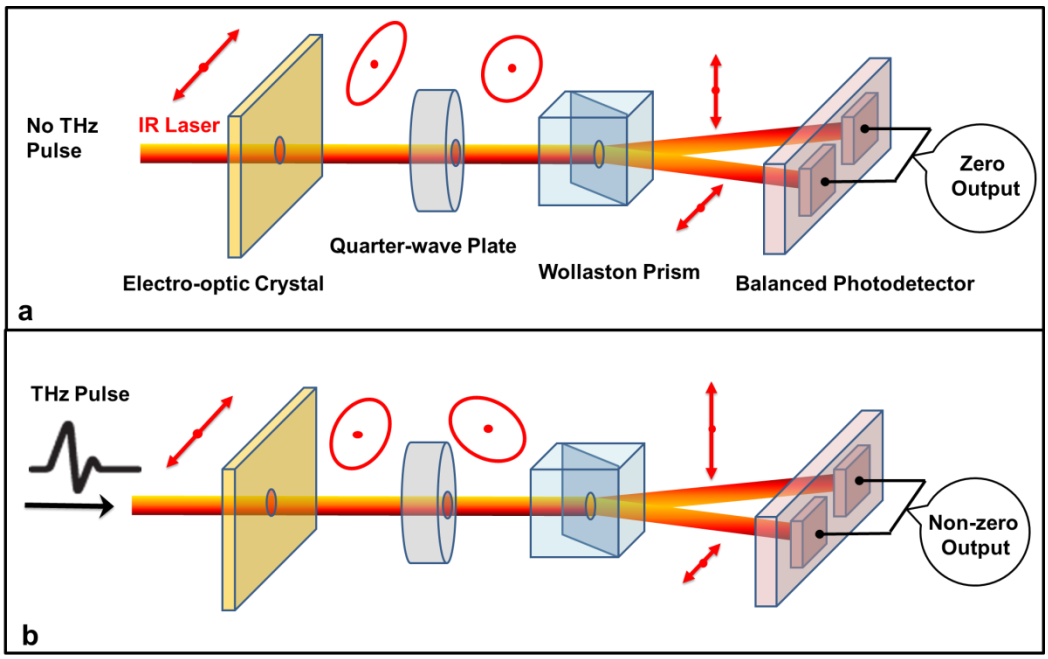

Figure 2.2: Schematic illustration of an electro-optic sampling setup (a) in the absence and (b) in the presence of the THz pulse in a THz-TDS system.

The electro-optic sampling process can be divided into two steps: (1) calibration in the absence of the THz pulse and (2) measurement in the presence of the THz pulse. In the absence of the THz pulse, the polarisation of the optical pulse is modulated from linear to circular by adjusting the quarter-wavelength plate. Then the circularly polarised optical pulse is separated into two equal components by the Wollaston prism, and collected by a balanced photodetector that consists of two identical photodiodes. For equal components, the two photodiodes in the balanced photodetector produce null current in between as shown in Figure 2.2(a). After calibration, the THz pulse (to be measured) is induced in the sampling path. The THz electric field causes a birefringence in the electro-optic crystal, which rotates the polarisation of the transmitted optical pulse. The polarisation of the transmitted optical pulse is modulated from linear to elliptic after passing through the quarter-wavelength plate. As a result, the two components become uneven, and thus the two photodiodes produce a differential current as shown in Figure 2.2(b). The detected current $I_{(det)}$, is related to the optical index n, effective electro-optic coefficient r_{eff}, electro-optic crystal thickness d and the incident THz electric field $E_{(THz)}$, expressed by

$$I_{(det)} \propto n^3 r_{eff}\, d\, E_{(THz)} \tag{2.3}$$

Therefore by varying the time delay between the THz pulse and optical pulse in the THz-TDS system, the current in the balanced photodetector as a function of delay time can be recorded which is proportional to the temporal waveform profile of the measured THz electric field $E_{(THz)}$.

2.4.2 Photoconductive Sampling

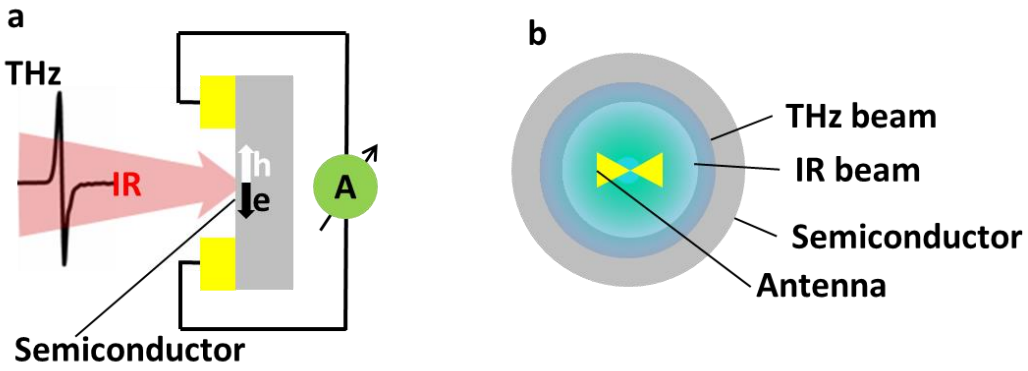

Figure 2.3: (a) A schematic illustration of a PCA in operation. (b) A collinear geometry for THz beam and excitation laser beam in setup.

Photoconductive sampling [34, 35] uses a PCA to detect the THz pulse in THz-TDS. It is an opposite process to photoconductive THz generation. A setup of the THz detection mechanism in a THz-TDS system using photoconductive detectors is presented in Figure 2.3. Typically, a photoconductive THz detector (or a PCA) consists of two metal electrodes (also known as antenna) that are coated on a semiconductor substrate with a gap between those two electrodes as shown in Figure 2.3(a). The electrodes are externally connected to a current sensor. For effective THz detection, the semiconductor substrate (detection material) is required to have a fast photocurrent rise time, high carrier mobility and short carrier lifetime, similarly as required in the photoconductive emitter. In the sampling process, an optical pulse (with energy above the band gap of the semiconductor substrate) excites the centre of the detector, and simultaneously a

well-aligned THz pulse is incident on the centre providing an electric field in the gap (see Figure 2.3(b)). The optical pulse generates electron-hole pairs in the gap region of the semiconductor substrate while the electric field of the THz pulse separates the electron-hole pairs and drives a transient photocurrent across the two electrodes. The intensity of the transient photocurrent is related to the strength of the incident THz electric field. Therefore by changing the time delay between the THz pulse and optical pulse at the detector, the temporal profile of the THz-induced photocurrent can be recorded which is proportional to the temporal waveform profile of the measured THz electric field. The transient photocurrent between the two electrodes of a photoconductive detector with respect to the THz-gate time delay (τ) [36] can be expressed by

$$I(\tau) \propto \int_{-\infty}^{+\infty} E_{(THz)}(t)\, \sigma(t-\tau) dt \qquad (2.4)$$

where $E_{(THz)}(t)$ is the effective electric field of the THz transient at the photoconductive detector and $\sigma(\tau)$ is the time dependant photoconductivity of the detection material.

When the detection material has an extremely short charge-carrier lifetime (< 1ps) than the duration of the THz transient (typically ~ 2 ps), a simplification can be made in equation (2.4). In this case, the conductivity $\sigma(\tau)$ of the detection material will be considered as a δ function as if the optical pulse generates a spike in conductivity in the material, where the THz-induced photocurrent is simplified as

$$I(\tau) \propto E_{(THz)}(t = \tau) \qquad (2.5)$$

The measured photocurrent intensity in the detector is directly proportional to the strength of the incident THz electric field. Such a detector is categorised as a "direct sampling" photoconductive detector.

When the detection material has a long charge-carrier lifetime (> 100 ps) than the duration of the THz transient, the conductivity $\sigma(\tau)$ of the detection material will be approximated as a unit step function and the detector is categorised as an "integrating" photoconductive detector, where

$$I(\tau) \propto \int_{\tau}^{\infty} E_{(THz)}(t)dt \tag{2.6}$$

From equation (2.6), it is note that the THz electric field $E_{(THz)}(t)$ can be recovered from the $I(\tau)$ data by differentiation with respect to the time. However, the approximation fails when the charge-carrier lifetime of the detection material is on the same scale as the measurement range (1 ps < τ <100 ps). In this case, $E_{(THz)}(t)$ can be extracted by deconvolution of the measured $I(\tau)$ data, which is written as

$$I(\tau) = \beta \int_{-\infty}^{+\infty} E_{(THz)}(t)\, \Phi(t-\tau)dt \tag{2.7}$$

where Φ is the normalised time dependent conductivity, β is a constant directly related to material properties and optical excitation condition. Equation (2.7) is a Fredholm integral equation that can be viewed as a convolution of functions $E_{(THz)}$ and Φ (in the Fourier sense), whose solution is given by

$$E_{(THz)} = \beta \mathcal{F}^{-1}\left[\frac{\mathcal{F}(I)}{\mathcal{F}(\Phi)}\right] \tag{2.8}$$

where $\mathcal{F}$ is the Fourier transform operator. In fact, in most THz-TDS systems the duration of the laser pulse is much shorter than the THz transient. Therefore, Φ can be further approximated as

$$\Phi \approx \mathcal{H}(t)e^{-t/\tau_c} \tag{2.9}$$

where $\mathcal{H}$ is the unit step function. Thus equation (2.8) can be simplified and written by

$$E_{(THz)} = \beta \mathcal{F}^{-1}\left[\mathcal{F}(I)\left(\frac{1}{\tau_c} + i\omega\right)\right] \tag{2.10}$$

where ω is the angular frequency, τ_c is the photoconductivity lifetime of the detection

material. In this case, the detector is categorised as an “intermediate” photoconductive detector.

2.5 Measurement Characteristics

In order to describe the performance of a THz-TDS system, some important parameters including bandwidth, frequency resolution, signal-to-noise ratio and dynamic range are defined [9] in this section, and used to quantify the performance of the THz-TDS system. These parameters will be calculated using the experimental results as described in Chapters 4-7. This section only presents a mathematical description of how to obtain these parameters from the THz-TDS measurement. Since most THz-TDS measurement parameters are kept the same in this thesis except for the detector types, the THz-TDS system performance can be directly correlated to the performance of the THz detector. In addition, measurements as well as the data extraction process of the complex optical properties of a material in a THz-TDS system are discussed, which will be shown in later chapters to demonstrate the practical value of the studied nanowire detectors.

2.5.1 From Time-Domain to Frequency-Domain Data

The raw data of a THz-TDS measurement compose of the shape and strength of the electric field of the THz pulse, which are collected in time domain as shown in Figure 2.4(a). To obtain corresponding frequency-domain data, a Fourier Transformation is applied on the temporal data to extract its frequency components. The converted data in frequency domain includes both phase and amplitude information over the THz frequency range, as presented in Figures 2.4(b) and (c), respectively. Typically, THz-TDS measurements are carried out in vacuum to avoid the absorption of THz radiation by atmospheric water vapour.

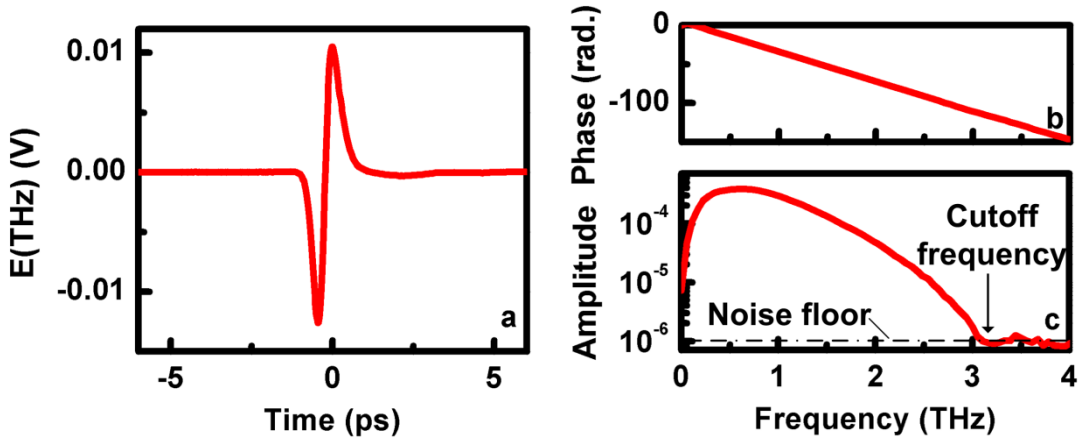

Figure 2.4: (a) A typical time-domain THz signal in the THz-TDS measurement (obtained from a ZnTe electro-optic crystal detector). (b) Phase and (c) amplitude frequency spectra of the THz signal processed from (a).

2.5.2 Frequency Spectral Resolution

The frequency spectral resolution of THz-TDS determines the minimum line width observable on the measured response frequency spectrum. Based on Fourier theory, the spectral resolution of THz-TDS is dependent on the extent of its temporal measurement [37], where the spectral resolution Δf in converted frequency-domain data is proportional to the temporal measurement window T, expressed by

$$\Delta f \approx \frac{1}{T} \tag{2.11}$$

In experiments, the temporal measurement window T is fundamentally limited by two factors: (1) scanning length of the delay stage in THz-TDS, and (2) noise level of the THz-TDS system. Theoretically, the maximum length of the scanning delay is determined by the duration between the two consecutive THz pulses in the THz-TDS system, which is related to the repetition rate of the femtosecond laser source used for THz generation. However, in real cases, the scanning length is much shorter (< 10 ps), as reflections of the THz pulse at the interfaces of elements (such as the emitter, detector, sample and lenses), called Fabry-Pérot reflections,

will be recorded in the time-domain data early ahead of the arrival of the second main THz pulse. Therefore, the scanning length in experiments is usually chosen to be short of the first reflected THz pulse in the system to avoid the possible artefacts in Fourier analysis. In this dissertation, the first reflected THz pulse in the measurement is mostly caused by the reflection from the detector and emitter due to their limited thicknesses (as will be discussed in Chapter 6). The measurement noise of a THz-TDS system commonly arises from external sources (such as intensity fluctuations in the THz pulse or laser pulse), which are the same for any detector used in this dissertation. However, for photoconductive THz detection, there are other noise sources in the measurement, namely, Johnson-Nyquist and shot noise [38], which is related to the electrical properties of the semiconductor (detection material) used in photoconductive detectors (as will be discussed in Chapter 5).

2.5.3 Bandwidth

Measurement bandwidth of a THz-TDS system in this thesis is defined as the cut-off frequency at the noise floor of its frequency spectrum (see Figure 2.4(c)), where the noise floor is given by averaging of the noise current in the spectrum. The measured bandwidth is primarily limited by two factors: bandwidth of the THz source and properties of the detector (e.g. detection material type and quality). In this thesis work, since the THz source was generated from the same femtosecond laser source and emitter, the performance of the detector plays a key role in the measured bandwidth. For photoconductive THz detectors, the properties of detection material (such as dark resistivity, carrier lifetime and carrier mobility) determine the measurable signal size and noise current level [36], and thus influence the measured bandwidth. Moreover, as will be discussed in Chapters 4 and 5, it is found that the antenna resonance of the photoconductive detector limits the accessible response frequency.

2.5.4 Signal-to-Noise Ratio and Dynamic Range

Signal-to-noise ratio (SNR) and dynamic range (DR) are two essential figures of merit to

evaluate the performance of a THz-TDS system. SNR determines the accuracy and stability of the measurement. DR determines the ability to measure strongly attenuating samples. In this dissertation, the detector is the only variable in the THz-TDS measurement. Therefore, SNR and DR can be used to represent the performance of the detector. Since there are many disparate methods of defining SNR and DR in relation to TDS systems, this section clarifies the definition of SNR and DR strictly based on reference [39].

For calculation of SNR, the signal is defined as the peak-to-peak current (in time domain), and the noise is defined as the standard deviation of the difference of two consecutive scans (with identical measurement parameters). It is expressed by

$$SNR = \frac{I_{(mean\ peak)}}{\sigma_{(scan-scan)}} \tag{2.12}$$

DR is defined as the peak-to-peak current over one time-domain scan to the standard deviation of the noise current in the absence of THz over the same scan, which is expressed by

$$DR = \frac{I_{(mean\ peak)}}{\sigma_{(mean\ noise\ floor)}} \tag{2.13}$$

2.6 Extraction of Material Parameters in THz-TDS

The choice of applications determines the data extraction process. In this thesis, transmission THz-TDS measurements were performed to demonstrate the functionality of the THz-TDS system, which can be associated with the practicality of the studied detector (see in Chapters 4-7). Related measurement steps and calculation methods are given below. The basic approach to analyse reflection THz-TDS measurements is similar to the transmission measurements but will not be discussed here.

2.6.1 Complex Transmission Properties

The complex optical properties of a material can be obtained via THz-TDS by measuring a

reference THz pulse E_{ref} transmitting through an empty stage and a sample THz pulse E_{sample} transmitting through the same stage with a material of thickness d placed in the THz path. These two time-domain data are converted into the frequency domain as shown in Figures 2.5(a) and (b). The phase difference between the sample and reference signals is calculated as demonstrated in Figure 2.5(c). The amplitude transmission of the THz electric field calculated by taking the ratio of the sample to reference spectrum is shown in Figure 2.5(d). For simplicity, it is convenient to define the phase difference $\emptyset(v) = \emptyset_{sample}(v) - \emptyset_{ref}(v)$ and ratio of the spectral amplitudes $A(v) = |E_{sample}|/|E_{ref}|$ of the two frequency spectra.

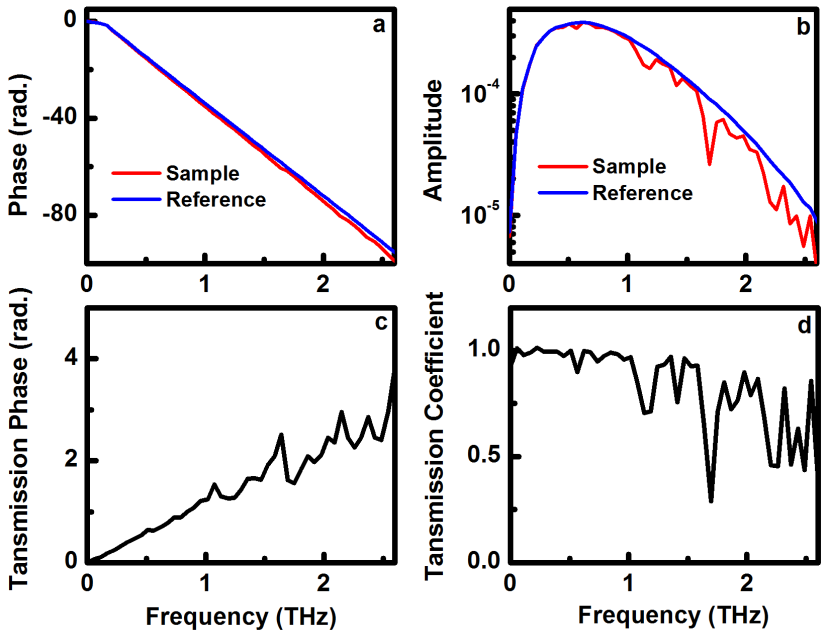

Figure 2.5: (a) Phase and (b) amplitude frequency spectra of the reference and sample signal. (c) Phase difference of the two spectra in (a). (d) Amplitude transmission ratio of the two spectra in (b). Blue solid line: reference signal. Red solid line: sample signal (water absorption lines).

2.6.2 Refractive Index and Absorption Coefficient

As the amplitude and phase changes in the measured THz signal are relate to the optical properties of the material [9], based on the obtained transmission results in Section 2.6.1, the

refractive index $n(v)$ and absorption coefficient $\alpha(v)$ of the measured material can be calculated as a function of THz frequency v from $\emptyset(v)$ and $A(v)$ using [40-42]:

$$n(v) = 1 + c \cdot \emptyset(v)/[2\pi v d] \quad (2.14)$$

$$T(v) = 1 - R = 1 - [n(v) - 1]^2/[n(v) + 1]^2 \quad (2.15)$$

$$\alpha(v) = -\ln[T(v) \cdot A(v)]/d \quad (2.16)$$

where d is the sample thickness, and R is the Fresnel loss at the air-sample interface. It is worth emphasising that, above equations from (2.14) to (2.16) are based on the condition that the THz signal passes through a material with parallel surfaces at a normal angle of incidence, assuming no reflections. Other measurement conditions will not be discussed here, as all experiments described in this thesis were conducted under this condition only.

2.7 Summary

This chapter has outlined the operation and principles of the main THz techniques employed in this thesis, with an emphasis on the introduction of THz-TDS, which has been used to characterise the THz detectors of interest. The related data processing methods used to examine the detector performance are also explained. Several key parameters regarding the THz-TDS measurement, such as bandwidth, signal-to-noise ratio and dynamic range, widely used throughout the thesis have been defined in this Chapter. For further information, the reader is referred to the cited references.

References

[1] P. H. Siegel, "Terahertz technology," *IEEE Transactions on Microwave Theory and Techniques*, vol. 50, pp. 910-928, 2002.

[2] A. Y. Pawar, D. D. Sonawane, K. B. Erande, and D. V. Derle, "Terahertz technology and its applications," *Drug Invention Today,* vol. 5, pp. 157-163, 2013.

[3] I. F. Akyildiz, J. M. Jornet, and C. Han, "Terahertz band: Next frontier for wireless communications," *Physical Communication,* vol. 12, pp. 16-32, 2014.

[4] J. B. Jackson, M. Mourou, J. F. Whitaker, I. N. Duling Iii, S. L. Williamson, M. Menu, and G. A. Mourou, "Terahertz imaging for non-destructive evaluation of mural paintings," *Optics Communications,* vol. 281, pp. 527-532, 2008.

[5] I. Amenabar, F. Lopez, and A. Mendikute, "In introductory review to THz non-destructive testing of composite mater," *Journal of Infrared, Millimeter, and Terahertz Waves,* vol. 34, pp. 152-169, 2013.

[6] T. Masahiko, H. Michael, and S. Kiyomi, "Generation and detection of terahertz pulsed radiation with photoconductive antennas and its application to imaging," *Measurement Science and Technology,* vol. 13, pp. 1739-1745, 2002.

[7] J. Shan and T. F. Heinz, "Terahertz radiation from semiconductors," *Ultrafast Dynamical Processes in Semiconductors,* vol. 92, pp. 1-56, 2004.

[8] R. Adomavicius, A. Urbanowicz, G. Molis, and A. Krotkus, "Terahertz radiation from narrow-gap semiconductors photoexcited by femtosecond laser pulses," *Microelectronic Engineering,* vol. 81, pp. 238-242, 2005.

[9] W. Withayachumnankul and M. Naftaly, "Fundamentals of measurement in terahertz time-domain spectroscopy," *Journal of Infrared, Millimeter, and Terahertz Waves,* vol. 35, pp. 610-637, 2014.

[10] J. El Haddad, B. Bousquet, L. Canioni, and P. Mounaix, "Review in terahertz spectral analysis," *Trac-Trends in Analytical Chemistry,* vol. 44, pp. 98-105, 2013.

[11] G. Reich, "Near-infrared spectroscopy and imaging: Basic principles and pharmaceutical applications," *Advanced Drug Delivery Reviews,* vol. 57, pp. 1109-1143, 2005.

[12] P. R. Griffiths and J. A. de Haseth, *Fourier Transform Infrared Spectrometry,* Second Edition ed.: John Wiley & Sons, Inc., 2006.

[13] A. Beeby, "Pump-Probe Laser Spectroscopy," in *An Introduction to Laser Spectroscopy: Second Edition*, D. L. Andrews and A. A. Demidov, Eds., ed Boston,

MA: Springer US, 2002, pp. 105-137.

[14] L. Ives, C. Kory, M. Read, J. Neilson, M. Caplan, N. Chubun, S. Schwartzkopf, and R. Witherspoon, "Development of backward wave oscillators for terahertz applications," *Terahertz for Military and Security Applications*, vol. 5070, pp. 71-82, 2003.

[15] B. S. Williams, "Terahertz quantum-cascade lasers," *Nature Photonics*, vol. 1, pp. 517-525, 2007.

[16] S. Preu, G. H. Dohler, S. Malzer, L. J. Wang, and A. C. Gossard, "Tunable, continuous-wave Terahertz photomixer sources and applications," *Journal of Applied Physics*, vol. 109, 061301, 2011.

[17] https://www.edinst.com/products/295-stand-alone-fir-laser/.

[18] M. Scheller and M. Koch, "Terahertz quasi time domain spectroscopy," *Optics Express*, vol. 17, pp. 17723-17733, 2009.

[19] B. Pradarutti, G. Matthäus, S. Riehemann, G. Notni, S. Nolte, and A. Tünnermann, "Highly efficient terahertz electro-optic sampling by material optimization at 1060 nm," *Optics Communications*, vol. 281, pp. 5031-5035, 2008.

[20] A. Tomasino, A. Parisi, S. Stivala, P. Livreri, A. C. Cino, A. C. Busacca, M. Peccianti, and R. Morandotti, "Wideband THz time domain spectroscopy based on optical rectification and electro-optic sampling," *Scientific Reports*, vol. 3, 03116, 2013.

[21] B. Salem, D. Morris, Y. Salissou, V. Aimez, S. Charlebois, M. Chicoine, and F. Schiettekatte, "Terahertz emission properties of arsenic and oxygen ion-implanted GaAs based photoconductive pulsed sources," *Journal of Vacuum Science & Technology A*, vol. 24, pp. 774-777, 2006.

[22] D. H. Auston, "Picosecond optoelectronic switching and gating in silicon," *Applied Physics Letters*, vol. 26, pp. 101-103, 1975.

[23] V. Apostolopoulos and M. Barnes, "THz emitters based on the photo-Dember effect," *Journal of Physics D: Applied Physics*, vol. 47, 374002, 2014.

[24] H. Zhong, N. Karpowicz, and X.-C. Zhang, "Terahertz emission profile from laser-induced air plasma," *Applied Physics Letters*, vol. 88, 261103, 2006.

[25] A. Rice, Y. Jin, X. F. Ma, X. C. Zhang, D. Bliss, J. Larkin, and M. Alexander, "Terahertz optical rectification from <110> zinc-blende crystals," *Applied Physics*

Letters, vol. 64, pp. 1324-1326, 1994.

[26] A. Nahata, A. S. Weling, and T. F. Heinz, "A wideband coherent terahertz spectroscopy system using optical rectification and electro-optic sampling," *Applied Physics Letters,* vol. 69, pp. 2321-2323, 1996.

[27] N. C. van der Valk, P. C. Planken, A. N. Buijserd, and H. J. Bakker, "Influence of pump wavelength and crystal length on the phase matching of optical rectification," *JOSA B,* vol. 22, pp. 1714-1718, 2005.

[28] Y. C. Shen, P. C. Upadhya, E. H. Linfield, H. E. Beere, and A. G. Davies, "Ultrabroadband terahertz radiation from low-temperature-grown GaAs photoconductive emitters," *Applied Physics Letters,* vol. 83, pp. 3117-3119, 2003.

[29] G. Zhao, R. N. Schouten, N. van der Valk, W. T. Wenckebach, and P. C. M. Planken, "Design and performance of a THz emission and detection setup based on a semi-insulating GaAs emitter," *Review of Scientific Instruments,* vol. 73, pp. 1715-1719, 2002.

[30] J. Bude, K. Hess, and G. J. Iafrate, "Impact ionization in semiconductors: Effects of high electric fields and high scattering rates," *Physical Review B,* vol. 45, pp. 10958-10964, 1992.

[31] M. Tani, S. Matsuura, K. Sakai, and S. Nakashima, "Emission characteristics of photoconductive antennas based on low-temperature-grown GaAs and semi-insulating GaAs," *Applied Optics,* vol. 36, pp. 7853-7859, 1997.

[32] Y. Jiang, B. Jin, W. Xu, L. Kang, J. Chen, and P. Wu, "Terahertz detectors based on superconducting hot electron bolometers," *Science China Information Sciences,* vol. 55, pp. 64-71, 2012.

[33] P. Kaufmann, R. Marcon, A. S. Kudaka, M. M. Cassiano, L. O. T. Fernandes, A. Marun, P. Pereyra, R. Godoy, E. Bortolucci, M. B. Zakia, J. A. Diniz, A. M. P. A. d. Silva, A. V. Timofeevsky, and V. A. Nikolaev, "Uncooled detectors of continuum terahertz radiation," *Journal of Microwaves, Optoelectronics and Electromagnetic Applications,* vol. 10, pp. 288-294, 2011.

[34] J. R. Hwang, H. J. Cheng, J. F. Whitaker, and J. V. Rudd, "Photoconductive sampling with an integrated source follower amplifier," *Applied Physics Letters,* vol. 68, pp.

1464-1466, 1996.

[35] S. G. Park, M. R. Melloch, and A. M. Weiner, "Comparison of terahertz waveforms measured by electro-optic and photoconductive sampling," *Applied Physics Letters*, vol. 73, pp. 3184-3186, 1998.

[36] E. Castro-Camus, L. Fu, J. Lloyd-Hughes, H. H. Tan, C. Jagadish, and M. B. Johnston, "Photoconductive response correction for detectors of terahertz radiation," *Journal of Applied Physics*, vol. 104, 053113, 2008.

[37] S. Mickan, J. Xu, J. Munch, X. C. Zhang, and D. Abbott, "The limit of spectral resolution in THz time-domain spectroscopy," *Photonics: Design, Technology, and Packaging*, vol. 5277, pp. 54-64, 2004.

[38] E. Castro-Camus, J. Lloyd-Hughes, L. Fu, H. H. Tan, C. Jagadish, and M. B. Johnston, "An ion-implanted InP receiver for polarization resolved terahertz spectroscopy," *Optics Express*, vol. 15, pp. 7047-7057, 2007.

[39] M. Naftaly and R. Dudley, "Methodologies for determining the dynamic ranges and signal-to-noise ratios of terahertz time-domain spectrometers," *Optics Letters*, vol. 34, pp. 1213-1215, 2009.

[40] L. Duvillaret, F. Garet, and J. L. Coutaz, "A reliable method for extraction of material parameters in terahertz time-domain spectroscopy," *IEEE Journal of Selected Topics in Quantum Electronics*, vol. 2, pp. 739-746, 1996.

[41] B. Hussain, M. Nawaz, M. Ahmed, and M. Y. A. Raja, "Measurement of thickness and refractive index using femtosecond and terahertz pulses," *Laser Physics Letters*, vol. 10, 055301, 2013.

[42] A. H. Cordes, D. H. Thomas, and J. P. von der Weid, "Phase measurements on terahertz waves," *Optics Letters*, vol. 38, pp. 3704-3707, 2013.

Chapter 3

Experimental and Simulation Methods

This chapter describes the key experimental techniques employed in this thesis, namely:

- III–V nanowire growth and characterisation, including metalorganic vapour phase epitaxy (MOVPE), scanning electron microscopy (SEM), transmission electron microscopy (TEM), photoluminescence (PL) spectroscopy and optical pump-terahertz probe (OPTP) spectroscopy.
- Single nanowire device fabrication, including direct-laser writing lithography (DLWL), ultraviolet (UV) lithography, and electron beam lithography (EBL),
- Single nanowire device characterisation, including dark/photo current-voltage (I-V) measurement, photocurrent mapping, four-terminal I-V measurement and terahertz time-domain spectroscopy (THz-TDS).

Since some techniques are complex and versatile, the discussion is restricted to the key functionalities relevant to this work. In addition, the theory and approach of optical simulation based on finite-difference time-domain (FDTD) method to understand the relationship between detector response characteristics and device geometry designs are also described in this chapter.

3.1 Nanowire Growth

Generally speaking, there are two main approaches to produce III-V nanowires: (1) through a conventional top-down approach via lithography and etching [1]; (2) through a variety of bottom-up growth approaches [2, 3]. The former is a size reduction process, which has difficulty to create structures below tens of nanometers. The latter enables creating a wide range of nanowire materials with controlled size (ranging from Angstroms to hundreds of nanometers [2]), crystallographic quality, composition, and doping. In this dissertation, all III-V nanowire samples were grown at the Australian National University (by collaborators, Dr. Qiang Gao and Miss Qian Gao) through the bottom-up processes using metalorganic vapour

phase epitaxy (MOVPE) technique based on Au-assisted vapour–liquid–solid (VLS) and selective area epitaxy (SAE) mechanisms, as will be discussed in Sections 3.1.2 and 3.1.3 respectively.

3.1.1 Metalorganic Vapour Phase Epitaxy

MOVPE, also known as metalorganic chemical vapour deposition (MOCVD), is a chemical vapour deposition method used to produce high-quality epitaxial single crystal materials (especially compound semiconductors) on single crystal substrates, based on the surface reaction between the high-purity organic compounds (or metalorganics) and metal hydrides containing the required chemical elements. III-V nanowires can be synthesised using MOVPE through a variety of growth mechanisms [4, 5] including SAE growth, oxide-assisted growth, VLS growth and vapour-solid-solid growth. The nanowires used in this dissertation were grown either by VLS or SAE, which are the most commonly used techniques for the growth of III-V nanowires.

3.1.2 Au-Assisted Vapour-Liquid-Solid Growth

The VLS mechanism is highly effective to realise one-dimensional materials via various growth techniques including MOVPE [6], laser ablation [7] and molecular beam epitaxy [8], in which a liquid catalyst acts as a mini sink for absorption of gaseous reactants to direct the growth of one-dimensional materials [6, 9]. In this thesis, Au-assisted VLS growth is used to produce core-shell GaAs/AlGaAs nanowires in a commercial MOVPE reactor (AIXTRON 200/4, see Figure 3.1(a)). Growth details are described in Chapter 4. The fundamental Au-assisted VLS growth process of III-V nanowires is demonstrated in Figure 3.1(b). Firstly, a semiconductor substrate is pre-treated with a poly-L-lysine solution and dried with a nitrogen gun (to introduce a Coulombic attraction between the substrate and the Au nanoparticles). Au nanoparticles with a specific size (ranging from 50 to 280 nm in this work) are deposited on the surface of the semiconductor substrate, and the substrate is loaded into the MOVPE reactor.

To initiate the growth, the substrate is heated to high temperature (ranging from 400 to 750 ºC). Then the vapour phase group III and group V precursors are introduced into the reaction chamber. The Au nanoparticles, together with some reactant species form a eutectic alloy (i.e. Au-reactant) on the substrate. For example, Au–Ga eutectic is formed during the growth of GaAs nanowires in this work. With a continual supply of reactants, the Au-reactant alloy nanoparticles become supersaturated and crystal nucleation begins at the nanoparticle-substrate interface. With a further supply of group III and V reactants, precipitation of III–V material occurs where one-dimensional crystal growth begins. The diameter of the VLS-grown nanowires is primarily determined by the size of the Au nanoparticles, as the liquid Au droplet is confined to the area of the precipitated solid. During growth, precipitation on the sidewalls of the nanowires (so called radial growth) may occur simultaneously via vapour-solid mechanism and competes with the VLS growth. This radial growth is commonly unintentional. To obtain uniform diameter of the grown nanowires, V/III ratio and the substrate temperature (which affect the nanowire nucleation, growth rate and preferred growth orientation) need to be carefully optimised to minimise the radial growth [10]. On the other hand, the radial growth can also be further promoted and optimised to form a uniform layer around the nanowires, creating radial heterostructures like the core-shell GaAs/AlGaAs nanowires studied in this work, where the AlGaAs shell is used to passivate the surface states of GaAs nanowires [11].

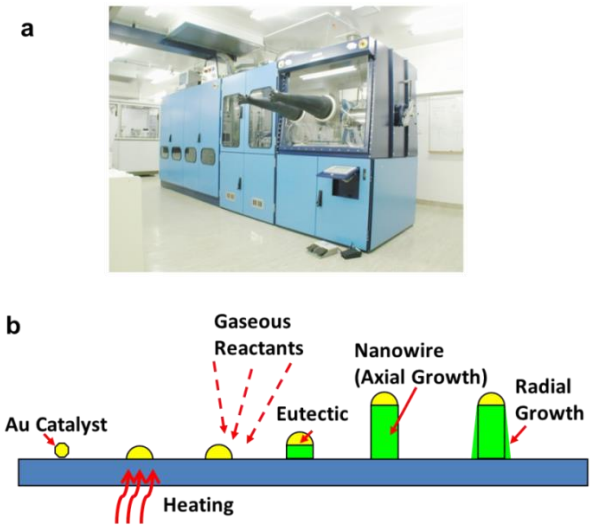

Figure 3.1: (a) Image of the MOVPE reactor used in this work. (b) A schematic illustration of the VLS growth of a single III-V nanowire using an Au catalyst particle.

3.1.3 Selective Area Epitaxy

It has been found that metal catalysts in VLS growth may act as unintended impurities inside the nanowires and form deep defect levels [12] which degrade the optical and electrical properties of the grown nanowires. The SAE growth of III-V nanowires using MOVPE (so called SA-MOVPE [13-15]) was developed to reduce concerns of catalyst contamination. The SAE growth is a template-based catalyst-free growth method involving a combination of bottom-up (epitaxial growth) and top-down (lithography) approaches. It is capable of forming less contaminant and well-aligned arrays of nanowires beneficial for many device applications (e.g. nanowire array solar cells and light-emitting diodes [16, 17]). In addition, the morphological inhomogeneity [18] of nanowires that commonly happens to Au-catalyst VLS growth can often be circumvented by using SAE growth. The basic SAE process to grow III-V nanowires using MOVPE is shown in Figure 3.2.

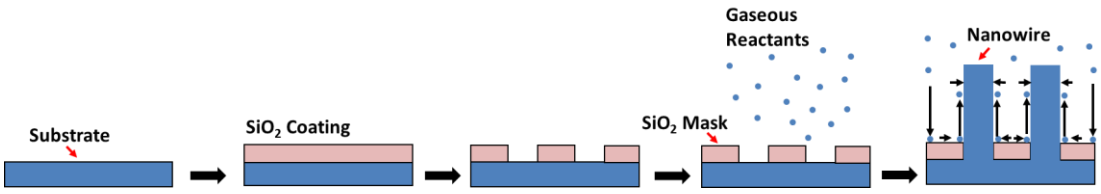

Figure 3.2: A schematic demonstration of the SAE growth of III-V nanowires.

Firstly, a thin layer of dielectric mask (e.g. ~ 30 nm SiO_2 or SiN_x) is coated on the top of a semiconductor substrate and then patterned through nano-lithography technique such as electron beam lithography (EBL) or nanoimprint lithography and (dry or wet) chemical etching to create position-controlled nano-size openings (i.e. holes) in the mask (which are used to direct nanowire growth). The patterned substrate is loaded into the MOVPE reactor. Reactant gases are supplied into the reactor chamber, and epitaxial growth occurs inside the openings and continues for one-dimensional crystal growth. Similar to the VLS growth, V/III ratio as well as the substrate temperature in SAE growth are crucial for obtaining uniform crystal structure and high-quality nanowires with uniform shape and size. The diameter of the SAE nanowire is primarily defined by the feature size of the opening on the SiO_2 or SiN_x mask but may increases due to radial growth under certain growth conditions and/or spaces between the

openings (e.g. pitch between two adjacent openings) [19]. Ultra-high quality defect-free pure wurtzite SAE-grown InP nanowires have been demonstrated by the Australian National University group [20]. In this thesis, these catalyst-free and defect-free InP nanowires are also grown and investigated for THz detection (growth details will be discussed in Chapter 6 and 7).

3.2 Nanowire Characterisation

In order to select suitable nanowire materials for optimised terahertz (THz) detection, several techniques were employed to characterise the nanowires after growth. Since semiconductors suitable for THz detection typically require both an ultra-short carrier lifetime to minimise the current noise and a reasonable carrier mobility to ensure a sufficient response level [21], all used material characterisation techniques were aimed to, directly or indirectly, determine the material quality, carrier lifetime and carrier mobility of the as-grown nanowires.

3.2.1 Scanning Electron Microscopy

Scanning electron microscopy (SEM) [22] is a powerful technique widely used to characterise the material morphology, element distribution or composition. It is realised by scanning a sample with a focused beam of electrons with sub-nanometre resolution. The incident electrons interact with atoms in a material sample at various depths, and generate scattered electrons including secondary electrons (inelastic) and back-scattered electrons (elastic), photons of characteristic X-rays as well as electron-hole pairs [23]. By collecting these scattered electrons or signals with appropriate detectors, information (such as the surface topography and composition) about the sample can be obtained. In this dissertation, SEM (FEI Helios 600 nanolab) was used to examine the nanowire morphology and image the fabricated single nanowire devices at the Australian National Fabrication Facility (ANFF) ACT node in the Australian National University.

3.2.2 Transmission Electron Microscopy

Transmission Electron Microscopy (TEM) [24] is another valuable technique to characterise the microscopic structural properties of materials. It employs a highly focused electron beam as a probe that interacts with an ultra-thin material sample and transmits through it. The transmitted electrons are captured by an imaging device (e.g. a charge coupled device camera) to form a 2D picture, providing fine details of the sample (such as chemical composition, crystal structure and orientation, sample-induced electron phase shift and the regular absorption image). TEM can achieve an image with a resolution of the order of a few Angstroms. However, the preparation of TEM sample is commonly challenging and time-consuming as it requires the sample to be very thin (typically 10-100 nm) such that the electron beam can pass through it. In this work, TEM images were taken by JEOL JSM2100F working in scanning TEM mode to study the crystal structure, identify defects and image the cross sections of the as-grown nanowires. It was carried out at the Centre for Advanced Microscopy in the Australian National University, in collaboration with Dr. Ya-nan Guo.

3.2.3 Photoluminescence and Time-Resolved Photoluminescence Spectroscopy

Photoluminescence (PL) spectroscopy is a non-contact optical method used to probe the electronic structure and optical property of a material. PL is light emission from a material upon (external) optical excitation. A typical PL process in semiconductor is demonstrated in Figure 3.3. Normally, a laser (with energies greater than the semiconductor band gap) is used to excite the valence band electrons into the conduction band of the semiconductor, leaving holes in the valence band. The photo-excited electrons and holes diffuse (i.e. via intraband relaxation), and then recombine either non-radiatively by emitting phonons or transferring energy to other particles, or radiatively to emit light (photons), in the form of PL. Based on the obtained PL spectral information, the band-gap energy or defect energy levels in the semiconductor can be extracted. As PL spectroscopy is not central to this thesis, the interested reader is directed to reference [25] for further information.

In this thesis, PL measurements were performed at room temperature to determine the crystal structure of the nanowires (based on their measured PL peak position and thus the band-gap energy) and their crystal quality (by analysing the PL intensity). The optical arrangements of the PL system used in this work are shown in Figure 3.4. This setup consists of a 522 nm pulsed laser source (frequency doubled from a pulsed 1044 nm laser) with a pulse width of 300 fs and a repetition rate of 20.8 MHz, a high NA focusing objective lens, a grating spectrometer (ACTON SpectraPro 2750) providing spectral discrimination and a charge coupled device (Princeton Instruments, PIXIS) for PL spectral collection.

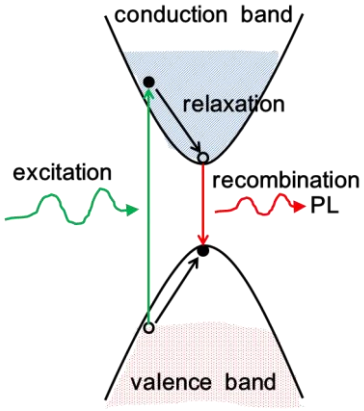

Figure 3.3: Schematic diagram of a typical PL process of semiconductors.

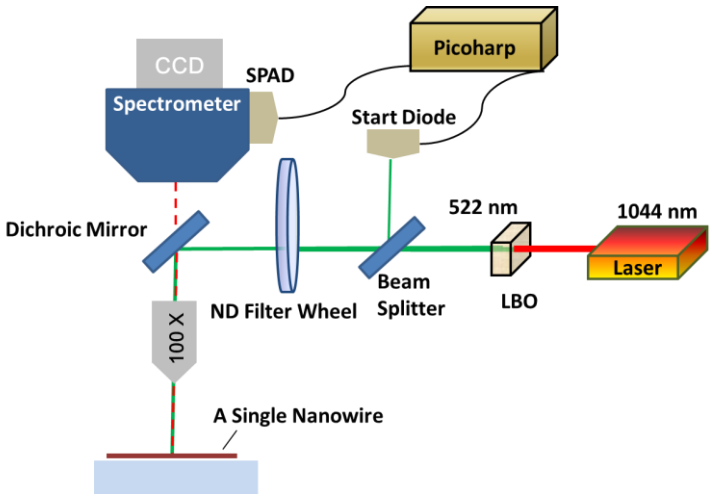

Figure 3.4: A schematic illustration of the experimental setup for PL as well as TRPL used in this work for nanowire characterisation.

In addition, a time-correlated single photon counting system is also installed in the same PL system to trace the subsequent decay in PL intensity as a function of time after optical excitation. This is called time-resolved PL (TRPL). TRPL measurement is a supplementary to normal PL measurement, allowing a further insight into the carrier recombination dynamics in materials [26]. A time resolution of ~50 ps with a maximum range of ~50 ns is achievable in this TRPL system. More details about this TRPL system have been well described in references [27] and [28]. In this thesis, TRPL was used to characterise the PL lifetime τ_{mc} (also known as minority carrier lifetime, defined as the average time that a minority carrier takes to recombine after an electron-hole generation) of the nanowires by analysing its PL intensity decay over time. Room-temperature τ_{mc} is determined by the material type, defect density and surface quality, which can be extracted by fitting the TRPL data with a mono-exponential decay curve, as expressed by

$$I_t = I_0 e^{(-t/\tau_{mc})} \tag{3.1}$$

where I_t is the PL intensity at time t and I_0 is a normalisation term. The PL lifetime is an important figure of merit for preliminary nanowire selection for THz detection (see Chapter 4).

3.2.4 Optical Pump-Terahertz Probe Spectroscopy

Optical pump-THz probe (OPTP) spectroscopy, also known as time-resolved THz spectroscopy, is used to probe the conductivity properties of a material. It is a technique based on pulsed THz time-domain spectroscopy (THz-TDS) as described in Section 2.2. In OPTP spectroscopy, the THz signal transmitted through a photo-excited sample is compared to that transmitted through the unexcited sample as a function of time. By Fourier analysis of the THz signals with and without optical excitation of the sample, frequency-dependent complex conductivity of the sample can be obtained. By further fitting the frequency-dependent conductivity spectrum using an appropriate theoretical model (i.e. Drude model), the carrier mobility, carrier density and photon-to-carrier yield of the sample can be extracted. References [29] and [30] provide more details about this technique and related analytical model. The layout of the OPTP system (at the University of Oxford) used in this thesis is shown in Figure

3.5.

Briefly, a 5 kHz 800 nm (centre wavelength) Ti: Sapphire laser amplifier with an average power of 4 W and pulse of 35 fs is used in the OPTP system. Part of this pulse is used as optical pump to photo-excite the sample (delay line 2) at a fluence of 4 μJ/cm^2/pulse. The remainder was separated into two paths. One is used to generate the THz pulse (through a GaP optical rectification crystal) as THz probe (delay line 1) and the other is to detect the THz probe (delay line 3) using a GaP electro-optic detection chip [29]. The full width at half maximum for the optical pump beam is ~ 10 mm while that for the THz probe is ~ 1 mm, to allow the two beams to spatially overlap with each other at the sample with sufficient and homogenous photo-excited carrier density. The THz electric field, *E*, is measured using the electro-optic technique via a balanced photodiode setup (see Section 2.4.1 for details) and lock-in amplifier 1 referenced to a chopper at 2.5 kHz in the THz generation beam path (delay line 1). The optical pump-induced change in the THz electric field, Δ*E*, is measured using a second lock-in amplifier 2 referenced to a chopper at 125 Hz in the optical pump beam path. By varying the time delays between all three beams, a 2D map of the THz spectral response of the sample over time after photo-excitation can be measured. In this work, nanowire samples were measured at the University of Oxford (by collaborators, Prof. Michael B. Johnston, Dr. Patrick Parkinson and Miss Jessica Boland) under identical excitation conditions at room temperature with the THz beam under vacuum. The samples were prepared by mechanical rubbing of as-grown nanowire samples onto the z-cut quartz substrates; this process was chosen to achieve a high density of nanowires on the substrate. More details of the used OPTP technique can be found in references [31-33]. In this dissertation, the OPTP measurements were used to measure the photoconductivity lifetime of each type of nanowires for further THz detector study since the photoconductivity lifetime determines the detector operation type (as described in section 2.4.2), noise level and signal processing technique required to recover the THz electric filed from the measured current in the photoconductive detectors.

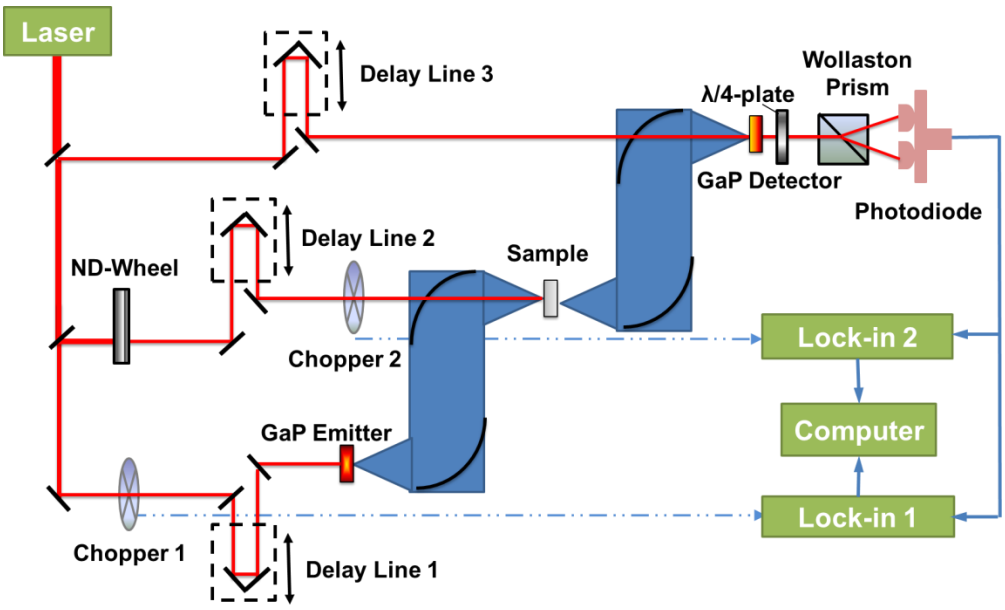

Figure 3.5: A schematic illustration of the OPTP system used in this thesis.

3.3 Single Nanowire Device Fabrication

For single nanowire device fabrication, the process can be summarised into three main steps: nanowire transfer, contact patterning and metallisation. Transfer is a process that places the nanowires onto a target substrate. Substrates could be SiO_2-on-Si substrates, glasses, quartz or plastics, determined by the requirements for device operation. Contact patterning is a process to define the device structure on the material (e.g. on a single nanowire), which is normally achieved by a lithography process involving steps such as resist spin coating, exposure and developing. Metallisation is a process (subsequent to contact patterning) associated with metal deposition and lift off to form electrical contacts onto the material. In this thesis, z-cut quartz substrate was used for THz detector fabrication since it is transparent to both optical and THz signals. SiO_2-on-Si substrates (convenient to cleave and mount onto chip packages) were used to produce test detectors for the purpose of optimising fabrication process and other optoelectronic characterisations (i.e. dark/photo I-V measurements). Two transfer methods including solution-based method for VLS nanowires and direct mechanical transfer method for SAE nanowires will be described in Chapters 4 and 6, respectively. Three different lithography tools used to pattern the single nanowire detector structures in this work will be discussed in

the following Sections 3.3.1 to 3.3.3. Electron-beam evaporation was finally used to deposit metals to form electrical contacts.

Optimisation of device fabrication process to obtain operational single nanowire devices is also important in this work. For example, it was found that the surface cleaning is key to forming low-resistivity contacts for nanowire devices. Oxygen plasma etching (to further remove the resist residue on the nanowire) followed by chemical etch (to remove the thin native oxide layer around the nanowire surface) have been added in fabrication process to provide a pristine surface for electrical contacts. A number of tests were carefully conducted in order to find out the appropriate condition for oxygen plasma etching (such as etching time, plasma pressure and intensity) and the perfect acid solution for chemical etching to specific semiconductor nanowire materials. Electrode metal type and its deposition thickness were also systemically studied for optimal contact quality and device performance. The device fabrication procedures as will be described in Chapters 5-7 are all based on the recipes after optimising.

3.3.1 Direct-Laser Writing Lithography

Direct-laser writing lithography (DLWL) is a technique used to pattern submicron-structures on a substrate by scanning the photoresist-covered substrate with a focused laser beam. In this work, a homebuilt PL system (as described in Section 3.2.3) is employed to perform DLWL (see [34] for more details), which provides a much simpler alternative to the other two techniques: EBL (requiring more sophisticated alignment processes) or ultraviolet (UV) lithography (with associated challenges in locating single nanowires and limited resolution for nano-device fabrication). A schematic diagram of the DLWL system is shown in Figure 3.6.

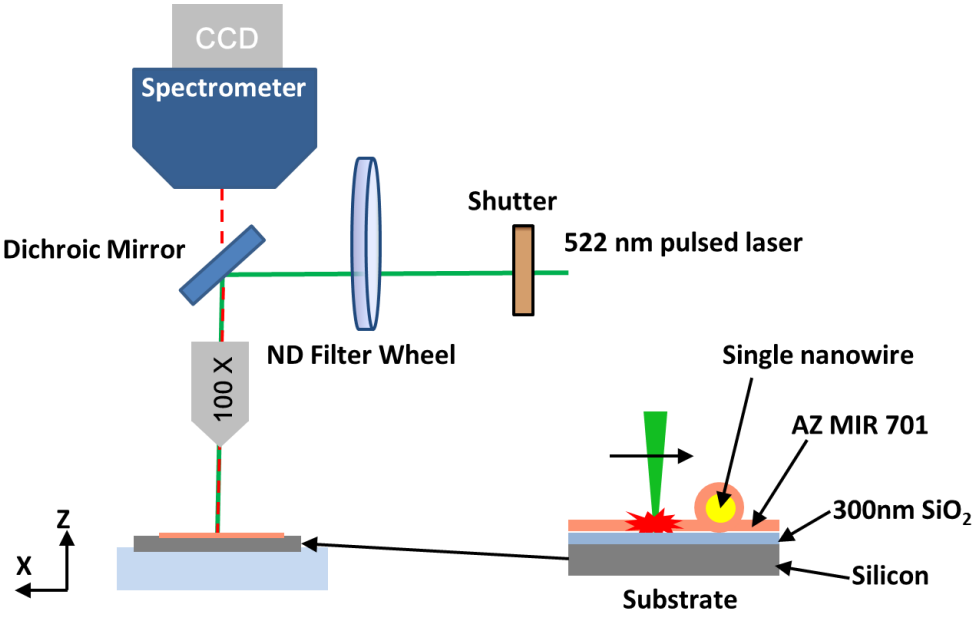

Figure 3.6: A schematic layout of the DLWL technique.

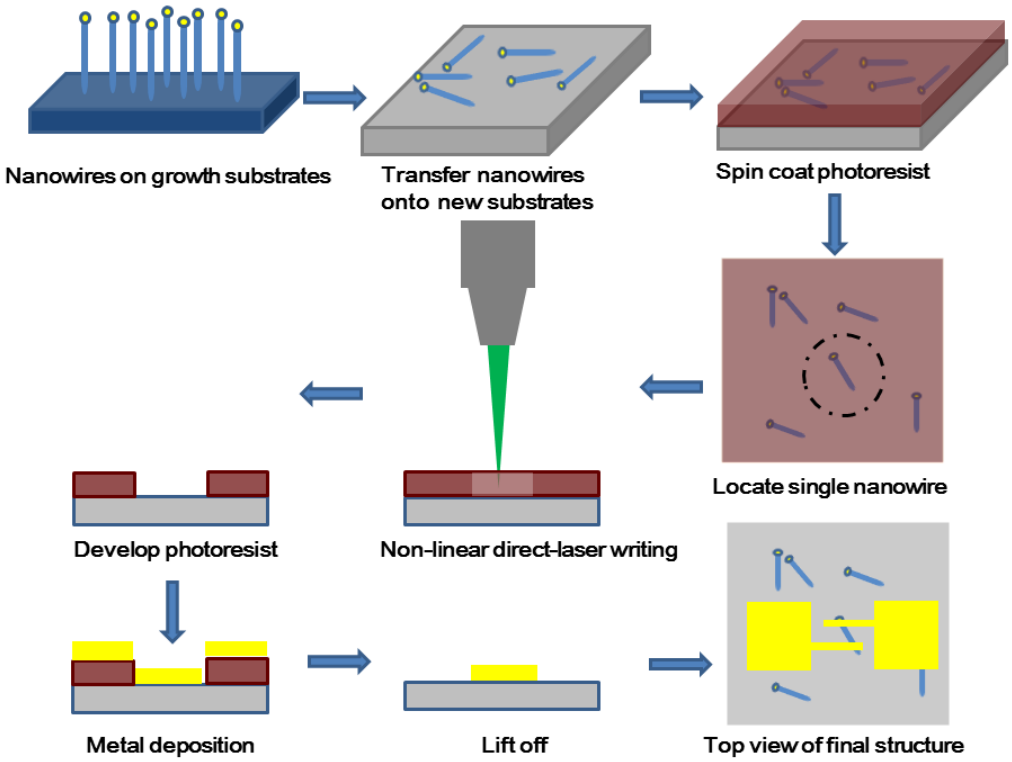

Figure 3.7: Process flow of the whole device fabrication process based on DLWL.

The steps in the fabrication of a single nanowire detector through DLWL are illustrated in Figure 3.7. Nanowires are firstly transferred from an as-grown substrate to the quartz or SiO_2-on-Si substrate. The substrate is then spin-coated with photoresist (AZ MIR 701) and placed on a motorised translation stage (with a step size of 200 nm) under an optical microscope. A computer is used to control the stage movement (along both X and Y directions) to locate the single nanowire, and to switch on the laser beam to expose the sample within a custom-defined pattern. After that, exposed photoresist is developed by developer AZ 726 MIF. Subsequently, electron-beam evaporation (Temescal BJD-2000) is performed to deposit metals on the sample, followed with a lift-off process [35] to remove the unexposed photoresist to complete the fabrication process. It is worth mentioning that the resolution of a DLWL system is limited by the laser writing beam spot size (522 nm beam source with a diameter of 650 nm as used in this thesis).

3.3.2 Ultraviolet Lithography

UV lithography is a conventional optical lithography technique widely used in microfabrication. It uses a UV light source through a photomask to define micrometre-size photoresist patterns on top of sample surfaces for subsequent device fabrication processes such as etching or lift off. Due to the limited magnification (~ ×200) and resolution (~ 2 μm as calculated from the square root of the product of the UV wavelength and the gap distance), UV lithography has limited capability for single nanowire device fabrication. However, the dimensions of the optimised THz detector contact patterns (described in Chapters 5, 6 and 7) are in millimetre size. UV lithography is suited to define such large contact patterns, despite being challenging and time-consuming to locate single nanowires as well as precisely align the mask to transfer a millimetre-size contact pattern onto a single nanowire. Figure 3.8 shows the basic UV lithography process for nanowire contacting, which involves photoresist spin coating, mask alignment, UV exposure and developing.

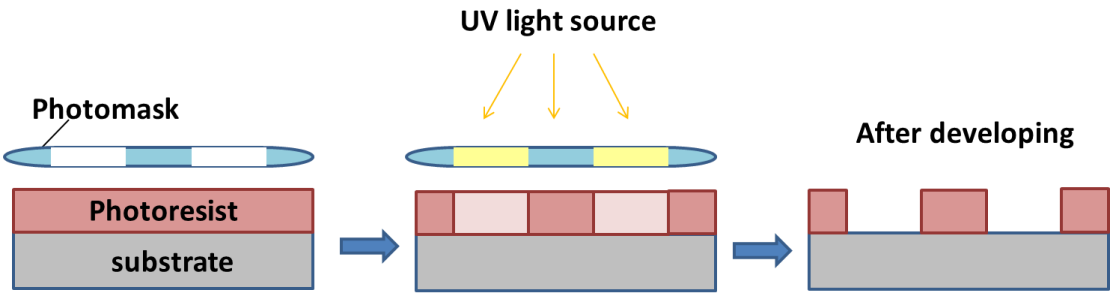

Figure 3.8: A schematic diagram of patterning process of UV photolithography.

3.3.3 Electron Beam Lithography

EBL [36] is one of the most commonly used techniques in nanofabrication, which can achieve complex pattern shapes on nano-materials and structures. It is a mask-less lithography technique similar to DLWL. Unlike DLWL using a focused laser beam, EBL is realised by scanning a sample surface covered with an electron-sensitive resist with a focused beam of electrons, whose writing resolution can reach to sub-10 nm due to the shorter wavelength of electron beams. A commercial EBL system usually combines functions of both nanolithography and analytical SEM imaging. However, compared with mask-based optical lithography, due to the long writing time the throughput of EBL is quite low which is impractical for large-scale manufacturing. To perform EBL, conducting substrates are often required to avoid charging effect. Insulating substrates (e.g. quartz) have to be coated with additional conducting layers, for instance a 5-nm Au thin film, before EBL process. In this thesis, EBL was not used to make nanowire THz detectors (on quartz substrates) but used to make four-terminal contacts of single nanowires on SiO_2-on-Si substrates for basic electrical measurements.

3.4 Device Characterisation

In order to explore the potential of III-V single nanowires for THz applications, it is important to investigate the electrical/optoelectronic properties of these nanowires, and

correlate them to their THz detection performance. As such, some basic electrical measurements on the fabricated single nanowire devices, including dark/photo current-voltage (I-V) measurement, photocurrent mapping and four-terminal I-V measurement, were performed at the Australian National University for preliminary device characterisation and selection. THz measurements were performed at the University of Oxford for THz detector characterisation from the selected devices.

3.4.1 Dark/Photo Current-Voltage Measurement

The semiconductor is a type of materials, capable of absorbing photons (with energy greater than that of its band gap) to create electron-hole pairs inside which can be driven by an external electric field resulting in a measurable current. To evaluate whether a semiconductor is suitable for use as an active material in photo-sensitive devices, characteristics of its dark/photo I-V curve are essential. Dark current refers to the relatively small current that flows through a device when there is no light exposed to it. Dark current can arise from different sources, where the two key ones include (1) thermal generation and diffusion of electrons/holes within the bulk and (2) thermal generation at the defect states. Ideally, the dark current should be as low as possible as it is the main noise source in a photo-sensitive device. Photocurrent refers to the increase of the current through the device upon light exposure. A semiconductor device with a large light to dark current ratio is highly desirable to ensure maximum sensitivity. In this thesis, dark/photo I-V measurements were carried out to evaluate the photosensitivity of the III-V nanowire devices as well as to use it as the first selection criterion for photoconductive THz detection. The dark currents were measured by using Keithley Model 6487 Picoammeter. The photocurrents were detected using a Stanford SR830 DSP lock-in amplifier, coupled with a mechanical chopper and a Stanford SR570 low-noise current pre-amplifier.

3.4.2 Photocurrent Mapping

Photocurrent mapping is also known as spatially resolved photocurrent. It is realised by scanning a photosensitive device with a focused laser beam while collecting the laser-induced photocurrent with corresponding position information. The spatial resolution of this measurement is commonly defined by the laser beam spot size (~ 650 nm as used in this thesis). The measurement setup is schematically shown in Figure 3.9. The spatial distribution of photocurrent can be obtained through this measurement, enabling us to track the origin of the photocurrents in the device. For example, photocurrent mapping has been widely used for p-n junction characterisation of semiconductor solar cells [37]. In this thesis, two-dimensional photocurrent mapping measurements were performed to examine the contact quality and contact type [38] (Ohmic/Schottky) of the fabricated single nanowire detectors.

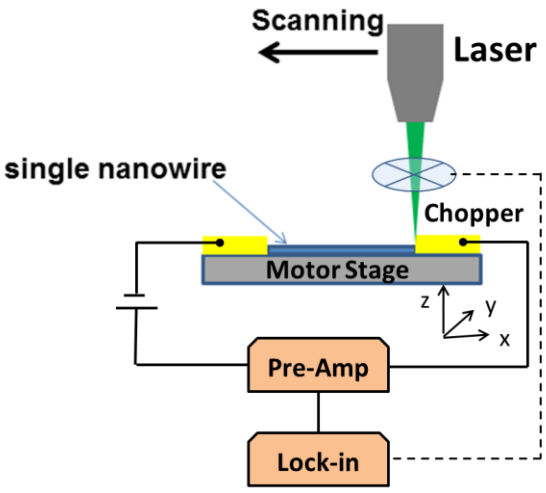

Figure 3.9: A schematic layout of the photocurrent mapping system.

3.4.3 Four-Terminal Current-Voltage Measurement

Four-terminal I-V measurement is a conventional method used to precisely measure the resistance of a material [39]. The setup for four-terminal measurement is shown in Figure 3.10, realised by applying a constant current through two outer terminals while measuring the voltage across the inner terminals. Compared to the two-terminal I-V measurement (realised by applying a constant voltage across two terminals while measuring the current through the same

two terminals), the four-terminal measurement eliminates the contribution of contact issues to the total resistance, providing higher accuracy in measured material resistance. The use of four-terminal measurement is necessary particularly when measuring devices made of a semiconductor, whose contact resistances could be comparable (or much larger) to that of the sample itself. Furthermore, an accurate resistance value for a material is important for further estimation of its carrier mobility and resultant doping concentration (see references [39] and [40] for more details). In this thesis, axial modulation-doped InP nanowires were designed and grown to optimise the THz detector performance. Four-terminal I-V measurements were performed in advance to characterise the doped nanowires for doping calibration and studying the relationship between the nanowire doping and corresponding nanowire device contact quality (as will be described in Chapter 7).

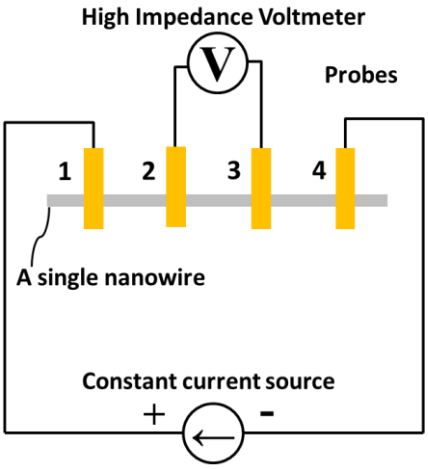

Figure 3.10: A schematic illustration of the four-terminal I-V measurement.

3.4.4 Terahertz Time-Domain Spectroscopy

The single nanowire detectors were characterised using a THz time-domain spectroscopy (THz-TDS) system [41]. The principle and optical arrangement of a THz-TDS system have been provided in Section 2.2. This section only depicts the specific setting parameters of the THz-TDS systems used in this dissertation. In brief, there were two THz-TDS systems used in this work. One was set up in 2013 (my first research trip to Oxford), and the other was set up in 2015 (my second research trip to Oxford. Details of these two THz-TDS system are shown

in Figure 3.11 and 3.12, respectively. THz-TDS data discussed in Chapter 4 were obtained from the first THz-TDS system, and data discussed in Chapters 5, 6 and 7 were from the second system. Compared to the first system, the second THz-TDS system was optimised by using a more stable femtosecond laser source with a simpler optical arrangement to reduce the difficulty in alignment for nano-size detector characterisation.

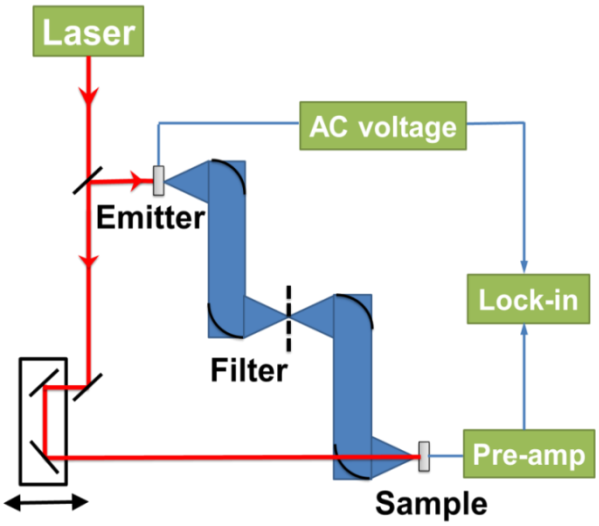

Figure 3.11: A Schematic diagram of the THz-TDS system used for the first research trip. A pulsed laser (~12 fs duration from a Ti: Sapphire oscillator with a repetition rate of 75 MHz at a centre wavelength of 800 nm) was split into two beams. A part of the laser pulse was used to excite an AC-biased 400 μm gap semi-insulating-GaAs photoconductive THz emitter, which is biased with a square wave of ± 140 V amplitude at 17 kHz. The other part of laser pulse, as a function of 'gate pulse', was directly used to excite the detector sample with a fluence of 3.9 μJ/cm^2/pulse. A delay stage was used to change the time delay between THz pulse and gate pulse.

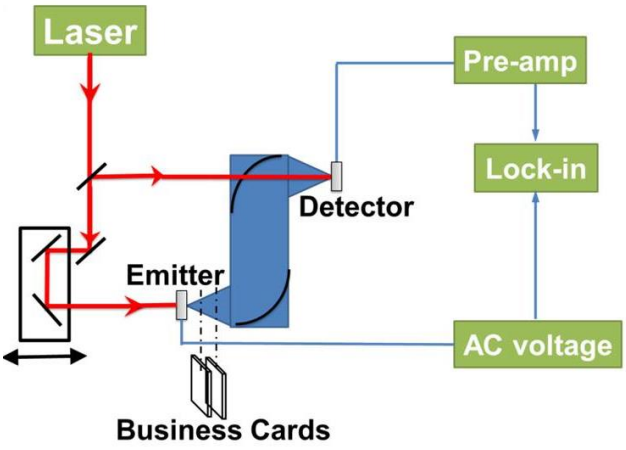

Figure 3.12: A schematic diagram of a THz-TDS system used for the second research trip. A femtosecond Ti: sapphire laser was used, which produces pulses at a centrewavelength of 800 nm with a duration of ~35 fs and a repetition rate of 84.5 MHz. The pulsed laser was split into two beams. One beam was used to excite a conventional photoconductive GaAs THz emitter, biased with a square wave of ± 400V amplitude at 17 kHz. The other beam was used to excite the detector sample at a fluence of 1.9 nJ/cm^2/pulse.

3.5 Optical Simulation for Device Design and Optimisation

Optical simulation is an important tool to complement experimental results to understand the multi-physical phenomena when light interacts with a material or structure. This work is particularly interested in the coupling effect of photoconductive antenna design (electrode structure) to the incident THz radiation. The optical characteristics of various antenna configurations were simulated in THz regime via finite-difference time-domain (FDTD) method to examine the resonant frequencies of the antenna-coupled THz detectors. All simulated results are discussed in Chapters 4, 5 and 6.

3.5.1 Maxwell's Equations

Maxwell equations describe all (classical) electromagnetic phenomena and are expressed as following:

$$\begin{aligned} \nabla \times \boldsymbol{E} &= -\frac{\partial \boldsymbol{B}}{\partial t} && (Faraday's\ law) \\ \nabla \times \boldsymbol{H} &= \boldsymbol{J} + \frac{\partial \boldsymbol{D}}{\partial t} && (Ampere's\ law) \\ \nabla \cdot \boldsymbol{D} &= \rho && (Gauss's\ law) \\ \nabla \cdot \boldsymbol{B} &= 0 && (Gauss's\ law) \end{aligned} \tag{3.2}$$

where $\boldsymbol{E}$ is the electric field, $\boldsymbol{B}$ is the magnetic flux density, $\boldsymbol{H}$ is magnetic field, $\boldsymbol{J}$ is electric current density, $\boldsymbol{D}$ is the electric flux density and ρ is the charge density.

Theoretically Maxwell's equations are able to describe the interaction between THz radiation and a metal antenna of interest. However, the experimental environment often involves complicated boundary and interface conditions, making them difficult to be solved analytically.

3.5.2 Finite-Difference Time-Domain Simulations

Finite-difference time-domain (FDTD) method is a numerical analysis technique that can solve Maxwell's equations in the time domain. The basis of the FDTD method [42] is realised via replacing the time-derivative calculation in Maxwell's equations by finite-difference approximation with second-order accuracy. The FDTD simulation technique [42-44] emerged in 1990, and has been quickly developed and applied to computationally model and solve problems involving electromagnetic wave interactions with various material structures. One advantages of this method is that it gives a wide frequency range (broadband) output from a single simulation run, and the other is its excellent scaling performance when the problem size grows.

In this work, a commercial FDTD-method Maxwell solver package, FDTD Solutions [45] developed by Lumerical©, was used to design, analyse and optimise the antenna-coupled THz detectors. The software package is operated as shown in Figure 3.13, with four main setup modules in the front panel, including structures, simulation region, sources and monitors. The structures module is used to define the physical structure and material type of the object being studied (i.e. the designed antenna that is made of gold on a quartz substrate); the simulation

region module is used to define the size, boundary condition and mesh size of the simulation, which is determined by the wavelength of incident radiation, dimensions of object being studied and desired accuracy of the results; the sources module is to define the type of incident radiation (i.e. Gaussian beam or plane wave) and related source parameters (i.e. beam profile or polarisation); the monitors module is to collect data for analysis. For a single execution of the FDTD simulation, all above-mentioned information is required to be input into the software. To make sure the simulation settings closely match the experimental conditions, all parameters used in simulations of this thesis work were based on experimental data. The detailed simulation setup will be discussed in Chapters 5.

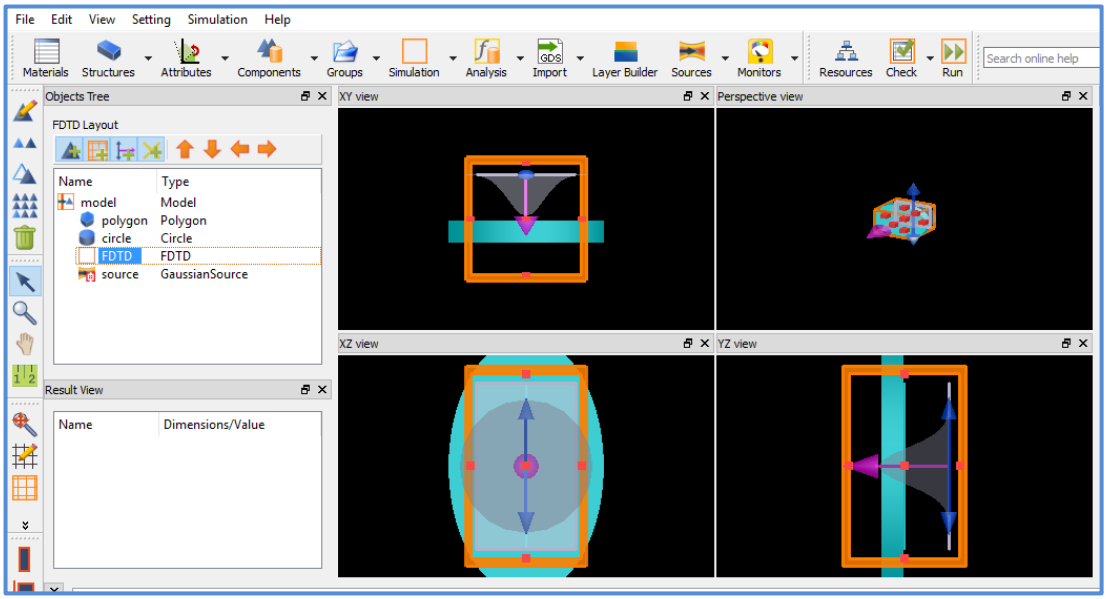

Figure 3.13.The user interface of the FDTD solutions in Lumerical. Each simulation setup module can be defined in this front panel.

3.6 Summary

The basics of nanowire growth and characterisation as well as single nanowire device fabrication and characterisation have been introduced in this chapter. For nanowire study, MOVPE was used to grow nanowires, while SEM, TEM, PL, TRPL and OPTP were used to characterise the structural, optical and conductivity properties of the nanowires. For device study, EBL, DLWL and UV lithography were used to fabricate single nanowire devices, while

dark/photo I-V measurement, photocurrent mapping, four-terminal I-V measurement and THz-TDS measurement were employed for device characterisation. This chapter also presented the optical simulation method used to examine the THz detector response characteristics studied by this thesis work.

References

[1] H. Wang, M. H. Sun, K. Ding, M. T. Hill, and C. Z. Ning, "A Top-down approach to fabrication of high quality vertical heterostructure nanowire arrays," *Nano Letters,* vol. 11, pp. 1646-1650, 2011.

[2] W. Lu and C. M. Lieber, "Nanoelectronics from the bottom up," *Nat Mater,* vol. 6, pp. 841-850, 2007.

[3] R. G. Hobbs, N. Petkov, and J. D. Holmes, "Semiconductor nanowire fabrication by bottom-up and top-down paradigms," *Chemistry of Materials,* vol. 24, pp. 1975-1991, 2012.

[4] H. J. Joyce, Q. Gao, H. H. Tan, C. Jagadish, Y. Kim, J. Zou, L. M. Smith, H. E. Jackson, J. M. Yarrison-Rice, P. Parkinson, and M. B. Johnston, "III-V semiconductor nanowires for optoelectronic device applications," *Progress in Quantum Electronics,* vol. 35, pp. 23-75, 2011.

[5] B. Mandl, J. Stangl, E. Hilner, A. A. Zakharov, K. Hillerich, A. W. Dey, L. Samuelson, G. Bauer, K. Deppert, and A. Mikkelsen, "Growth mechanism of self-catalyzed group III−V nanowires," *Nano Letters,* vol. 10, pp. 4443-4449, 2010.

[6] S. A. Fortuna and X. L. Li, "Metal-catalyzed semiconductor nanowires: a review on the control of growth directions," *Semiconductor Science and Technology,* vol. 25, 024005, 2010.

[7] A. M. Morales and C. M. Lieber, "A laser ablation method for the synthesis of crystalline semiconductor nanowires," *Science,* vol. 279, pp. 208-211, 1998.

[8] E. Janik, P. Dluzewski, S. Kret, A. Presz, H. Kirmse, W. Neumann, W. Zaleszczyk, L. T. Baczewski, A. Petroutchik, E. Dynowska, J. Sadowski, W. Caliebe, G. Karczewski, and T. Wojtowicz, "Catalytic growth of ZnTe nanowires by molecular beam epitaxy:

structural studies," *Nanotechnology,* vol. 18, 475606, 2007.

[9] K. W. Kolasinski, "Catalytic growth of nanowires: Vapor-liquid-solid, vapor-solid-solid, solution-liquid-solid and solid-liquid-solid growth," *Current Opinion in Solid State and Materials Science,* vol. 10, pp. 182-191, 2006.

[10] N. Jiang, P. Parkinson, Q. Gao, S. Breuer, H. H. Tan, J. Wong-Leung, and C. Jagadish, "Long minority carrier lifetime in Au-catalyzed GaAs/AlxGa$_{1-x}$As core-shell nanowires," *Applied Physics Letters,* vol. 101, pp. 023111-023114, 2012.

[11] N. Jiang, Q. Gao, P. Parkinson, J. Wong-Leung, S. Mokkapati, S. Breuer, H. H. Tan, C. L. Zheng, J. Etheridge, and C. Jagadish, "Enhanced minority carrier lifetimes in GaAs/AlGaAs core-shell nanowires through shell growth optimization," *Nano Letters,* vol. 13, pp. 5135-5140, 2013.

[12] E. P. A. M. Bakkers and M. A. Verheijen, "Synthesis of InP nanotubes," *Journal of the American Chemical Society,* vol. 125, pp. 3440-3441, 2003.

[13] T. Sato, Y. Kobayashi, J. Motohisa, S. Hara, and T. Fukui, "SA-MOVPE of InGaAs nanowires and their compositions studied by micro-PL measurement," *Journal of Crystal Growth,* vol. 310, pp. 5111-5113, 2008.

[14] K. Ikejiri, J. Noborisaka, S. Hara, J. Motohisa, and T. Fukui, "Mechanism of catalyst-free growth of GaAs nanowires by selective area MOVPE," *Journal of Crystal Growth,* vol. 298, pp. 616-619, 2007.

[15] J. Noborisaka, J. Motohisa, and T. Fukui, "Catalyst-free growth of GaAs nanowires by selective-area metalorganic vapor-phase epitaxy," *Applied Physics Letters,* vol. 86, 213102, 2005.

[16] K. Tomioka, T. Tanaka, S. Hara, K. Hiruma, and T. Fukui, "III-V nanowires on Si substrate: Selective-area growth and device applications," *IEEE Journal of Selected Topics in Quantum Electronics,* vol. 17, pp. 1112-1129, 2011.

[17] M. Yao, N. Huang, S. Cong, C.-Y. Chi, M. A. Seyedi, Y.-T. Lin, Y. Cao, M. L. Povinelli, P. D. Dapkus, and C. Zhou, "GaAs nanowire array solar cells with axial p-i-n junctions," *Nano Letters,* vol. 14, pp. 3293-3303, 2014.

[18] M. C. Plante and R. R. LaPierre, "Control of GaAs nanowire morphology and crystal structure," *Nanotechnology,* vol. 19, 495603, 2008.

[19] Q. Gao, V. G. Dubrovskii, P. Caroff, J. Wong-Leung, L. Li, Y. N. Guo, L. Fu, H. H. Tan, and C. Jagadish, "Simultaneous selective-area and vapor-liquid-solid growth of InP nanowire arrays," *Nano Letters*, vol. 16, pp. 4361-4367, 2016.

[20] Q. Gao, D. Saxena, F. Wang, L. Fu, S. Mokkapati, Y. A. Guo, L. Li, J. Wong-Leung, P. Caroff, H. H. Tan, and C. Jagadish, "Selective-area epitaxy of pure wurtzite InP nanowires: High quantum efficiency and room-temperature lasing," *Nano Letters*, vol. 14, pp. 5206-5211, 2014.

[21] E. Castro-Camus, L. Fu, J. Lloyd-Hughes, H. H. Tan, C. Jagadish, and M. B. Johnston, "Photoconductive response correction for detectors of terahertz radiation," *Journal of Applied Physics*, vol. 104, p. 053113, 2008.

[22] J. Goldstein, *Scanning Electron Microscopy and X-ray Microanalysis*, 3rd ed. New York: Kluwer Academic/Plenum Publishers, 2003.

[23] L. Wen Pin and C. Hsiu Ju, "Physical failure analysis cases by electron beam absorbed current & electron beam induced current detection on nano-probing SEM system," in *2010 17th IEEE International Symposium on the Physical and Failure Analysis of Integrated Circuits*, pp. 1-4, 2010.

[24] D. B. Williams and C. B. Carter, *Transmission Electron Microscopy*: Springer US, 2009.

[25] S. Perkowitz, *Optical Characterization of Semiconductors: Infrared, Raman, and Photoluminescence spectroscopy*: Elsevier, 2012.

[26] Y. Kawakami, K. Omae, A. Kaneta, K. Okamoto, T. Izumi, S. Saijou, K. Inoue, Y. Narukawa, T. Mukai, and S. Fujita, "Radiative and nonradiative recombination processes in GaN-based semiconductors," *Physica Status Solidi a-Applications and Materials Science*, vol. 183, pp. 41-50, 2001.

[27] N. Jiang, Q. Gao, P. Parkinson, J. Wong-Leung, S. Mokkapati, S. Breuer, H. H. Tan, C. L. Zheng, J. Etheridge, and C. Jagadish, "Enhanced minority carrier lifetimes in GaAs/AlGaAs core–shell nanowires through shell growth optimization," *Nano Letters*, vol. 13, pp. 5135-5140, 2013.

[28] F. Wang, Q. Gao, K. Peng, Z. Li, Z. Y. Li, Y. N. Guo, L. Fu, L. M. Smith, H. H. Tan, and C. Jagadish, "Spatially resolved doping concentration and nonradiative lifetime

profiles in single Si-doped InP nanowires using photoluminescence mapping," *Nano Letters,* vol. 15, pp. 3017-3023, 2015.

[29] J. L. Boland, S. Conesa-Boj, P. Parkinson, G. z. Tütüncüoglu, F. Matteini, D. Rüffer, A. Casadei, F. Amaduzzi, F. Jabeen, and C. L. Davies, "Modulation doping of GaAs/AlGaAs core–shell nanowires with effective defect passivation and high electron mobility," *Nano Letters,* vol. 15, pp. 1336-1342, 2015.

[30] J. J. Hannah, L. B. Jessica, L. D. Christopher, A. B. Sarwat, and B. J. Michael, "A review of the electrical properties of semiconductor nanowires: insights gained from terahertz conductivity spectroscopy," *Semiconductor Science and Technology,* vol. 31, 103003, 2016.

[31] H. J. Joyce, C. J. Docherty, Q. Gao, H. H. Tan, C. Jagadish, J. Lloyd-Hughes, L. M. Herz, and M. B. Johnston, "Electronic properties of GaAs, InAs and InP nanowires studied by terahertz spectroscopy," *Nanotechnology,* vol. 24, pp. 214006-214012, 2013.

[32] J. L. Boland, S. Conesa-Boj, P. Parkinson, G. Tütüncüoglu, F. Matteini, D. Rüffer, A. Casadei, F. Amaduzzi, F. Jabeen, C. L. Davies, H. J. Joyce, L. M. Herz, A. Fontcuberta i Morral, and M. B. Johnston, "Modulation doping of GaAs/AlGaAs core-shell nanowires with effective defect passivation and high electron mobility," *Nano Letters,* vol. 15, pp. 1336-1342, 2015.

[33] H. J. Joyce, P. Parkinson, N. Jiang, C. J. Docherty, Q. Gao, H. H. Tan, C. Jagadish, L. M. Herz, and M. B. Johnston, "Electron mobilities approaching bulk limits in 'surface-free' GaAs nanowires," *Nano Letters,* vol. 14, pp. 5989-5994, 2014.

[34] P. Parkinson, N. Jiang, Q. Gao, H. H. Tan, and C. Jagadish, "Direct-write non-linear photolithography for semiconductor nanowire characterization," *Nanotechnology,* vol. 23, pp. 335704-335708, 2012.

[35] P. Carlberg, M. Graczyk, E. L. Sarwe, I. Maximov, M. Beck, and L. Montelius, "Lift-off process for nanoimprint lithography," *Microelectronic Engineering,* vol. 67-68, pp. 203-207, 2003.

[36] Y. F. Chen, "Nanofabrication by electron beam lithography and its applications: A review," *Microelectronic Engineering,* vol. 135, pp. 57-72, 2015.

[37] P. Parkinson, Y. H. Lee, L. Fu, S. Breuer, H. H. Tan, and C. Jagadish, "Three-dimensional in situ photocurrent mapping for nanowire photovoltaics," *Nano Letters,* vol. 13, pp. 1405-1409, 2013.

[38] B. Bercu, W. Geng, O. Simonetti, S. Kostcheev, C. Sartel, V. Sallet, G. Lerondel, M. Molinari, L. Giraudet, and C. Couteau, "Characterizations of Ohmic and Schottky-behaving contacts of a single ZnO nanowire," *Nanotechnology,* vol. 24, 415202, 2013.

[39] A. S. Walton, C. S. Allen, K. Critchley, M. L. Gorzny, J. E. McKendry, R. M. D. Brydson, B. J. Hickey, and S. D. Evans, "Four-probe electrical transport measurements on individual metallic nanowires," *Nanotechnology,* vol. 18, 065204, 2007.

[40] Z. Y. Li, X. M. Yuan, L. Fu, K. Peng, F. Wang, X. Fu, P. Caroff, T. P. White, H. H. Tan, and C. Jagadish, "Room temperature GaAsSb single nanowire infrared photodetectors," *Nanotechnology,* vol. 26, 445202, 2015.

[41] K. Peng, P. Parkinson, L. Fu, Q. Gao, N. Jiang, Y. N. Guo, F. Wang, H. J. Joyce, J. L. Boland, H. H. Tan, C. Jagadish, and M. B. Johnston, "Single nanowire photoconductive terahertz detectors," *Nano Letters,* vol. 15, pp. 206-210, 2015.

[42] K. S. Kunz and R. J. Luebbers, *The Finite Difference Time Domain Method for Electromagnetics*: CRC press, 1993.

[43] T. Wang and G. W. Hohmann, "A finite-difference, time-domain solution for three-dimensional electromagnetic modeling," *Geophysics,* vol. 58, pp. 797-809, 1993.

[44] A. Taflove and S. C. Hagness, *Computational Electrodynamics*: Artech house publishers, 2000.

[45] Lumerical Solutions, Inc. http://www.lumerical.com/tcad-products/fdtd/.

Chapter 4

Photoconductive Terahertz Detectors Based on GaAs/AlGaAs Core-Shell Nanowires

4.1 Introduction

The carrier lifetimes in core-only GaAs nanowires are known to be extremely short [1], of the order of picoseconds, due to the high surface recombination velocity [2], resulting in poor performance for optoelectronic applications. Nevertheless, an ultra-short carrier lifetime in the material corresponds to an ultra-fast response time in the fabricated device, which is desirable for high-speed applications, particularly for the low-noise photoconductive detection of terahertz (THz) frequency radiation [3, 4]. Previous studies have found that the carrier lifetime and carrier mobility in GaAs nanowires can be tuned through careful control of the crystal quality [5] and surface passivation via AlGaAs shell growth [6, 7]. It is promising to grow GaAs/AlGaAs core-shell nanowires with designated properties (e.g. reasonable carrier mobility and short carrier lifetime) for low-noise photoconductive THz detection. In this chapter, single nanowire based photoconductive THz detectors are demonstrated for the first time using vapour-liquid-solid (VLS) grown GaAs/AlGaAs nanowires. The GaAs/AlGaAs single nanowire THz detectors show good signal-to-noise ratio (SNR) when compared with traditional detectors including ion-implanted photoconductive antennas and electro-optic crystals, with a detection band of 0.1-0.6 THz.

4.2 Growth and Characterisation of GaAs/AlGaAs Nanowires

In order to obtain GaAs-based nanowires suitable for THz detection, nine different types of GaAs/AlGaAs core-shell nanowires were designed and grown in this work. They were grown

on bulk GaAs substrates using the Au-assisted VLS approach with a commercial metalorganic vapour phase epitaxy (MOVPE) system [8]. These nanowires were classified into three groups, which were designed based on different growth recipes to investigate the effect of carrier lifetime and carrier mobility on detector performance. In each group, there are three types of core-shell structures differentiated by their core diameters of 50, 100, 150 nm, respectively. The first group - group A - had a high-quality, monotypic zinc blende (ZB) stacking-fault free GaAs core covered by an AlGaAs Shell. Both the second and third groups - groups B and C - were intentionally grown to have a low-quality GaAs core incorporating stacking faults and defects known to reduce the carrier mobility and lifetime; however the group C while having the same quality core (as that of group B) had a thinner AlGaAs shell (when compared to groups A and B). An additional GaAs cap was grown outside the AlGaAs shell for all nanowires to prevent the oxidation of the shell. Details of the growth method are depicted in following Section 4.2.1.

4.2.1 Growth Details

The GaAs/AlGaAs core-shell nanowires were grown on semi-insulating GaAs (111)B substrates in an MOVPE reactor (AIXTRON 200/4) at a pressure of 100 mbar and a total gas flow rate of 15 litres/min. Trimethylgallium (TMG), trimethylaluminium (TMAl), and arsine (AsH_3) were used as the Ga, Al and As source materials, respectively. Au nanoparticles of 50, 100 and 150 nm in diameter were used as catalysts and dispersed onto the GaAs substrates prior to growth. The substrates with Au nanoparticles were firstly annealed at 600 °C for 10 minutes under AsH_3 ambient to desorb surface contaminants prior to nanowire growth. After cooling to the desired temperature, TMG was switched on to initiate nanowire growth. The GaAs core of group A was grown by a two-temperature procedure developed previously by the Australian National University group [5, 6, 8], which has significant advantages in minimising undesirable tapering and eliminating twin defects to provide a high quality GaAs core. The growth was initiated at 450 °C with a 1 min “nucleation” step followed by a prolonged (120 min) growth at 375 °C. Source flows of TMG and AsH_3 were 1.2×10^{-5} and 5.4×10^{-4} mol/min, respectively. The GaAs core of groups B and C were grown by a single-temperature fast

growth rate procedure (450 °C for 30 min) [10], where the source flows of both TMG and AsH_3 were increased by a factor of 4. After the GaAs core growth, TMG was switched off and the growth temperature was ramped to 750 °C in an AsH_3 ambient. An AlGaAs shell and a GaAs cap layers were then grown at this temperature according to the optimised procedure previously developed [8]. Both group A and B have the same growth time (and thus similar thickness) for AlGaAs shell, whereas group C has a shorter growth time for AlGaAs shell leading to thinner shell. Finally, the nanowires were terminated by GaAs capping layer growth at the same growth time for all the three sets of samples. A summary of the key growth parameters are presented in Table 4.1.

Table 4.1: Details of the growth conditions for the three different groups of nanowires used for the THz detectors.

	GaAs core		**AlGaAs shell**	**GaAs cap**
Group	**Au catalyst (nm)**	**Growth time**	**Growth time**	**Growth time**
A	150	1 min 450°C, 120 min 375°C (1 time precursor flow)	3min 45s, 750 °C	1min, 750 °C
	100			
	50			
B	150	30 min 450°C (4 times precursor flow)	3min 45s, 750 °C	
	100			
	50			
C	150	30 min 450°C (4 times precursor flow)	1min 30s, 750 °C	
	100			
	50			

4.2.2 Material Characterisation

To identify the best core-shell nanowire structure for THz photoconductive detection, preliminary characterisation of the nanowires was carried out at the Australian National University. The carrier lifetime, carrier mobility and dark resistivity are the three most critical material properties for photoconductive THz detection, since the photoconductivity rise time determines speed and detection bandwidth of the device, the carrier lifetime determines the detector operation type and noise level, while the mobility and resistivity contribute to the

detector response level and sensitivity [4]. In this chapter, in addition to the commonly used scanning electron microscopy (SEM) and transmission electron microscopy (TEM) techniques for morphology and structural characterisation, three types of measurements including photoluminescence (PL) lifetime, photocurrent and dark current, were chosen to evaluate the carrier lifetime, carrier mobility and dark resistivity of nanowires. The PL lifetime (which is essentially the minority carrier lifetime) can be approximated as the carrier lifetime within the material that can be measured via time-resolved PL (TRPL). It is challenging to directly measure the carrier mobility for semiconductor nanowires (particularly for single nanowires) due to the small material volume involved and thus limited techniques. As such, the photocurrent is measured to evaluate the carrier mobility. Since the photocurrent is related to the product of the carrier density, mobility and lifetime of the material, a high photocurrent is often a good indication for high carrier mobility. Dark current is inversely proportional to the dark resistivity of the material. Therefore, nanowires with a relatively short PL lifetime, high photocurrent and low dark current are considered favourable for THz detection.

4.2.2.1 Scanning/Transmission Electron Microscopy

After growth, the morphologies of the GaAs/AlGaAs nanowires were firstly characterised by employing SEM, and their core-shell structural characteristics were studied by TEM for the nanowire cross sections. The cross-sectional samples were prepared by embedding the nanowires into an epoxy resin and then cutting into thin sections (30 nm in thickness) by ultramicrotomy. High-angle annular dark-field images with atomic number contrast were taken by TEM, where the core-shell structure can be clearly identified with the AlGaAs shell exhibiting a darker contrast than the GaAs core and cap layer. GaAs/AlGaAs nanowires with a diameter of 150 nm from groups A, B and C are used as representative samples for examining the microstructure. Figure 4.1 shows that the three types of nanowires have a core-shell-cap structure with a 150 nm diameter GaAs core, an AlGaAs shell of 28 nm (namely Groups A and B) or 5 nm (namely Group C) thickness and a thin GaAs cap layer (to prevent the oxidation of the AlGaAs shell), with an average length of around 13 μm (Group A) or 23 μm (Groups B and C). The doubled nanowire length of Group B and Group C is due to the 4-time precursor flow

used for growth. The less tapered nanowire morphology of Group A (compared with Groups B and C) is due to the use of an optimised two-temperature growth [5, 6, 8] recipe.

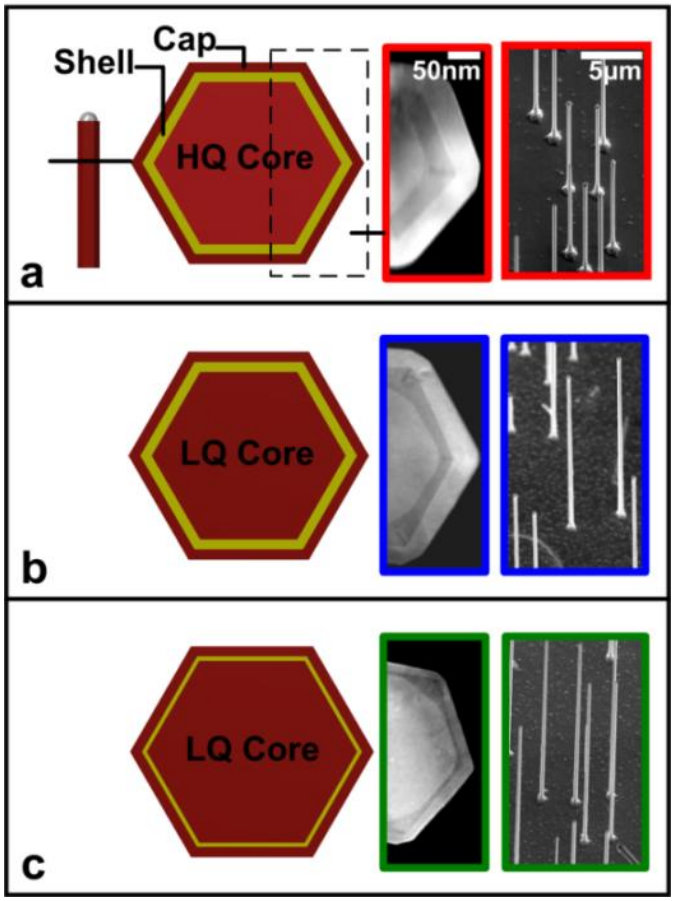

Figure 4.1: Electron micrograph images of the GaAs/AlGaAs nanowire samples. Schematic cross-sections (left) of the GaAs/AlGaAs core-shell nanowire used in this study. Typical cross-sectional TEM (centre) and SEM (right) images of the three types of nanowire samples grown with either high quality (HQ) or low quality (LQ) GaAs cores with a diameter of 150 nm (the SEM images were taken with the surface tilted at 52° to the electron beam).

4.2.2.2 Photoluminescence and Time-Resolved Photoluminescence

PL measurements were performed at room temperature to investigate the optical quality of the GaAs/AlGaAs nanowires, as shown in Figure 4.2(a). Again, the GaAs/AlGaAs nanowires with a diameter of 150 nm from groups A, B and C (namely Groups A, B and C, respectively) are used as examples. PL emission peaks from the three types of GaAs/AlGaAs nanowires can

be observed at ~ 1.425 eV (band-gap energy of ZB GaAs), indicating they are of ZB crystal structure. As expected the nanowire from Group A shows the strongest PL emission due to the improved crystal quality of the GaAs core achieved by using the two-temperature growth technique [5, 6]. Group C shows the weakest PL emission, caused by the defective GaAs core grown using single temperature [9] and the poor GaAs/ AlGaAs interface quality arising from its very thin AlGaAs shell (that is not sufficient to passivate GaAs). TRPL measurements at room temperature were also investigated for these GaAs/AlGaAs nanowires, as shown in Figure 4.2(b). The PL lifetimes, measured at the PL peak energy of 1.425 eV, are 340 ps, 70 ps and 90 ps for nanowires from Groups A, B and C, respectively.

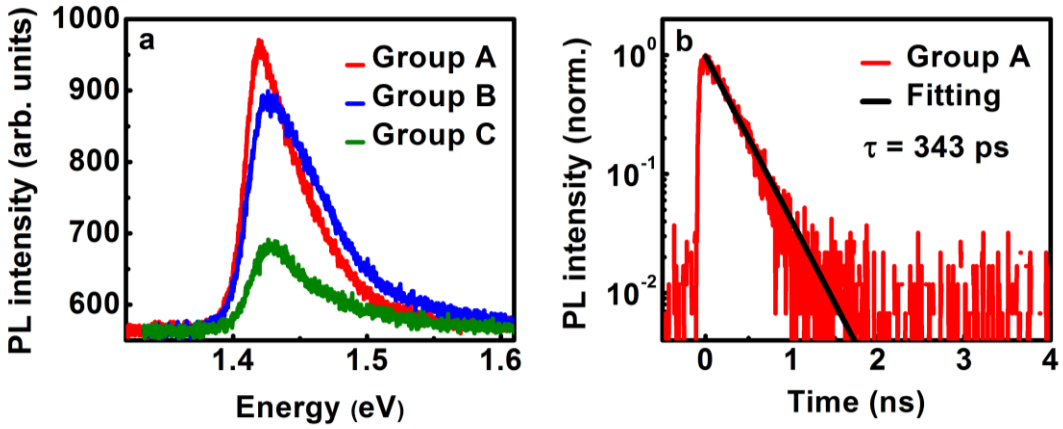

Figure 4.2: (a) Typical room-temperature PL spectra of single GaAs/AlGaAs core-shell nanowires (with core diameter of 150 nm) studied in this work. (b) The TRPL decay of a single GaAs/AlGaAs nanowire.

4.3 Detector Fabrication and Characterisation

The optical properties studied from different types of nanowires can, to a certain extent, reveal their potential for application in optoelectronic devices. It is essential to study the actual electrical/optoelectronic properties of the nanowire devices, to correlate them with their performances as photoconductive THz detectors. In this section, the electrical/optoelectronic properties of GaAs/AlGaAs single nanowire devices were investigated under direct-current (DC) measurements, which were then correlated with their THz response performance.

4.3.1 Device Fabrication

Single nanowire THz detectors were fabricated using a custom-designed direct-laser writing lithography (DLWL) technique (as described in Section 3.3.1), allowing electrical contacts to be made to single nanowires on quartz substrates. At first, small pieces of substrate were cleaved from the as-grown wafers of the nanowire sample and placed in isopropyl alcohol for a 30-second ultra-sonication, to transfer the nanowires from the GaAs substrate to the solution. The solution was dropped onto z-cut quartz substrates and allowed to dry naturally. The z-cut quartz was used as the detector substrate as it is an electrical insulator and transparent to THz radiations. The THz detector structures were then patterned using DLWL [10]. After contact pattern development, an oxygen plasma etch was employed for further removal of the photoresist residue on the nanowires, followed by a 4% HCl chemical etch to remove a thin native oxide layer from the nanowire surface. The device structures were finally metallised using electron beam evaporation and lift off to form Ti/Au (10 nm/300 nm) contacts on each side of the nanowires.

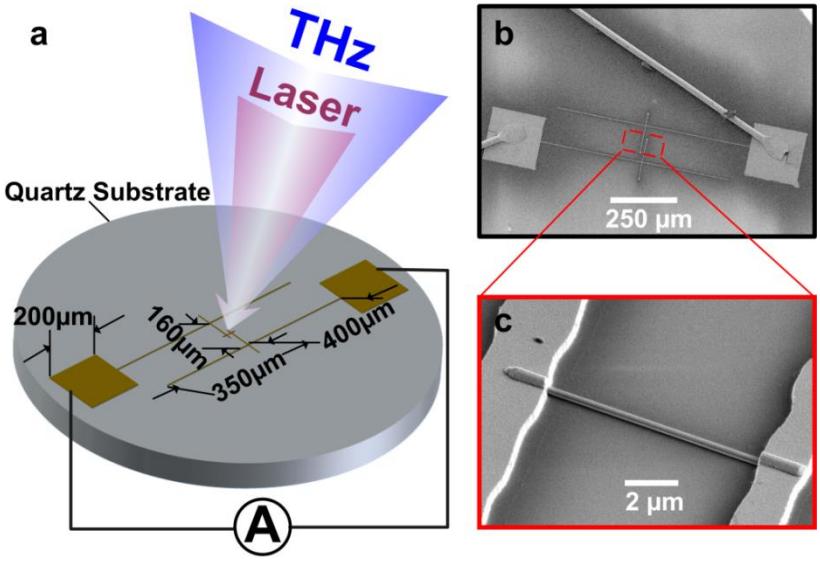

Figure 4.3: Schematic demonstration of the THz detector design (a) and SEM images of the fabricated detector under low (b) and high (c) magnifications.

The schematic structure and dimensions of the fabricated detector is shown in Figure 4.3, along with a typical SEM image of a complete single nanowire device. Two large square pads

(200 μm × 200 μm) were designed to allow for wire-bonding to make electrical connections (with external measurement equipment), which were set far away from the centre area of the detector to eliminate undesired coupling effects between the incident THz radiation and electrode structures. However, it turns out that such design still affects the resonance characteristics of the detector, as will be discussed in Section 4.4.5.

4.3.2 Dark/Photo Current-Voltage Measurement and Photocurrent Mapping

The dark/photo current-voltage (I-V) measurements at room temperature were performed to confirm the contact quality of the fabricated detectors. The detectors made of GaAs/AlGaAs nanowires with a diameter of 150 nm from groups A, B and C (namely Group A, B and C, respectively) are used as examples. It can be seen from Figure 4.4(a), that all three types of nanowire detectors show a very low dark current (sub-nA), and a clear photo-response under different biases; the nanowire detector from Group A exhibits the strongest light response, with photocurrent exceeding 100 nA when biased at 4 V, confirming the superior electrical properties arising from the high material quality due to the two-temperature growth technique; while nanowire detector from Group B which possesses the shortest PL lifetime has a better photo-response (10s of nA at 4 V) when compared with Group C (a few nA at 4 V). In general, all nine types of nanowire detectors show near-Ohmic responses; however, a few are not so linear, most likely due to contact imperfections. Furthermore, 2-dimensional photocurrent mapping was performed. As clearly confirmed from Fig. 4.4(c), the photocurrents measured from the single nanowire detector mainly originated from the nanowire itself (rather than the contact junction), as a result of good contact quality to these nanowire detectors.

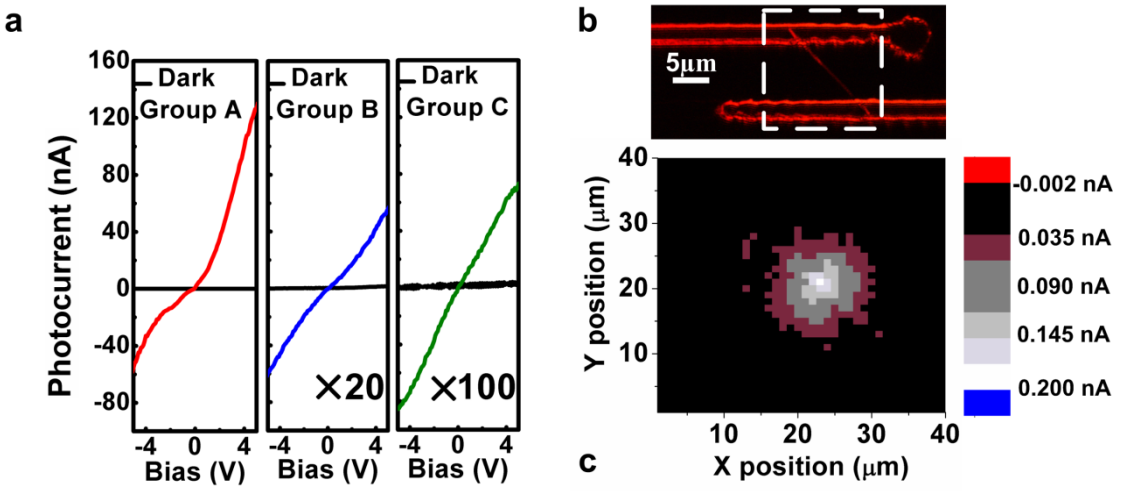

Figure 4.4: (a) Photocurrent measured for different types of detector, under illumination with a pulsed laser (522 nm centre wavelength, 300 fs duration and 20 MHz repetition rate) and a fluence of 0.8 mJ/cm^2/pulse; (b) A typical dark-field optical image of the centre part of the detector with a nanowire contacted; (c) 2-dimension photocurrent mapping for the contacted single nanowire in (b), under illumination from a green pulsed laser at a fluence of 0.5 mJ/cm^2/pulse (spot size is 650 nm in diameter), biased at 3V. The 2-dimensional scanning area is indicated by the white dashed box in (b).

4.4 Selection for Terahertz Detection

A summary of the basic optical/electrical/optoelectronic measurement results for all nine types of nanowires and corresponding single nanowire detectors are shown in Table 4.2. Nanowires with the largest core diameter of 150 nm (highlighted in Table 4.2) met the criteria in each group, having the highest photocurrent response while coupling with a short PL lifetime and low dark current at sub-nA level. Therefore, three types of GaAs/AlGaAs nanowires with core diameter of 150 nm - sample A, B, C (named after their group name) - were chosen for further investigation at the University of Oxford for THz measurements.

Table 4.2: Characterisation and selection of the GaAs/AlGaAs nanowires used to fabricate THz detectors (statistical average). N/A refers to 'unmeasurable' (signal is too weak for PL and TRPL measurements). PL spectra and photocurrents were measured under illumination with a pulsed 522 nm laser at a fluence of 2.8 μJ/cm^2/pulse and 0.8 mJ/cm^2/pulse (biased at 8 V), respectively.

Nanowire Type		**PL Measurement**		**Dark/photocurrent I-V Measurement**	
Group	**Core Diameter (nm)**	**Peak Position (nm)**	**Lifetime (ps)**	**Dark Current (A)**	**Photocurrent/Dark Current Ratio**
A	150	873.5	300	10^{-10}	1000
	100	874.5	830	10^{-11}	100
	50	865.8	220	10^{-11}	100
B	150	869.6	70	10^{-10}	100
	100	868.4	100	10^{-10}	10
	50	N/A	N/A	10^{-11}	10
C	150	866.4	90	10^{-10}	100
	100	868.5	55	10^{-11}	10
	50	N/A	N/A	10^{-11}	1

4.5 Terahertz Measurements

4.5.1 Optical Pump-Terahertz Probe Spectroscopy

A time-domain optical pump-THz probe (OPTP) spectroscopy system [11, 12] was used to measure the photoconductivity rise time and conductivity lifetime of an ensemble of nanowires from samples A, B and C, as shown in Figure 4.5. More details of this measurement have been described in Section 3.2.4. Ultrafast photo-excitation at 800 nm (1.55 eV) was chosen to match the excitation conditions used under device operating conditions. It is noted that the ultimate temporal resolution of a photoconductive THz detector is set by the photoconductivity rise time, and is much less than 1 ps for all samples. A bi-exponential carrier decay was observed for all samples, including a fast component (τ_f) due to recombination in the unpassivated GaAs capping layer, and a slower recombination (τ_s) in the GaAs core, ranging from 4.6 ± 1 ns

(sample A) to 800 ± 30 ps (sample B). Sample C exhibits a much larger early time fast carrier decay, which may arise from carrier tunnelling through the thin AlGaAs shell layer to the highly defective capping layer as in accordance with the investigation on AlGaAs passivation [13]. All the three types of nanowires have long conductivity lifetimes (>> 1ps), indicating that they are of integrating detector type. Discussions on detector type and related signal processing technique can be found in Section 2.4.2.

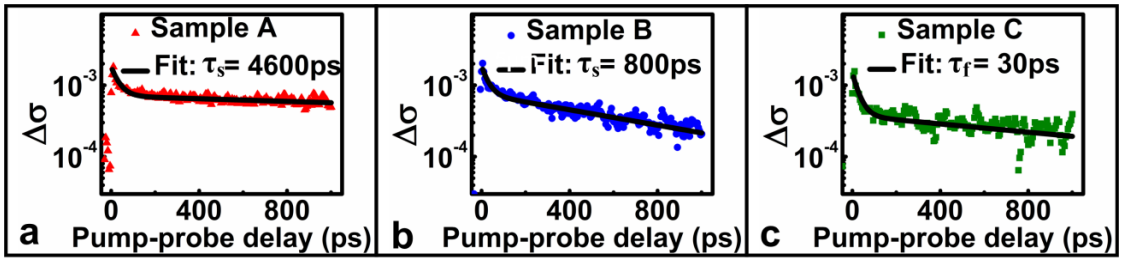

Figure 4.5: OPTP photoconductivity decays of the nanowire samples. Solid black lines are a bi-exponential fit to the data. The labels show the dominant carrier lifetime for each sample.

It is worth noting that the photoconductivity lifetimes for these GaAs/AlGaAs nanowires (sample A and B) are much longer than their PL lifetimes (see Table 4.2 in Section 4.4). To understand this phenomenon, PL lifetime and photoconductivity lifetime were compared and discussed. PL lifetime is the average time during which the electrons and holes are simultaneously free, and able to diffuse, and is therefore dependent on the electron-hole recombination time such as defect recombination and band-to-band recombination lifetimes in the III-V nanowires. Photoconductivity lifetime is the lifetime during which at least one type of charge carrier remains free to carry current. So photoconductivity lifetime not only includes PL lifetime but also includes the time during which a charge carrier spends at a trapping centre (or in a bound state). In this work, the interface between the AlGaAs shell and GaAs core (cap) in the GaAs/AlGaAs nanowires may form a large number of defect centres to trap the photo-generated charge carriers, resulting in a spatial separation of electrons and holes within the nanowires [14]. This spatial separation of electrons and holes can cause a rapid PL quenching (leading to a short PL lifetime) while allowing a long photoconductivity lifetime as spatially separated electrons and holes still contribute to conduction. Additionally, the complex nature of the core/shell/cap interfaces in GaAs/AlGaAs nanowires further complicates the

optical and electrical properties of the nanowires, leading to a weak dependence of PL lifetime on nanowire diameter (as shown in Table 4.2).

PL lifetime reflects the optical quality of the material. Photoconductivity lifetime, on the other hand, is further related to electrical and conductivity properties of the material, which determines the actual magnitude of the response current in the fabricated detector. In this dissertation, it is believed that photoconductivity lifetime is a more accurate measure of evaluation of the suitability of nanowires for THz detection, since the photoconductive nanowire THz detector works as an electronic device and produces electrical responses to the incident THz signal.

4.5.2 THz Detector Performance

The single nanowire detectors were finally characterised using a THz time-domain spectroscopy (THz-TDS) system [11], to study and analyse their THz response performances with respect to time, frequency and polarisation of the incident THz radiation. More details of this THz-TDS system are given in Section 3.4.4 (see Figure 3.11). Six nanowire detectors from sample A (A1-A6), and six from sample B (B1-B6) and one from sample C (C1) were successfully measured. The nanowire samples gave highly repeatable results as shown in Figure 4.6. A high degree of uniformity in response is observed within each nanowire batch, both in terms of peak current (on the left of Figure 4.6), and in terms of spectral response (on the right of Figure 4.6).

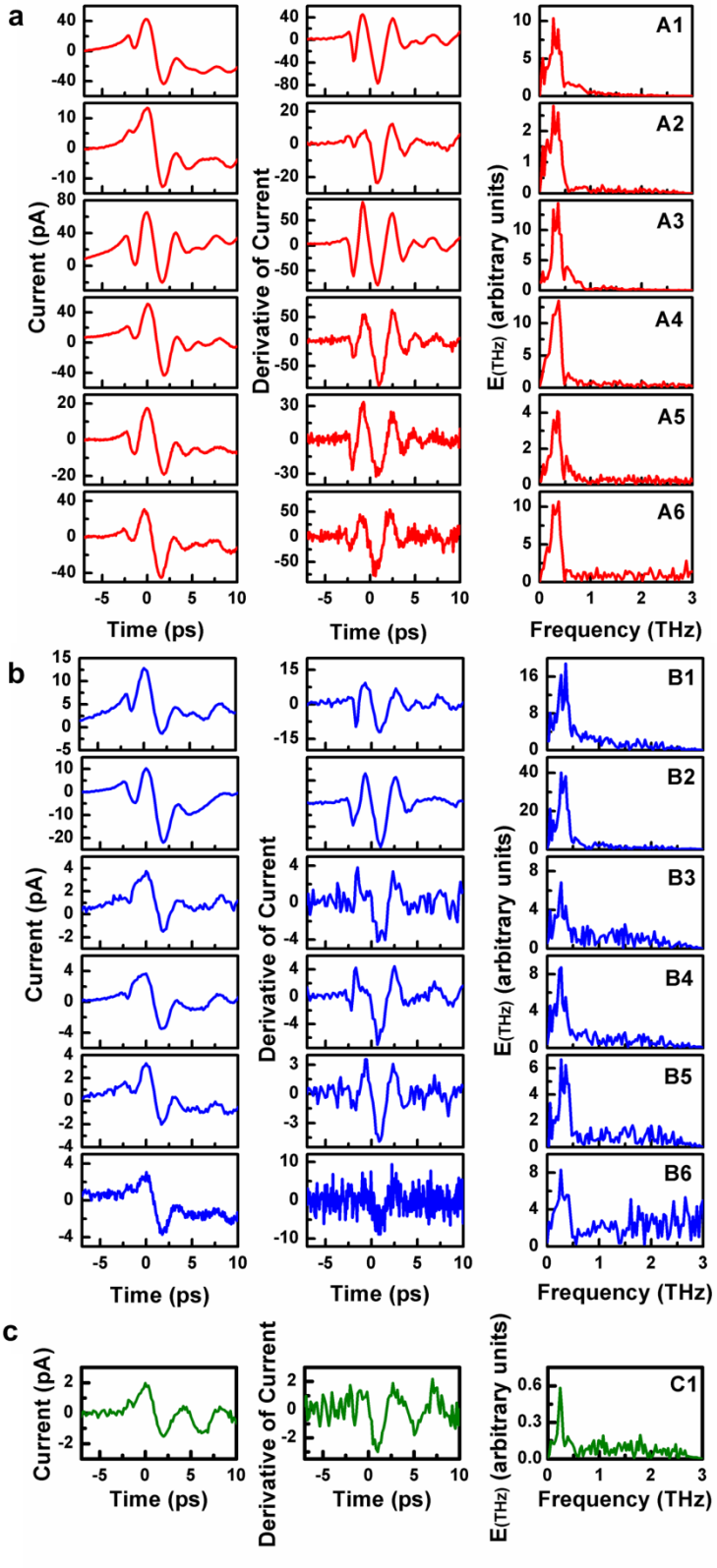

Figure 4.6: THz responses of single GaAs/AlGaAs nanowire detectors, from (a) sample A (red), (b) sample B (blue) and (c) sample C (green). Left: unprocessed THz-induced current. Centre: calculated time-domain electric field. Right: amplitude frequency spectrum of the detector.

The THz detector performance for samples A, B and C are compared in Figure 4.7 (a). All devices produced pA-level responses with the detectors incorporating nanowires from samples A and C exhibiting the best and worst SNR respectively, which is consistent with results from their photocurrent measurements (in Section 4.3.2) and PL measurements (in Section 4.2.2.2). This indicates that PL intensity, magnitude of photocurrent response and magnitude of photoconductive THz response are closely correlated. Since there are significant similarities in response of the three detectors, all remaining measurements in this chapter will be focused on sample A, which presents the best detector performance. A standard electro-optic detection crystal (ZnTe) was used as a reference detector to measure the electric field of the THz source, while a photoconductive receiver (ion-implanted InP with a bow-tie antenna structure [11]) was used as a reference in comparison with the single nanowire detectors. The transient THz electric field measured by the two bulk reference detectors and sample A, and their calculated spectral response are shown in Figure 4.7(b)-(d) and Figures 4.7(e)-(g), respectively. Despite that the signal measured using the nanowire has a lower bandwidth in the range of 0.1-0.6 THz; it shows sufficient SNR for practical use.

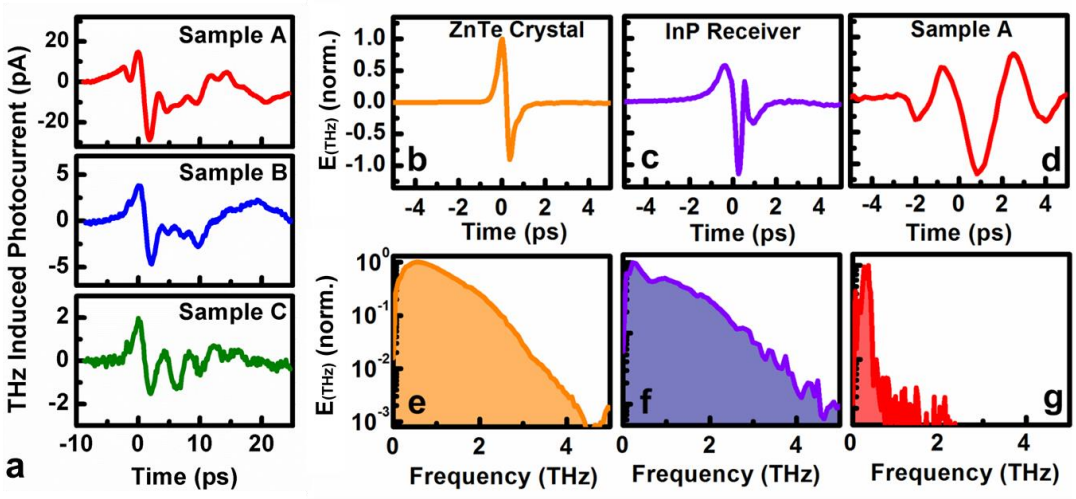

Figure 4.7: THz time-domain spectroscopy characterisation of fabricated devices. (a) Unprocessed time-domain THz-induced currents obtained from the nanowire detectors (samples A, B and C). (b-d) Processed and normalised THz electric field as measured by (b) a reference electro-optic sampling detector, (c) a reference InP photoconductive receiver and (d) sample A. (e-g) THz amplitude spectra corresponding to the electric field signals in (b-d).

To assess the performance of the GaAs/AlGaAs nanowire detectors for real-world applications, a 290 GHz inductive mesh low-pass filter was inserted into the THz path. Figure 4.8 shows the THz responses from the nanowire detector made of sample A and the InP photoconductive receiver, without (red) and with (blue) the presence of the low-pass filter. It can be seen that similar cut-off edge and transmitted signal amplitude (around 80%) for both detectors. When compared with the traditional (bulk) THz detectors, such nanoscale devices bring many advantages for future applications whenever size or spatial resolution is critical [15, 16].

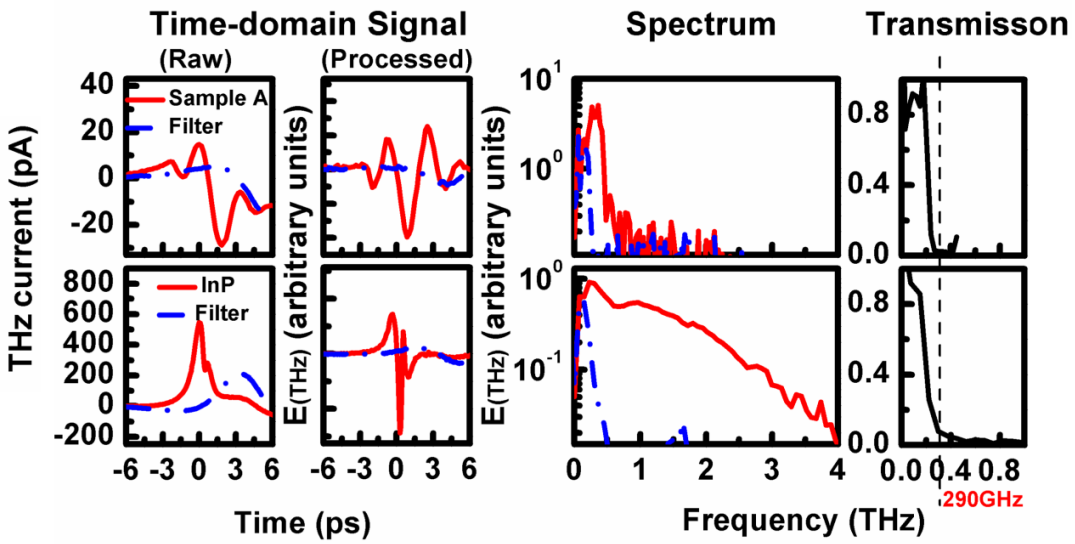

Figure 4.8: Comparative performance of (upper) nanowire-based and (lower) traditional THz photoconductive detectors. Left: raw and processed time-domain THz electric field. Centre: amplitude spectrum of THz electric field. Right: change in transmission due to the low-pass filter (Red solid line: without filter. Blue solid line: with low-pass filter. Black dashed line: cut-off frequency at 290 GHz).

4.4.5 Finite-Difference Time-Domain Simulation

In order to understand the nature of response characteristics of the photoconductive THz detector and find out the origin of the narrow detection bandwidth of the single nanowire photoconductive THz detectors, optical simulations were carried out using Lumerical finite-difference time-domain (FDTD) solutions in the THz regime and compared with

experimental results. FDTD simulations were set up using the same geometry used in experiments, as shown in Figure 4.9. Further details of the simulations will be described in Chapter 5.

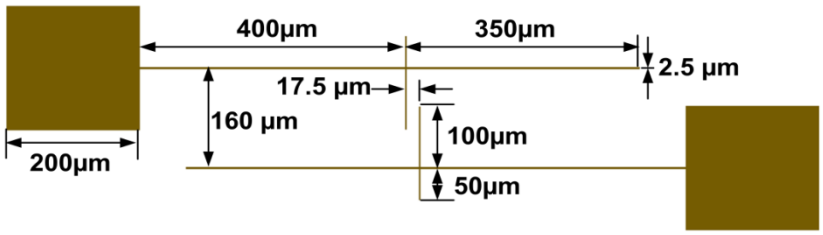

Figure 4.9: Detector geometry used for FDTD simulations.

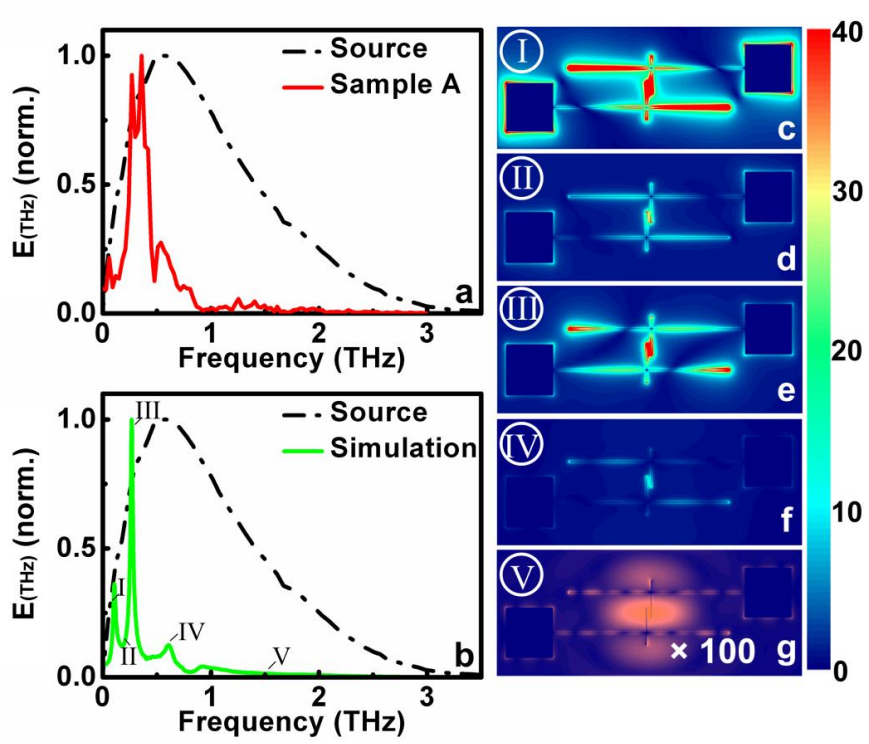

Figure 4.10: FDTD simulation of frequency response for the two-pad detector structure. (a) Experimentally determined amplitude spectrum of THz electric field transient obtained using sample A, (b) FDTD simulated spectrum. (c - g) THz electric field distribution at five different frequencies including I : 0.11 THz; II: 0.18 THz; III: 0.27 THz; IV: 0.61 THz and V: 1.5 THz.

Figure 4.10(a) shows the experimental amplitude spectrum of the THz electric field, while

Figure 4.10(b) shows the simulated spectrum monitored at the centre of the antenna with the same geometry as used in the experiment. It can be seen that the geometry of the detector has a great impact on the detected THz spectral profile, leading to enhancement of the electric field at specific resonant frequencies. Figure 4.10(c)-(g) show the THz electric field distribution on the antenna structure for five individual frequencies; it is clear that at frequencies 'I' (0.11 THz) and 'III' (0.27 THz), the THz electric fields are strongly enhanced at the centre of antenna, where the single nanowire is located. In contrast, there is very little field enhancement at the frequency 'V' (1.5 THz). It is noted that the experimental spectrum is well consistent with the simulated spectrum, showing similar bandwidth (0.1-0.6 THz) with three electric-field-enhanced peaks. This indicates that the detection bandwidth is in fact limited by detector design rather than the nanowire itself. In the future, a specific device geometry designed and optimised by FDTD simulations may be used to tune the resonance frequency range of the detector.

4.4.6 Polarisation Sensitivity

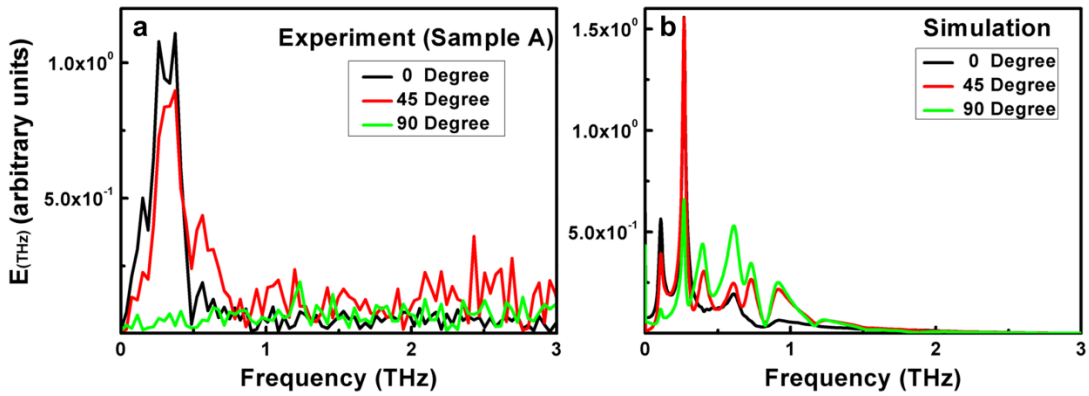

Figure 4.11: Polarisation-dependent THz response for the detector structure. (a) Experimental amplitude frequency spectrum obtained using detectors made of sample A. (b) FDTD simulated resonant frequency spectrum. The polarisations of THz electric field were set at 0, 45 and 90 degrees respectively (from direction parallel to perpendicular to the nanowire axis).

All above mentioned experiments and simulations were performed at normal incidence, and

the polarisation of the incident THz electric field was linear, aligned parallel to the nanowire axis. Considering the unique one-dimensional geometry of a single nanowire, polarisation-dependent THz measurements on the single nanowire detectors were studied. To change the polarisation of the incident THz electric field, the THz emitter was manually rotated by 45 degrees and 90 degrees, respectively. Figure 4.11(a) shows the THz responses obtained from a single GaAs/AlGaAs nanowire detector before and after rotating the emitter. Polarisation-dependent FDTD simulations were also performed to compare with experimental results as shown in Figure 4.11(b), since the device geometry may contribute to the polarisation-related response characteristics. It can be seen that, when the polarisation of the incident THz electric field is changed from parallel (to the nanowire axis) to perpendicular, the magnitude of the measured THz response for the single nanowire THz detector decreased from maximum to zero with the strongest resonant peak in the response spectrum changed from low- to high-frequency. The change in response magnitude can be attributed to the optical absorption anisotropy of the one-dimensional detector to THz radiation, and the strongest resonant peak shift in the response spectrum is most likely caused by polarisation-related resonance sensitivity of the device geometry. Figure 4.11(b) proves that the intensity change of the resonance peaks in response spectrum arises from the device geometry. However, the simulated result still shows a response to the incident THz radiation when THz polarisation is perpendicular to the gap of device geometry, in contrast to the experimental result where the single nanowire detector shows zero response under the same incident condition due to the anisotropic optical absorption of the nanowire. Figure 4.11(b) also indicates that the device geometry itself can be independently sensitive to the incident THz polarisation, influencing both amplitude and strongest resonant peak in response spectrum. Therefore it is of great promise to use single nanowires (combined with an optimised device design) to realise highly polarisation-sensitive photoconductive THz detectors.

4.5 Summary

Various VLS-growth single GaAs/AlGaAs nanowire structures were designed and grown by MOVPE. The morphology, optical and optoelectronic properties of the nanowires were studied

by a series of experimental techniques, and correlated to the THz responses measured by THz-TDS. GaAs/AlGaAs single nanowire photoconductive THz detectors were successfully demonstrated, and shown to operate well over a usable detection range (0.1-0.6 THz) that may in future be adjusted through proper device geometry. The demonstration of single GaAs/AlGaAs nanowire detectors with a specific frequencies response through antenna design, could lead to numerous potential applications for tunable band THz devices, for example, amplitude modulator/switches and tunable narrowband THz emitters/detectors. The following chapter will focus on the modelling of detector design to explore single nanowire THz detectors for broadband THz-TDS spectroscopy applications.

References

[1] P. Parkinson, H. J. Joyce, Q. Gao, H. H. Tan, X. Zhang, J. Zou, C. Jagadish, L. M. Herz, and M. B. Johnston, "Carrier lifetime and mobility enhancement in nearly defect-free core-shell nanowires measured using time-resolved terahertz spectroscopy," *Nano Letters*, vol. 9, pp. 3349-3353, 2009.

[2] H. J. Joyce, C. J. Docherty, Q. Gao, H. H. Tan, C. Jagadish, J. Lloyd-Hughes, L. M. Herz, and M. B. Johnston, "Electronic properties of GaAs, InAs and InP nanowires studied by terahertz spectroscopy," *Nanotechnology*, vol. 24, pp. 214006-214012, 2013.

[3] J. Lloyd-Hughes, L. Fu, E. Castro-Camus, S. Merchant, H. H. Tan, C. Jagadish, and M. B. Johnston, "THz emitters and detectors based on ion implanted III-V semiconductors," *Conference Digest of the 2006 Joint 31st International Conference on Infrared and Millimeter Waves and 14th International Conference on Terahertz Electronics*, pp. 149-149, 2006.

[4] E. Castro-Camus, L. Fu, J. Lloyd-Hughes, H. H. Tan, C. Jagadish, and M. B. Johnston, "Photoconductive response correction for detectors of terahertz radiation," *Journal of Applied Physics*, vol. 104, p. 053113, 2008.

[5] H. J. Joyce, Q. Gao, H. H. Tan, C. Jagadish, Y. Kim, X. Zhang, Y. N. Guo, and J. Zou, "Twin-free uniform epitaxial GaAs nanowires grown by a two-temperature process,"

Nano Letters, vol. 7, pp. 921-926, 2007.

[6] N. Jiang, Q. Gao, P. Parkinson, J. Wong-Leung, S. Mokkapati, S. Breuer, H. H. Tan, C. L. Zheng, J. Etheridge, and C. Jagadish, "Enhanced minority carrier lifetimes in GaAs/AlGaAs core–Shell nanowires through shell growth optimization," *Nano Letters,* vol. 13, pp. 5135-5140, 2013.

[7] P. Parkinson, J. Lloyd-Hughes, Q. Gao, H. H. Tan, C. Jagadish, M. B. Johnston, and L. M. Herz, "Transient terahertz conductivity of GaAs nanowires," *Nano Letters,* vol. 7, pp. 2162-2165, 2007.

[8] N. Jiang, P. Parkinson, Q. Gao, S. Breuer, H. H. Tan, J. Wong-Leung, and C. Jagadish, "Long minority carrier lifetime in Au-catalyzed GaAs/AlxGa$_{1-x}$As core-shell nanowires," *Applied Physics Letters,* vol. 101, pp. 023111-023114, 2012.

[9] H. J. Joyce, Q. Gao, H. H. Tan, C. Jagadish, Y. Kim, M. A. Fickenscher, S. Perera, T. B. Hoang, L. M. Smith, H. E. Jackson, J. M. Yarrison-Rice, X. Zhang, and J. Zou, "Unexpected benefits of rapid growth rate for III-V nanowires," *Nano Letters,* vol. 9, pp. 695-701, 2009.

[10] P. Parkinson, N. Jiang, Q. Gao, H. H. Tan, and C. Jagadish, "Direct-write non-linear photolithography for semiconductor nanowire characterization," *Nanotechnology,* vol. 23, pp. 335704-335708, 2012.

[11] K. Peng, P. Parkinson, L. Fu, Q. Gao, N. Jiang, Y. N. Guo, F. Wang, H. J. Joyce, J. L. Boland, H. H. Tan, C. Jagadish, and M. B. Johnston, "Single nanowire photoconductive terahertz detectors," *Nano Letters,* vol. 15, pp. 206-210, 2015.

[12] J. L. Boland, S. Conesa-Boj, P. Parkinson, G. Tütüncüoglu, F. Matteini, D. Rüffer, A. Casadei, F. Amaduzzi, F. Jabeen, C. L. Davies, H. J. Joyce, L. M. Herz, A. Fontcuberta i Morral, and M. B. Johnston, "Modulation doping of GaAs/AlGaAs core–shell nanowires with effective defect passivation and high electron mobility," *Nano Letters,* vol. 15, pp. 1336-1342, 2015.

[13] H. J. Joyce, P. Parkinson, N. Jiang, C. J. Docherty, Q. Gao, H. H. Tan, C. Jagadish, L. M. Herz, and M. B. Johnston, "Electron mobilities approaching bulk limits in 'surface-free' GaAs nanowires," *Nano Letters,* vol. 14, pp. 5989-5994, 2014.

[14] H. J. Joyce, J. Wong-Leung, C.-K. Yong, C. J. Docherty, S. Paiman, Q. Gao, H. H. Tan,

C. Jagadish, J. Lloyd-Hughes and L. M. Herz, "Ultralow surface recombination velocity in InP nanowires probed by terahertz spectroscopy," *Nano letters*, vol. 12, pp. 5325-5330, 2012.

[15] C. Wood, J. Cunningham, I. Hunter, P. Tosch, E. Linfield, and A. Davies, "On-chip pulsed terahertz systems and their applications," *International journal of infrared and millimeter waves*, vol. 27, pp. 557-569, 2006.

[16] J. Cunningham, M. Byrne, C. Wood, and L. Dazhang, "On-chip terahertz systems for spectroscopy and imaging," *Electronics Letters*, vol. 46, pp. s34-s37, 2010.

Chapter 5

Optimisation of Antenna Design for Broadband GaAs/AlGaAs Nanowire Terahertz Detectors

5.1 Introduction

Broad terahertz (THz) detection bandwidth is important for many applications, particularly essential to spectroscopic application such as THz time-domain spectroscopy (THz-TDS) [1, 2]. It has been shown in Chapter 4 that the bandwidth of detector response is a strong function of the resonant characteristics of the device geometry. In order to obtain some guidance for future work and understand how the device design can be used to tailor the response performance and bandwidth of the detector, various detector geometries, including two-pad (as described in Chapter 4), bow-tie [3] and strip-line structure [4], were modelled using finite-difference time-domain (FDTD) simulations [5] in this chapter. Based on the optical simulation results, geometry-optimised GaAs/AlGaAs single nanowire photoconductive THz detectors were designed and fabricated with a broadened detection bandwidth achieved in the range of 0.1-1.6 THz, highlighting the importance of a careful device design for photoconductive THz detection.

Furthermore, in this chapter the low-noise nature of single nanowire photoconductive THz detector (benefiting from its nanoscale size of detecting material on an insulating substrate) is discussed, revealing the fundamental advantage of the relaxed requirement of an extremely short carrier lifetime within the semiconductor material for photoconductive THz detection, and suggesting that more III-V nanowire systems may be considered for THz detection (as will be described in Chapter 6). The additional effects of the thin GaAs capping on the response characteristics of the GaAs/AlGaAs core-shell single nanowire THz detectors is also analysed and discussed.

5.2 Finite-Difference Time-Domain Simulation for Terahertz Detector Antenna Design

5.2.1 Simulation Setup

In order to make sure the simulation environment matches the experimental conditions, a broadband pulsed 'Gaussian Source' was used as the simulation THz source with characteristics such as pulse profile and bandwidth imported from experimental data measured using a standard electro-optic detection crystal (ZnTe) [6] as shown in Figures 4.7(b) and (e). Although experimentally the thickness of the gold electrodes was 300 nm, a thickness of 4 μm was chosen as the simulated electrode thickness to avoid the use of a mesh size which was too-small in the z-direction. Considering the shortest wavelength in the simulation was around 60 μm, it was reasonable to make such approximation (since the 4 μm was much smaller than the shortest wavelength). A mesh override region was added to the gold layer to force a 2 μm mesh (dx=dy=dz=2 μm). A time (point) monitor, was placed at the centre of the device configuration to receive the arrived THz radiation in time domain. In most cases, simulations were performed at normal incidence, and the polarisation of the incident THz electric field was parallel to the nanowire axis as used experimentally. Due to the large and negative real part of the relative permittivity of most metals at THz frequencies, the perfect electrical conductor (PEC) material model was employed for all simulations. Details of the simulation software regarding FDTD solution can be found in Section 3.5.2.

5.2.2 Simulated Device Geometry

The simulated device geometries are categorised into two groups as shown in Figures 5.1 and 5.2, respectively. Figure 5.1 consists of seven detector configurations, including the basic two-pad detector geometry as described in Chapter 4 and the other six variations derived from it. These seven geometries were simulated to understand the reason for the narrow detection bandwidth and origin of specific frequency resonant peaks for the two-pad nanowire THz detector. It is of particular interest to know which part of the two-pad structure determines the

resonant frequency range of the detector. Table 5.1 shows the dimensions of the seven two-pad related device geometries.

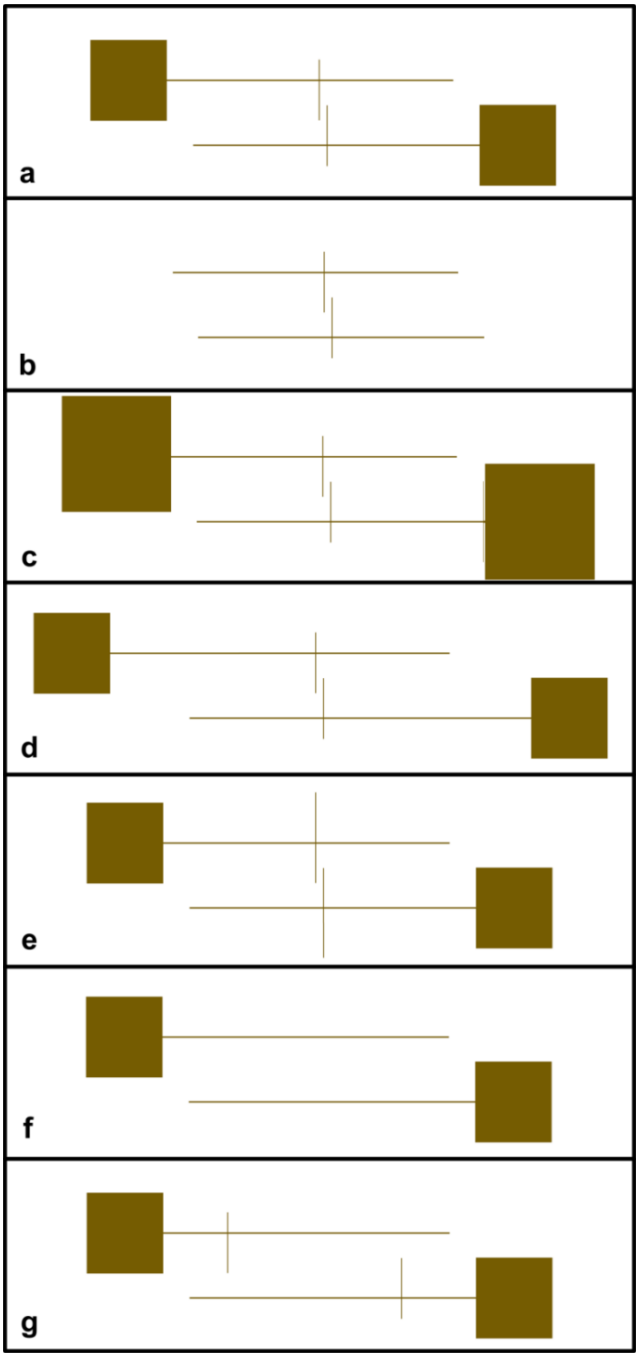

Figure 5.1: Detector geometries used for FDTD simulations: (a) the reference two-pad antenna (as described in Chapter 4); (b) two-pad antenna with no pads; (c) two-pad antenna with larger pads; (d) two-pad antenna with pads further apart; (e) two-pad antenna with longer centre lines; (f) two-pad antenna without centre lines; (g) two-pad antenna with centre lines further apart.

Table 5.1: Detailed two-pad detector geometry and its six derivatives used in FDTD simulations.

Geometry Description	**Two Pads**		**Centre Thin Lines**	
Name	**Pad Area (μm^2)**	**Distance Between Two Pads (μm)**	**Length (μm)**	**Distance Between (μm)**
Two-pad (a)	200×200	820	150	17.5
No-pad (b)	0×0	820	150	17.5
Larger-pad (c)	400×400	820	150	17.5
Pads-apart (d)	200×200	1020	150	17.5
Longer-centre lines (e)	200×200	820	240	17.5
No-centre lines (f)	200×200	820	0	0
Centre lines-apart (g)	200×200	820	150	417.5

In addition, since the bow-tie [7] and strip-line [8] antenna have been proven to provide a broadband THz response in bulk detectors [7], it is useful to further study their use in single nanowire detectors and investigate their influence on the frequency response of the single nanowire detectors. In this chapter, both bow-tie and strip-line detector geometry were also simulated and compared with the two-pad detector, as shown in Figure 5.2.

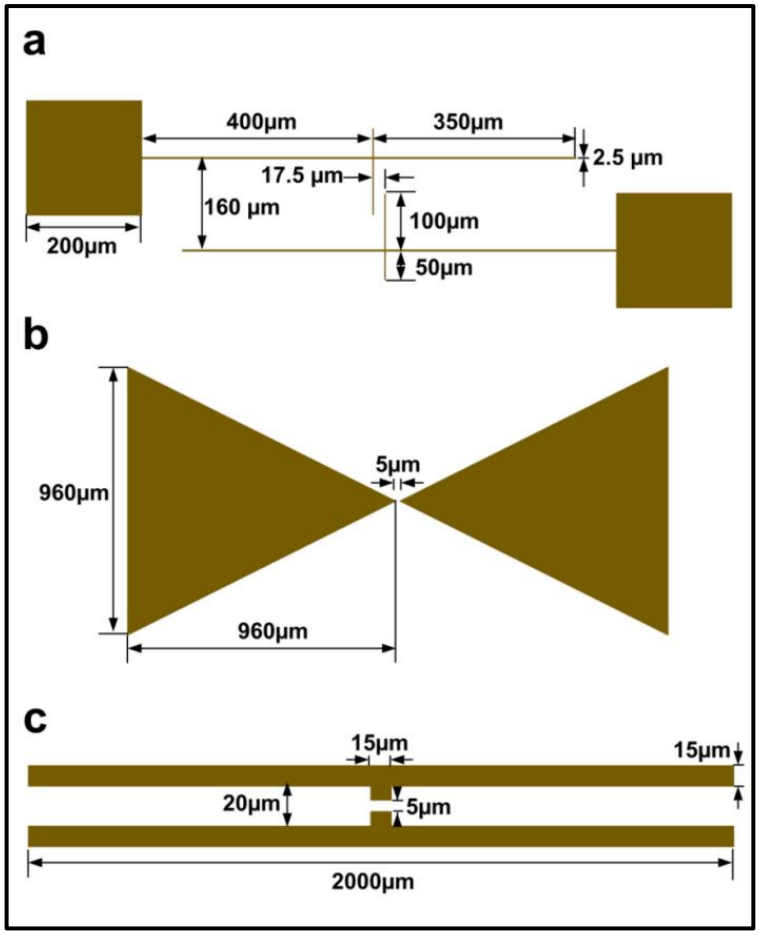

Figure 5.2: Detailed detector geometries used for both experiments and FDTD simulations: (a) two-pad antenna; (b) bow-tie antenna; (c) strip-line antenna.

5.2.3 Resonant Characteristics of Different Antenna Structures

For the two-pad configuration, the two large square pads (200 μm × 200 μm) were assumed to be responsible for the reduced bandwidth of the detector as their sizes are comparable to the incident THz wavelength (~ 300 μm). To examine this, modifications were made to the original two-pad geometry (Figure 5.1(a)) as used experimentally for simulation study, including removing the square pads (Figure 5.1(b)), increasing the area of the square pads (Figure 5.1(c)) and increasing the distance between the two square pads (Figure 5.1(d)). Figure 5.3 shows THz responses obtained by FDTD simulations from the four two-pad device geometries defined in Figures 5.1(a)-(d). The simulation results clearly reveal that the square pads in fact do not affect the overall spectral response profile of the THz detector; however

their size may affect the resonant peak positions of the response spectrum. In order to figure out which part determines the resonant frequency in the two-pad geometry, more modifications are made to the original two-pad configuration by adjusting other design parameters as shown in Figures 5.1(e)-(g).

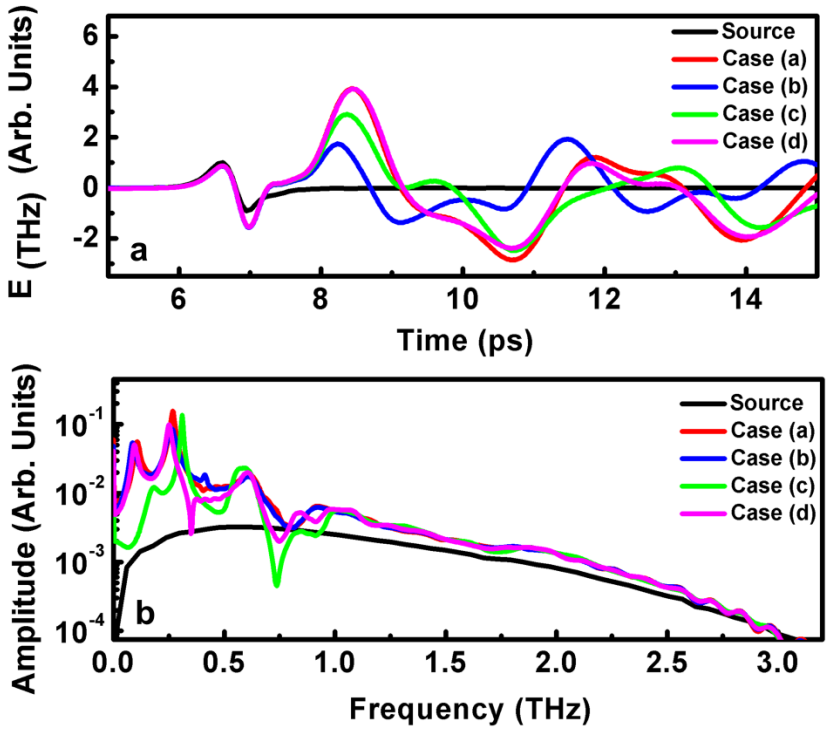

Figure 5.3: (a) Time-domain THz electric field transient obtained from simulated antenna geometries as described in Figures 5.1(a-d). (b) Frequency spectrum of THz electric field transformed from (a).

Figure 5.4 shows THz responses obtained from the two-pad geometries in Figures 5.1(a) and (e)-(g) obtained by FDTD simulations. It can be seen that, the (two) thin strip lines at the centre of the two-pad geometry play a crucial role in control of the response amplitude and resonant frequency of the detector. The length of the thin strip lines (Figure 5.1(e)) affects the positions of resonant frequency peaks, where a longer length leads to a stronger resonance at lower frequency region in response of the detector. The gap between the two thin strip lines (Figure 5.1(g)) determines the response spectral profile and amplitude of the detector, where a larger gap results in a flat and broad spectral response however a lower response amplitude. Since the thin strip lines are used for contacting the single nanowire in this work, between

which the distance are limited by the length of the single nanowires, the two-pad geometry is not suitable to be used as the antenna structure for single nanowire detectors for broad flat band THz detection with high amplitude.

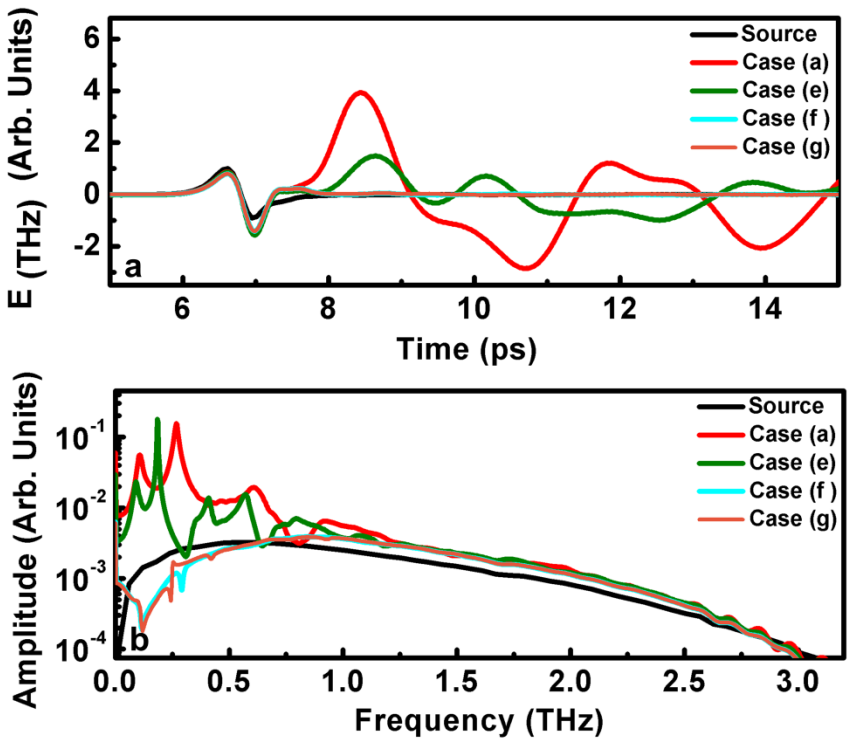

Figure 5.4: (a) Time-domain THz electric field transient obtained from simulated antenna geometries as described in Figures 5.1(a) and (e-d). (b) Frequency spectrum of THz electric field transformed from (a).

Figure 5.5 shows the THz responses obtained from the other device geometries studied by FDTD simulations. The two-pad configuration as shown in Figure 5.5(a) is the reference geometry used to fabricate initial single nanowire detectors as described in Chapter 4. Bow-tie and strip-line configurations shown in Figure 5.5(b) and (c) have been widely used for broadband THz detection in bulk detectors [7, 8], which were designed and simulated in this work. Figures 5.5(d) and (e) indicate that the two-pad electrode design would strengthen the incident THz electric field signal but cause a distortion in the measured waveform resulting in strong low-frequency resonances. The bow-tie electrode on the other hand would not only strengthen the incident THz signal by a larger factor, but also with a minor distortion in measured waveform as a result of relatively broadband response. The strip-line structure may

be the best choice of geometry for THz detection strengthening the incident THz signal while minimising distortion of radiation waveform, however, it does not strengthen the THz field to the same extent observed for the bow-tie or two-pad geometry (see Figure 5.5(d)).

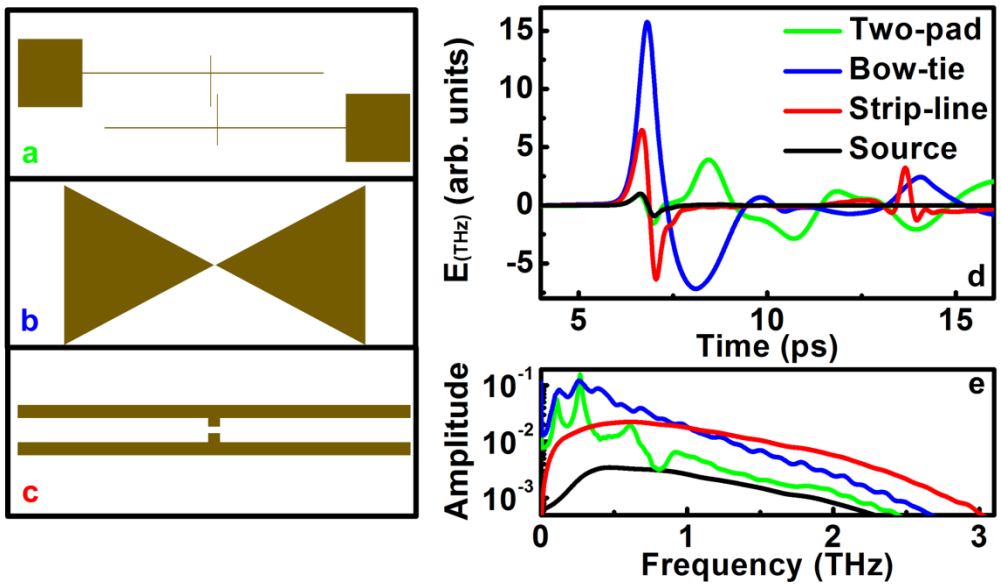

Figure 5.5: Schematic representations of device geometry studied by FDTD simulations: (a) Two-pad; (b) Bow-tie; (c) Strip-line. (d) Time-domain THz electric field transient obtained from simulations with different antenna geometries. (e) Frequency spectrum of THz electric field transient from (d).

5.3 GaAs/AlGaAs Nanowire Terahertz Detectors with Optimised Antenna Design for Broadband Response

5.3.1 Detector Fabrication

To verify the simulation results while obtaining the best performing broadband single nanowire THz detectors, geometry-optimised GaAs/AlGaAs single nanowire THz detectors were designed, fabricated and characterised. The best performing GaAs/AlGaAs nanowires - sample A (as described in Chapter 4) were transferred onto z-cut quartz substrates. Conventional ultraviolet (UV) photolithography [9] was employed to pattern the electrodes onto the nanowires. Both bow-tie and strip-line antenna designs (as studied in FDTD

simulations) were chosen as the electrode geometries for new nanowire detectors. An oxygen plasma etch was used for further removal of the photoresist residue on nanowires, followed by a 4% HCl chemical etching to remove native oxide layer formed on the nanowire surface. The detector structures were finally metallised using electron beam evaporation, followed by a lift-off process to form Ti/Au (10 nm/300 nm) contacts. It is worth mentioning that, due to the challenges to locate a single nanowire for electrode patterning via UV lithography, longer GaAs/AlGaAs nanowire (sample A) with an average length of 30-35 μm were grown and used for detector fabrication this time.

The geometries for both bow-tie and strip-line GaAs/AlGaAs single nanowire THz detectors are shown in Figure 5.6. The gap between two contact electrodes for all configurations was designed to be 5 μm on the photomask in UV photolithography. However, due to the relatively low resolution (~ 2 μm) of UV photolithography, it is difficult to achieve very sharp features as originally designed by the simulation and photomask, as shown in Figure 5.6. The measured gap distance was ~ 5 μm for strip-line detectors, and ~ 8 μm for bow-tie detectors.

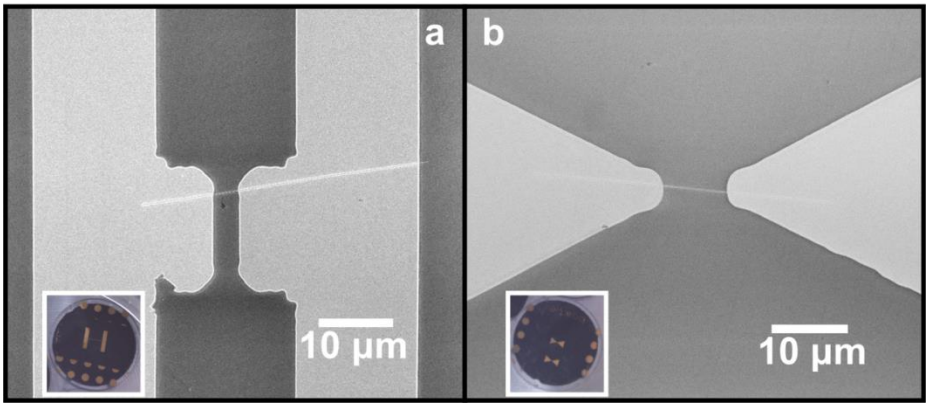

Figure 5.6: SEM images of the central area of the fabricated GaAs/AlGaAs single nanowire detectors with (a) a strip-line device geometry and (b) a bow-tie device geometry. Inset: zoom-out optical images of the fabricated devices on quartz substrates.

5.3.2 Terahertz Detector Performance

The single nanowire detectors were characterised using the THz-TDS system [2,10,11]

described in Section 3.4. GaAs/AlGaAs single nanowire detectors with both bow-tie and strip-line geometries were successfully measured. For each type of the device geometry, the detectors show a high similarity in their response profiles. The detection bandwidth of the newly fabricated nanowire detectors are significantly improved (in the range of 0.1-1.6 THz, shown in Figure 5.7) when compared to those described in Chapter 4, which can be directly attributed to the optimisation of detector geometry. It is also noted that the response currents obtained from the bow-tie nanowire detectors is approximately 2.5 times higher than that obtained from the strip-line nanowire detector, which agrees well with the simulation results, where the bow-tie geometry is more effective in strengthening the incident THz electric field than the strip-line geometry. Due to the limited detection material volume and thus very low THz response current (a few pA), the GaAs/AlGaAs single nanowire detectors failed to measure the full spectral range of the incident THz source (0.1-3.0 THz). By further improving the detection material for higher response current and lower noise floor in the detector, broader detection bandwidth could be achieved (as will be discussed in Chapter 6).

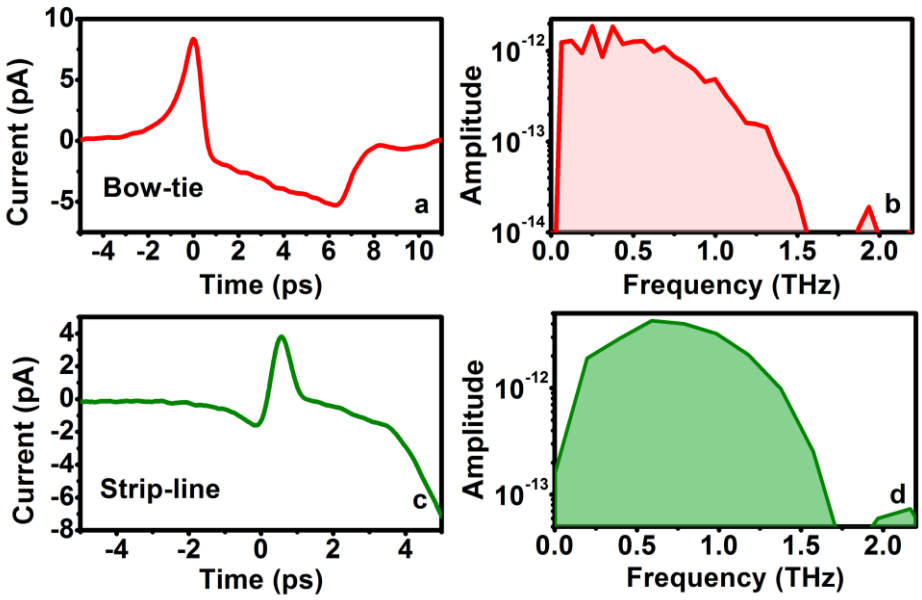

Figure 5.7: THz-TDS characterisation of the bow-tie (red) and strip-line (green) GaAs/AlGaAs single nanowire THz detectors. Left: unprocessed time-domain THz-induced current. Right: processed THz amplitude spectrum.

To further benchmark the broadband single nanowire detectors, traditional InP receivers (Fe^{+}-implanted InP [12]) based on the same device geometry designs (bow-tie and strip-line) were fabricated and characterised in the same THz-TDS system as references for comparison. Table 5.2 shows a comparative device performance analysis between the GaAs/AlGaAs single nanowire THz detectors and traditional bulk THz receivers. Despite having only pA-level responses, the single nanowire detectors show comparable signal-to-noise ratio (SNR) to the bulk ones. Considering the large difference in detection material volume, the single nanowire detectors perform very competitively.

Table 5.2: A comparison of device performance between single GaAs/AlGaAs nanowire detector and traditional ion-implanted InP photoconductive receiver.

Device type / **Performance**	**Single GaAs/AlGaAs Nanowire**		**Ion-implanted InP**	
	Strip-line	**Bow-tie**	**Strip-line**	**Bow-tie**
Conductivity Lifetime	~ 4600 ps		< 6 ps	
Dark Current (at 1 V bias)	~10 pA	~10 pA	~ 69200 pA	~ 45700 pA
THz Signal	7.96 pA	13.6 pA	676.6 pA	544.3 pA
Signal-to-Noise Ratio	34	31	70	43

To understand the low-noise nature of the single nanowire detector, different noise sources for photoconductive detectors were analysed. For traditional (bulk) photoconductive receivers, the sources of the noise in response current predominantly arise from the electrical noise, namely Johnson-Nyquist and shot noise [13], as well as external noise [14] such as intensity fluctuations in the laser pulse or THz pulse. In contrast, single nanowire detectors, taking the advantage of the nanoscale active material volume and the use of insulating substrates, have a very low dark current (see Table 5.2), leading to very low Johnson-Nyquist noise. Therefore, for single nanowire THz detectors, the main sources of noise in response current are from the shot noise and external noises. The significantly reduced noises in the single nanowire detectors improved their signal-to-noise performance. This explains why the GaAs/AlGaAs

single nanowire detectors show lower noise compared with bulk ion-implanted InP receivers, despite the former having a much longer carrier lifetime (see Table 5.2).

5.3.3 Influence of GaAs Capping on Detector Response

For the THz-TDS measurement, an 800 nm (1.55 eV) laser was used to photo-excite the nanowire detectors. Since the Al composition in the AlGaAs shell is nominally around 42%, requiring higher energy (> 1.94 eV) to excite, it is reasonable to assume that most of the THz-induced current is generated in the GaAs core region only. However, as has been noted from Figure 4.5 that despite being very thin (and hence possessing small material volume), the outer GaAs cap layer causes a small but non-negligible signal at the short early time when measuring nanowire photoconductivity lifetimes (very fast decay, < 10 ps). Thus the GaAs cap layer could also play a non-negligible role in the THz-TDS measurement. In this section, the effect of cap layer on THz response characteristics of the GaAs/AlGaAs single nanowire detectors is further investigated.

As detailed in Section 2.4.2, in general, there are two basic types of photoconductive detectors (as determined by the photoconductivity lifetime of the detection material), which require two different signal processing techniques to recover the measured THz field including direct sampling and integrating sampling. Figure 5.8 shows the FDTD simulation results which have been processed taking into account the two different sampling modes. In Figure 5.8, the THz responses obtained from the simulated bow-tie antenna operating under direct and integrating sampling mode are plotted respectively, in comparison with that from an experimentally measured bow-tie GaAs/AlGaAs single nanowire detector. It can be seen clearly that the response profile of the single nanowire detector does not resemble either of the simulated responses, but more like a combination of the simulated results, implicating that direct and integrating samplings may occur simultaneously in the GaAs/AlGaAs nanowire detector. The passivated GaAs core, owing to having a long photoconductivity lifetime (~ 4 ns, see Figure 4.5), is no doubt an integrating detector; whereas the highly defective GaAs capping layer could be responsible for the direct sampling behaviour observed in the detector due to its ultra-short photoconductivity lifetime (< 10 ps). In occasional cases, some GaAs/AlGaAs

single nanowire detectors were found to operate under directing sampling mode only (as shown in Figure 5.9), indicating that the GaAs capping layers can sometimes dominate the whole detector performance. To eliminate the capping influence and reduce the response complexity, etching of the cap layers at the contact region to make the electrical contacts directly to the core area for the core-shell-cap nanowires may be helpful to avoid the complication for data analysis and improve the reproducibility of the device performance.

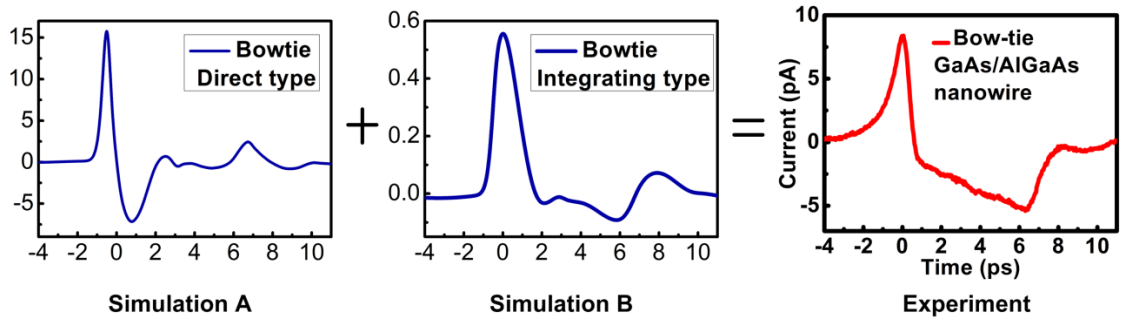

Figure 5.8: Time-domain THz responses in a THz-TDS system as obtained from a simulated bow-tie antenna (blue) and a typical bow-tie GaAs/AlGaAs single nanowire detector (red). Simulation A represents a direct sampling detector and simulation B represents an integrating sampling detector.

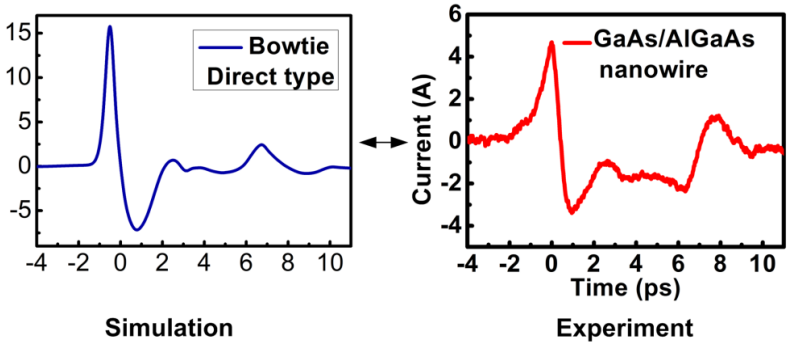

Figure 5.9: Time-domain THz responses in a THz-TDS system as obtained from a simulated bow-tie antenna (blue) in the direct sampling mode and an untypical bow-tie GaAs/AlGaAs single nanowire detector (red).

5.5 Summary

FDTD simulations in the THz frequency regime were carried out to investigate the relationship between the geometry design of the photoconductive detector and its effect on the characteristics of THz responses. Based on the FDTD simulation, GaAs/AlGaAs single nanowire THz detectors with broad detection bandwidth (0.1-1.6 THz) were achieved by using two new device geometries, including bow-tie and strip-line configurations. A notable low-noise nature of the single nanowire detector has been observed and ascribed to its small active material volume and the use of insulating substrates. As such, the GaAs/AlGaAs nanowires no longer require an extremely short carrier lifetime (typically a few picoseconds) to minimise the noise current as is commonly required in bulk semiconductors. Two sampling modes (direct and integrating sampling) were found in the operation of the GaAs/AlGaAs single nanowire detector, which can be attributed to the contributions from GaAs cap and the GaAs core, respectively, leading to complexity in THz response for analysis and processing. Based on these findings, single nanowire photoconductive THz detectors developed from the other nanowire materials for higher sensitivity and simpler sampling mode in device operation are proposed in Chapter 6, to achieve improved performance of THz detection.

References

[1] K.-E. Peiponen, A. Zeitler, and M. Kuwata-Gonokami, *Terahertz Spectroscopy and Imaging*, vol. 171: Springer, 2012.

[2] W. Withayachumnankul and M. Naftaly, "Fundamentals of measurement in terahertz time-domain spectroscopy," *Journal of Infrared, Millimeter, and Terahertz Waves*, vol. 35, pp. 610-637, 2014.

[3] D. M. Hailu, I. A. Ehtezazi, M. Neshat, and S. Safavi-Naeini, "Simulation of bow-tie THz antenna using hybrid finite element method and spectral ray tracing technique," in *2009 34th International Conference on Infrared, Millimeter, and Terahertz Waves*, pp. 1-2, 2009.

[4] T. K. Nguyen and I. Park, "Effects of antenna design parameters on the characteristics

of a terahertz coplanar stripline dipole antenna," *Progress In Electromagnetics Research M*, vol. 28, pp. 129-143, 2013.

[5] H.-T. Chen, W. J. Padilla, J. M. Zide, A. C. Gossard, A. J. Taylor, and R. D. Averitt, "Active terahertz metamaterial devices," *Nature*, vol. 444, pp. 597-600, 2006.

[6] D. N. Erschens, D. Turchinovich, and P. U. Jepsen, "Optimized optical rectification and electro-optic sampling in ZnTe Crystals with chirped femtosecond laser pulses," *Journal of Infrared, Millimeter, and Terahertz Waves*, vol. 32, pp. 1371-1381, 2011.

[7] Y. P. Yang, R. Singh, and W. L. Zhang, "Anomalous terahertz transmission in bow-tie plasmonic antenna apertures," *Optics Letters*, vol. 36, pp. 2901-2903, 2011.

[8] S. Kasai, A. Tanabashi, K. Kajiki, T. Itsuji, R. Kurosaka, H. Yoneyama, M. Yamashita, H. Ito, and T. Ouchi, "Micro strip line-based on-chip terahertz integrated devices for high sensitivity biosensors," *Applied Physics Express*, vol. 2, 062401, 2009.

[9] F. Cerrina, "Lithography," in *Wiley Encyclopedia of Electrical and Electronics Engineering*, ed: John Wiley & Sons, Inc., 2001.

[10] K. Peng, P. Parkinson, J. L. Boland, Q. Gao, Y. C. Wenas, C. L. Davies, Z. Li, L. Fu, M. B. Johnston, H. H. Tan, and C. Jagadish, "Broadband phase-sensitive single InP nanowire photoconductive terahertz detectors," *Nano Letters*, vol. 16, pp. 4925-4931, 2016.

[11] D. Saeedkia, *Handbook of Terahertz Technology for Imaging, Sensing and Communications*: Elsevier, 2013.

[12] K. Peng, P. Parkinson, L. Fu, Q. Gao, N. Jiang, Y. N. Guo, F. Wang, H. J. Joyce, J. L. Boland, H. H. Tan, C. Jagadish, and M. B. Johnston, "Single nanowire photoconductive terahertz detectors," *Nano Letters*, vol. 15, pp. 206-210, 2015.

[13] E. Castro-Camus, J. Lloyd-Hughes, L. Fu, H. H. Tan, C. Jagadish, and M. B. Johnston, "An ion-implanted InP receiver for polarization resolved terahertz spectroscopy," *Optics Express*, vol. 15, pp. 7047-7057, 2007.

[14] M. Li, F. G. Sun, G. A. Wagoner, M. Alexander, and X. C. Zhang, "Measurement and analysis of terahertz tadiation from bulk semiconductors," *Applied Physics Letters*, vol. 67, pp. 25-27, 1995.

Chapter 6

Highly Sensitive Broadband Photoconductive Terahertz Detectors Based on InP Nanowires

6.1 Introduction

From previous chapters, it is concluded that proper device design and optimised material optoelectronic properties are key factors for development of high-performance single nanowire photoconductive terahertz (THz) detectors. It is also discovered that due to the low-noise nature single nanowire THz detectors may allow more choices of the detection materials, opening new opportunities to explore a wide range of nanowire systems for THz applications. In this chapter, high-quality InP nanowires grown by selective-area metalorganic vapour phase epitaxy (SA-MOVPE) were investigated for their applications as high-performance THz detectors in THz-TDS systems.

InP based material systems are favoured over GaAs system in a number of optoelectronic device applications [1], owing to their low surface recombination velocity [2, 3] and concurrent high carrier mobility. InP nanowires maintain the property of a low surface recombination velocity and high carrier mobility, and are therefore a great promise for photoconductive THz detection. InP nanowires have also shown high photo-sensitivity [4-6] and radiative quantum efficiency [4] when compared with other III-V nanowires, due to the suppressed non-radiative recombination (originated from the intrinsically low surface recombination velocity). This eliminates the need for additional chemical or surface passivation to enhance radiative recombination and prevent oxidative degradation [6, 7], which are otherwise essential for (In,Al,Ga)As material system. In this chapter, (core-only) InP single nanowire photoconductive THz detectors were fabricated and studied. These THz detectors were developed from structurally-uniform stacking fault-free InP nanowires grown by

SA-MOVPE technique. Combined with optimised device geometries (as described in Chapter 5), the InP single nanowire THz detectors can provide high-quality time-domain spectra (including both amplitude and phase information) for materials characterisation in a THz time-domain spectroscopy (THz-TDS) system, comparable to those bulk THz detector (including the ion-implanted bulk InP receiver and the standard electro-optic ZnTe crystal THz detector).

6.2 Growth and Characterisation of InP Nanowires

6.2.1 Growth Details

InP nanowires were grown using SA-MOVPE [4]. A 30 nm SiO_2 mask layer was first deposited on (111)A InP substrates, and patterned by electron beam lithography (EBL) to create hexagonal arrays of circles. The pattern was then transferred to the SiO_2 mask by wet chemical etching using buffered hydrogen fluoride solution. After etching, the diameter of the circles was 200 nm with a pitch of 800 nm. The patterned substrates were then loaded into a horizontal flow low pressure (100 mbar) MOVPE system. All samples were annealed at 750 °C for 10 min under a phosphine protective flow and grown at 730 °C for 40 min with trimethylindium (TMIn) and phosphine at a flow rate of 6.1×10^{-6} and 4.9×10^{-4} mol/min, respectively.

6.2.2 Material Characterisation

6.2.2.1 Scanning/Transmission Electron Microscopy

The detailed nanowire growth and characterisation based on the identical growth conditions (except for the growth time) have been previously reported elsewhere [4, 8], and shown to produce pure wurtzite (WZ) phase, structurally-uniform and high-quantum-efficiency InP nanowires with a range of diameters from 220 to 280 nm and lengths from 8 to 11um. Figure 6.1 shows the scanning electron microscope (SEM) images of the InP nanowires after growth.

The transmission electron microscope (TEM) images (see Figure 6.2) for these InP nanowire show that the nanowires grown under this condition are almost defect free; there are no zinc blende (ZB) stacking faults formation along the nanowires.

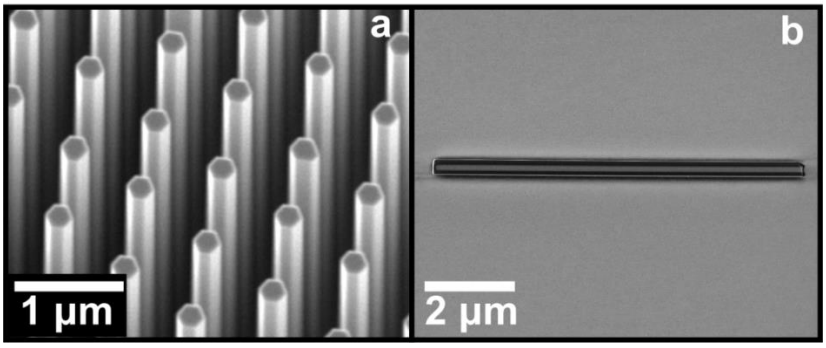

Figure 6.1: SEM images of the InP nanowires used in this study: (a) an array of nanowires; (b) a single nanowire transferred onto a quartz substrate.

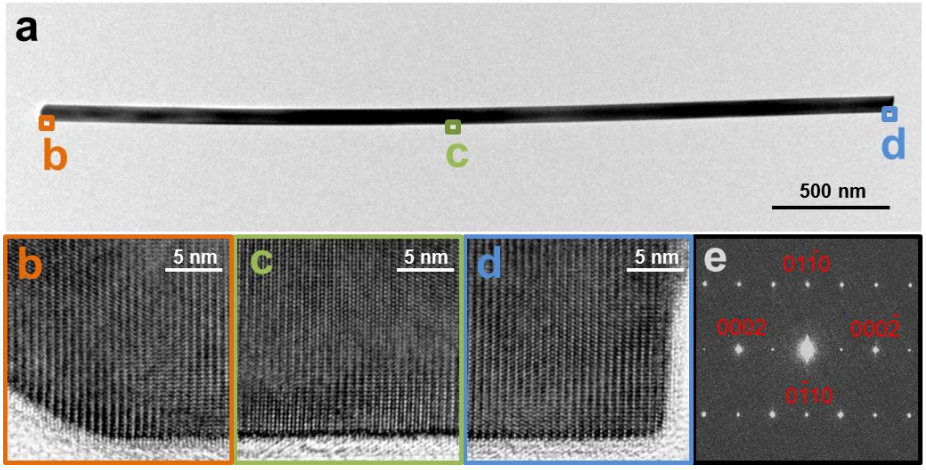

Figure 6.2: (a) Bright-field TEM image showing the morphology of a typical InP nanowire grown under similar condition to those used in this thesis. (b–d) TEM images taken along [-2110] zone axis from the top, middle, and bottom regions of the single InP nanowire shown in (a), respectively. The TEM images show that the nanowire has a WZ structure and are free of stacking faults. (e) Selected area electron diffraction pattern of the nanowire shown in (d) confirming the WZ phase. (Adapted from reference [4])

6.2.2.2 Photoluminescence and Time-Resolved Photoluminescence

Photoluminescence (PL) measurements were performed at room temperature to characterise the optical properties of these InP nanowires. The typical PL spectrum for a single InP nanowire is presented in Figure 6.3, with a peak centred at 1.413 eV and a shoulder at higher energy of 1.44 eV. The lower energy peak is attributed to band edge emission from WZ InP nanowires [9, 10] and the higher energy peak to the split off valence band [11, 12]. The strong PL emission indicates the high crystal quality achieved by using SA-MOVPE technique [4]. PL intensity decay behaviour for these InP nanowires was also investigated by the time-resolved PL (TRPL) measurements at room temperature. The inset figure in Figure 6.3 shows the decay time (PL lifetime) measured at the PL peak energy of 1.413 eV, which is ~ 1.54 ns.

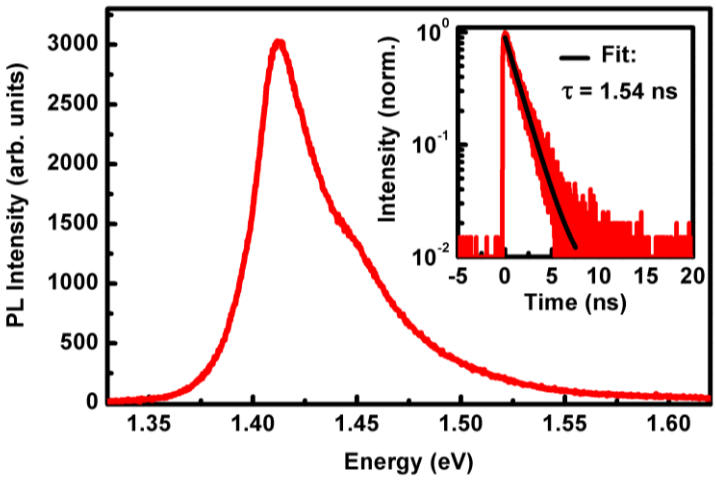

Figure 6.3: A typical room-temperature PL spectrum of a single InP nanowire studied in this thesis. The insert figure shows the TRPL decay of the nanowire.

6.3 Detector Fabrication and Characterisation

6.3.1 Device Fabrication

After growth, the InP nanowires were mechanically transferred from the growth substrate to the surface of z-cut quartz substrates, in which a filter paper (held by tweezers) was used to

break off the nanowires from the as-grown substrate and place them onto the quartz substrate (by sweeping the filter paper). Conventional ultraviolet (UV) photolithography was employed to pattern the electrodes onto the nanowires. An oxygen plasma etch was used for further removal of the photoresist residue from nanowires, followed by a 9.3% HCl chemical etching to remove native oxide layer from the nanowire surface. The detector structures were finally achieved by using electron beam evaporation to deposit Ti/Au (10 nm/300 nm) on the electrode patterns followed by lift off.

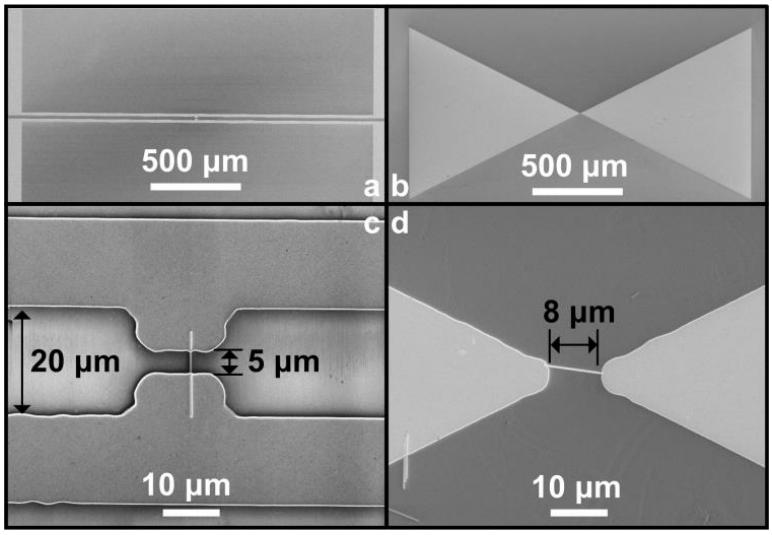

Figure 6.4: SEM images of representative InP single-nanowire detectors used in this study, labelled with nominal dimensions: (a), (c) a nanowire detector with strip-line geometry; (b), (d) a nanowire detector with bow-tie geometry. (Top) Zoom-out views of the fabricated detectors. (Bottom) Zoom-in images of the central area of the detectors.

Both bow-tie and strip-line antennas were fabricated as electrode geometries for the InP nanowire detectors, which have been simulated and proven to provide a broadband THz response in Chapter 5. Figure 6.4 shows typical SEM images of the InP single nanowire detectors used in this chapter.

6.3.2 Dark/Photo Current-Voltage Measurement

The optoelectronic properties of InP single nanowire detectors were characterised by

dark/photo current-voltage (I-V) measurement. Photocurrents from InP single nanowire detectors were obtained under the illumination of a pulsed 522 nm laser at a fluence of 0.8 mJ/cm^2/pulse, which is exactly the same illumination condition used to measure the GaAs/AlGaAs single nanowire detectors (Section 4.3.2). Figure 6.5 shows the I-V curves from a GaAs/AlGaA single nanowire detector and an InP single nanowire detector measured under the same illumination conditions. The photocurrents from InP single nanowires were found to be approximately 30 nA at 2 V with the dark currents at sub-nA level (~10^{-11} A), showing much higher photo-sensitivity than those of GaAs/AlGaAs nanowire detectors.

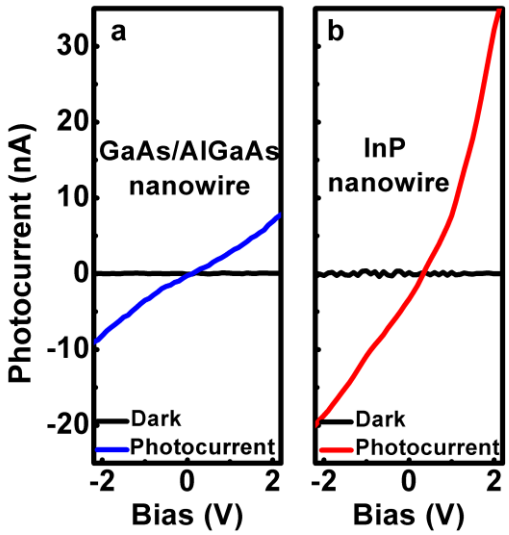

Figure 6.5: Photocurrents measured from (a) a GaAs/AlGaAs single nanowire detector and (b) an InP single nanowire detector fabricated in this study, under illumination of a pulsed laser (522 nm centre wavelength, 300 fs duration and 20 MHz repetition rate) at a fluence of 0.8 mJ/cm^2/pulse.

6.4 Terahertz Measurements

6.4.1 Optical Pump-Terahertz Probe Spectroscopy

The photoconductivity rise time, carrier lifetime and mobility of these InP nanowires were evaluated using time-domain optical pump-THz probe (OPTP) spectroscopy [13, 14] for a comparison with GaAs/AlGaAs nanowires as described in Chapters 4. A mono-exponential

carrier decay was observed for an ensemble of InP nanowires with a sub-picosecond photoconductivity rise time [3] and a photoconductivity lifetime of ~1.71 ± 0.32 ns as shown in Figure 6.6(b). The long (>> 1 ps) photoconductivity life indicates that the InP single nanowire detectors are of integrating type, and they only require one sampling mode in response processing, unlike the GaAs/AlGaAs single nanowire detectors which require considering complicated two-sampling mode processing as a result of multi-exponential decay (where the first sharp decay comes from recombination in the cap layer due to the presence of thin GaAs cap layer outside the GaAs/AlGaAs nanowires) as shown in Figure 6.6(a). The photoconductivity lifetime for these InP nanowires is similar to their PL lifetime (see Section 6.2.2.2), which benefits from their simple core-only structure as opposite to the GaAs/AlGaAs nanowires whose surface GaAs capping and AlGaAs shell cause the complexity of the analysis of material properties and corresponding device performance as discussed in Sections 4.5.1 and 5.3.3. It is also found that the photoconductivity lifetime of these InP nanowires is ~ 2-3 times smaller than that of GaAs/AlGaAs nanowires (sample A in Chapter 4), suggesting a lower noise current level may be observed in InP single nanowire photoconductive detectors. The mobility of InP nanowires was extracted by fitting the photoconductivity spectra [15] and was found to be approximately 1260 ± 320 cm^2 V^{-1} s^{-1} which is a factor of ~ 2 times higher than that of previously reported InP nanowires grown by the vapour-liquid-solid technique [2, 3], further confirming the high quality of the nanowires grown by SA-MOVPE.

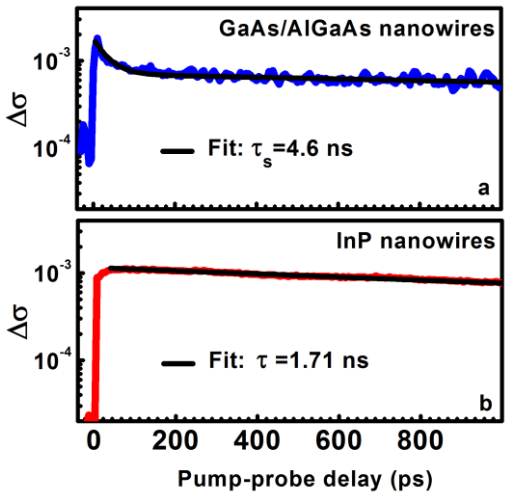

Figure 6.6: A comparison of OPTP photoconductivity decays between (a) GaAs/AlGaAs nanowires (sample A in Chapter 4) and (b) InP nanowires.

6.4.2 Terahertz Detector Performance

The fabricated InP single nanowire detectors were incorporated into a pulsed THz-TDS system [13] for THz response characterisation. The details of the THz-TDS system were described in Section 3.4.4. Figure 6.7 shows the THz responses measured from two strip-line and two bow-tie InP single nanowire detectors, respectively. For each type of nanowire detectors (with the same device configuration), they gave repeatable THz response results in terms of response current profile and the corresponding response spectrum (see Figure 6.7). Similar to the GaAs/AlGaAs nanowire detectors (including both strip-line and bow-tie ones as described in Section 5.3.1), it is found that the THz response current obtained from the bow-tie InP nanowire detectors (Figure 6.7(a)-(f)) is much higher than that obtained from the strip-line InP nanowire detectors (Figure 6.7(g)-(l)), which is consistent with the simulation results (see Figure 5.5). Figure 6.8 shows a demonstration of how to extract both amplitude and phase information from a typical THz-induced transient photocurrent measured from a single InP nanowire detector. Using the temporal current profile directly measured from the nanowire detector as shown in Figure 6.8(a), key information such as the waveform of incident THz electric field as a function of time, and the corresponding phase and amplitude spectrum, were extracted via Fourier transformation and are presented in Figures 6.8(b), (c) and (d) (detailed calculation methods see Chapter 2). It can be seen from Figure 6.8(d) that the THz response measured from the single InP nanowire detector exhibit excellent signal-to-noise ratio (SNR) with broad spectral bandwidth ranging from 0.1 to 2.0 THz which was mainly limited by the bandwidth of the THz source in this work.

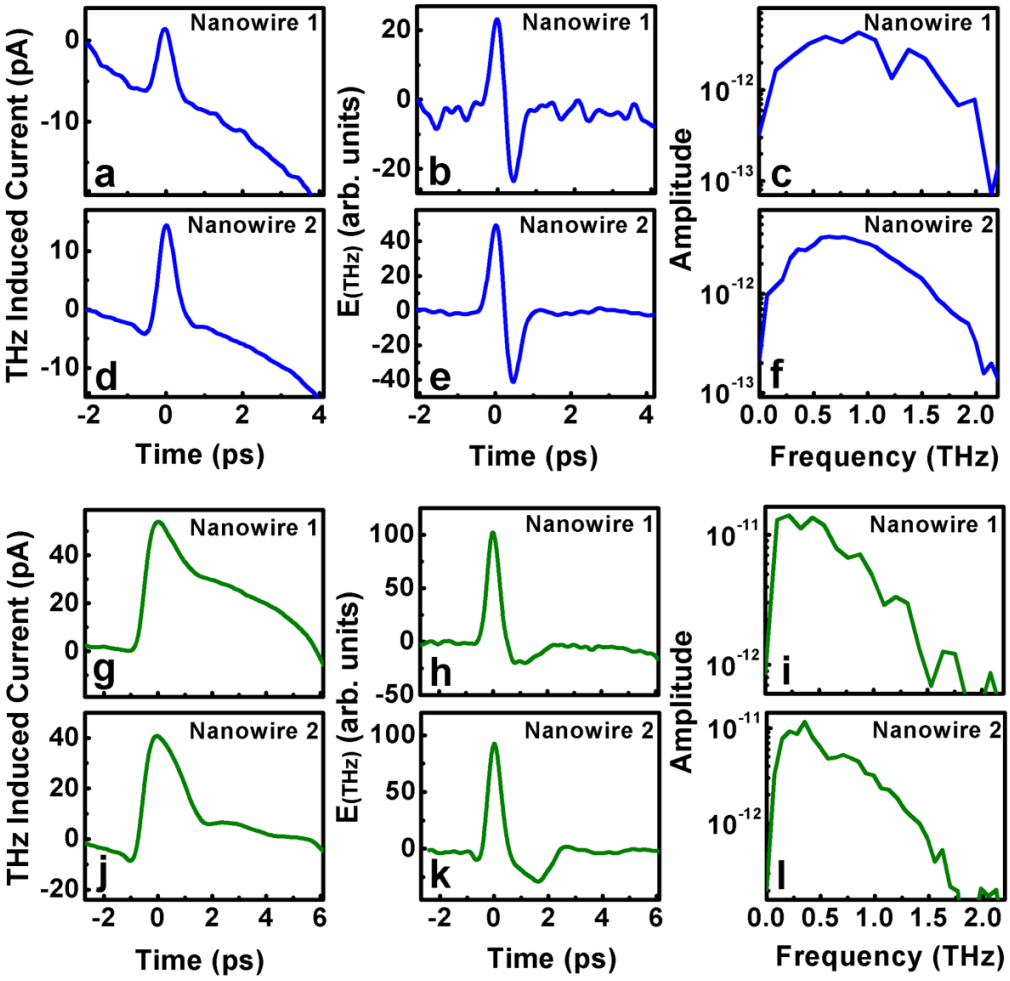

Figure 6.7: THz responses measured from single InP nanowire detectors with both strip-line (blue) and bow-tie (green) electrode structures. Left: unprocessed THz-induced current. Centre: calculated time-domain electric field. Right: amplitude frequency spectrum of the device.

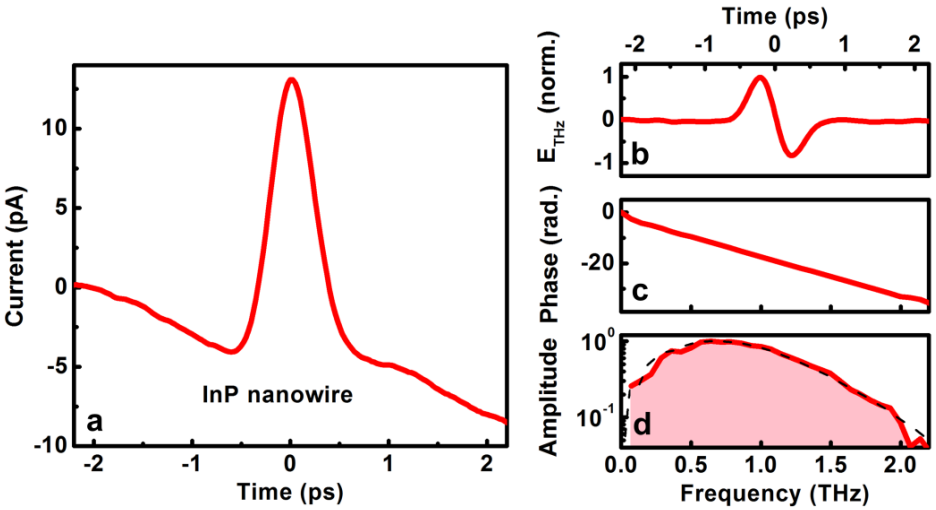

Figure 6.8: THz response characteristics of a typical (strip-line) single InP nanowire THz detector: (a) THz-induced current (measured from a single nanowire detector with strip-line electrode geometry); (b), (c), (d) processed data from (a): calculated time-domain THz electric field, phase and amplitude frequency spectrum. The dashed line is the reference spectrum obtained from a standard bulk electro-optic crystal detector.

Traditional InP receivers (bulk Fe^{+}-implanted InP) with the same (bow-tie and strip-line) device geometries were characterised in the same THz-TDS system to compare with InP single nanowire detectors. Finite-difference time-domain (FDTD) simulation results are also shown for reference. Figure 6.9 shows the THz responses obtained from single InP nanowire detectors, simulated antennas and ion-implanted InP receivers (bulk reference) for both the strip-line and bow-tie configurations. It can be seen that the response waveform and spectral profile measured from the InP single nanowire agree very well with the simulation results (only integrating sampling type). The bulk references show similar performances to those of nanowire detectors however with a small distortion (see the defined regions by the red dashed-line squares in Figure 6.9) observed in the measured waveform signal and frequency spectrum, particularly for the case of the bulk bow-tie detector. This may be attributed to the ion-implanted InP detector being of intermediate type [16] as determined by their short carrier lifetime (< 6 ps), which requires further correction in terms of deconvolution (as will be discussed and shown in Figure 6.10). However, such correction would not affect the SNR analysis.

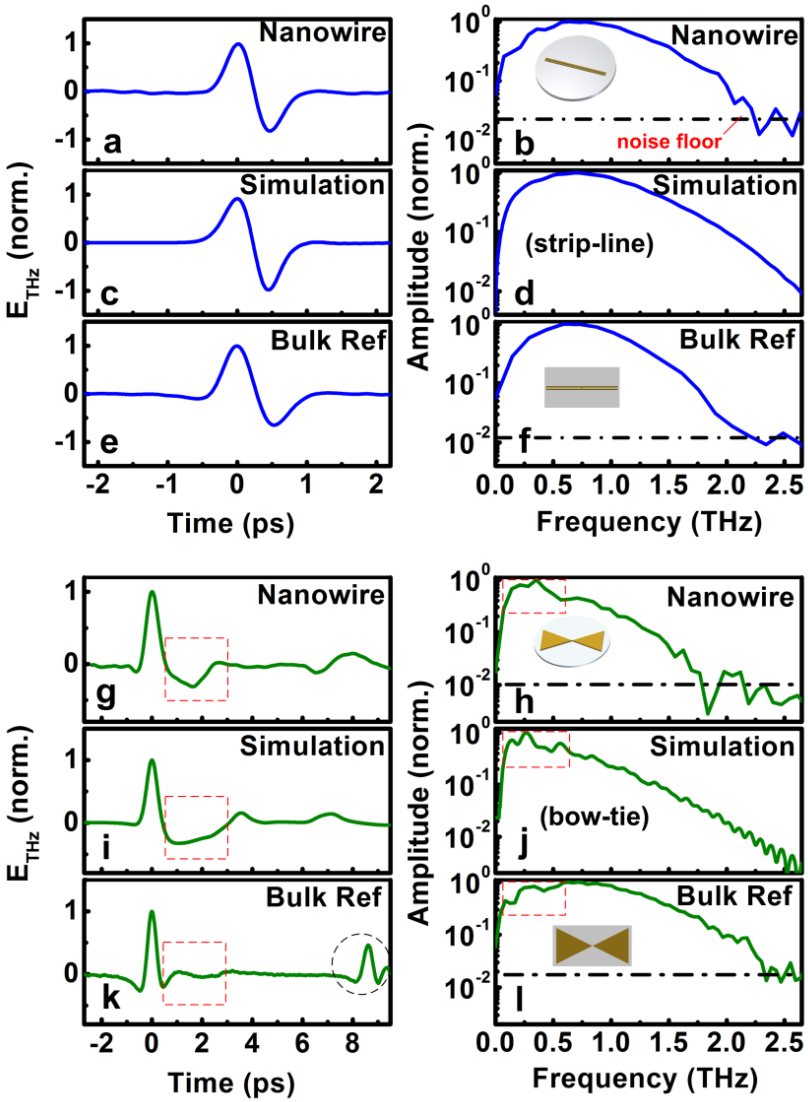

Figure 6.9: THz response obtained from (a), (b), (g), (h) single InP nanowire detectors; (c), (d), (i), (j) simulated antennas; (e), (f), (k), (l) bulk InP receivers, with contact geometry of strip lines (blue solid line) and bow tie (green solid line). All the figures on the left are the time-domain electric field and those on the right are their corresponding frequency-domain amplitude spectra. (Dash dot line: noise floor. Inset: schematic diagrams of the samples.)

In addition, the bulk ion-implanted InP receiver shows a small replica of the main THz pulse at ~ 8.5 ps (see the circle in Figure 6.9(k) with a black dashed line border) in response spectra, due to the reflected THz pulse from the bottom surface of the bulk ion-implanted InP substrate (~ 0.4 mm thick). In contrast, no reflection signal can be observed in the nanowire detector response spectra (see Figure 6.9(g)), since the InP single nanowire detectors are fabricated on

thick quartz substrates (~ 2 mm) with a single nanowire as the active component, resulting in a long time-domain sampling window (and hence enabling higher spectral resolution measurements). Therefore, more details (as good as the simulated spectrum) can be measured by the nanowire detector in its response spectrum, as highlighted with the red dashed-line squares in Figures 6.9(h) and (j), while some spectroscopic information is lost in the bulk detector due to the limited spectral resolution (see the red dashed-line squares in Figure 6.9(l)).

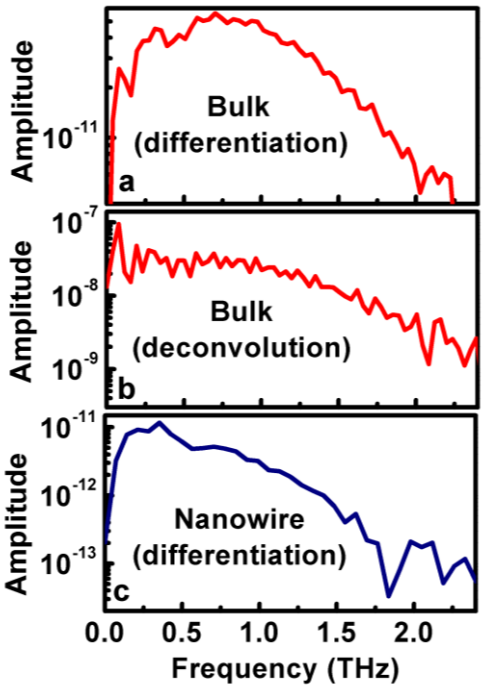

Figure 6.10: Comparison of THz response spectra calculated by (a) differentiation and (b) deconvolution of the photocurrent obtained from a Fe^+ ion-implanted InP receiver with bow-tie geometry. (c) A reference THz response spectrum calculated by differentiation of the photocurrent obtained from an InP single nanowire photoconductive THz detector.

To correct the distortion observed in the measured waveform signal for the case of the traditional bow-tie Fe^+ ion-implanted receiver (see Figure 6.9), deconvolution was performed. Details of the correction method have been described in Section 2.4.2. Figure 6.10 shows the THz response spectrum of an ion-implanted InP receiver processed without (a) and with (b) deconvolution. The corrected spectrum of the InP receivers is similar to that of the single InP nanowire detector as shown in Figure 6.10(c), which confirmed that the Fe^+ ion-implanted

receiver is of intermediate type (see Section 2.4.2). In theory, for the case of strip-line Fe^+ ion-implanted receiver, such response correction also needs to be done. However, it is hard to see the change before and after response correction in this work, as there is much less distortion in the measured response waveform signal (see Figure 6.9(e)) due to the use of strip-line device geometry.

To further quantitatively compare the InP nanowire detectors with GaAs/AlGaAs nanowire detectors studied in this thesis, Figure 6.11 shows the THz responses measured from an InP single nanowire detector and a GaAs/AlGaAs single nanowire detector. Since they have the same device geometry, their responses show similarities both in terms of current profile and spectral response. However, the response for the InP single nanowire detector is 2-3 times higher in magnitude compared to that of the GaAs/AlGaAs single nanowire detector while lower in noise floor and thus broader in detection bandwidth. These results are consistent with previous measurements and analysis of the InP nanowires, which show higher photocurrents (photosensitivity) but shorter photoconductivity lifetimes, critical for THz detector applications.

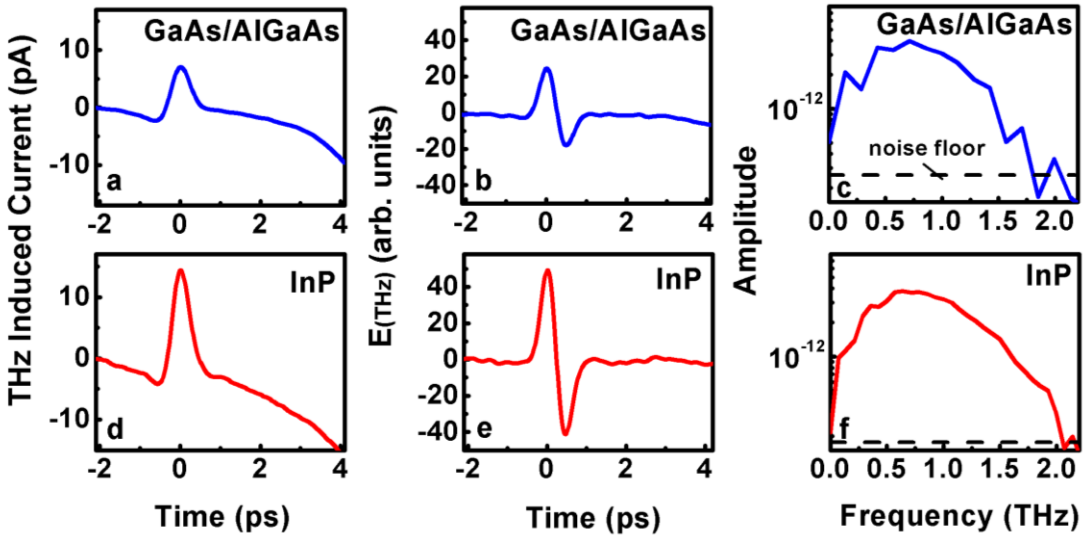

Figure 6.11: Comparisons in THz responses measured from a GaAs/AlGaAs single nanowire detector (blue solid line) and an InP single nanowire detector (red solid line) with the same (strip-line) device geometry. Left: unprocessed THz-induced current. Centre: calculated time-domain electric field. Right: amplitude frequency spectrum of the device.

A comparative summary of device performance between the nanowire THz detectors and traditional ion-implanted THz receivers is listed in Table 6.1. Despite having a pA-level response and a relatively long photoconductivity lifetime, the single nanowire detectors show comparable SNR to bulk receivers, owing to the nature of low dark currents (low background noise). Overall, InP nanowire detectors show much higher response current than GaAs/AlGaAs nanowire detectors. However, the better SNR (which means more stable signal from scan to scan) for strip-line GaAs/AlGaAs-detectors could attribute to the direct-sampling signal component from the GaAs capping layer. It is interesting to note that the dynamic range for each detector is significantly different, which likely arises from different coupling effects between antenna geometry (bow-tie vs strip-line) and material parameters (nanowire vs bulk). It may be useful to further simulate and measure the impedance, capacitance and coupling efficiency of each antenna design for further improvement.

Table 6.1: A comparison of device performance among GaAs/AlGaAs single nanowire detector, InP single nanowire detector and traditional ion-implanted InP receiver. BT: bow-tie geometry; SL: strip-line geometry. All dark I-V measurements were conducted at bias of 1V.

Device type / **Performance**	**GaAs/AlGaAs Single Nanowire**		**InP Single Nanowire**		**Ion-implanted InP Bulk Receiver**	
	SL	**BT**	**SL**	**BT**	**SL**	**BT**
Conductivity Lifetime (ps)	~ 4600		~ 1710		< 6	
Dark Current (pA)	~10	~10	~10	~10	~ 69200	~ 45700
THz Signal (pA)	7.96	13.6	19.5	52.6	676.6	544.3
Signal-to-noise Ratio	34	31	21	40	70	43
Dynamic Range	97	180	103	575	540	280

To demonstrate the potential of the InP single nanowire detectors for practical use, a number of 0.33 (± 0.01) mm paper cards were inserted into the THz path and their transmission spectra were characterised using the single InP nanowire detectors. Figure 6.12(a) shows the optical setup used in this measurement. Figures 6.12(b)-(j) show the THz responses measured by a

single InP nanowire, a bulk InP receiver and a standard electro-optic detection crystal (ZnTe), with and without the presence of cards in the THz-TDS system. It can be seen that, despite having a pA-level THz photocurrent signal, the single InP nanowire shows comparable sensitivity to that of traditional bulk detectors in both measured THz amplitude and phase spectra. Based on the data shown in Figure 6.12, the absorption coefficient [17] (Figure 6.13(a)) and refractive index spectra [18-20] (Figure 6.13(b)) of the card were obtained based on the method described in Section 2.6. The refractive indices measured from the three different types of detectors are similar and constant (~ 1.55) over the frequency band extending from 0.4 to 1.6 THz, consistent with the value reported in the literatures [20]. This result indicates that the InP single nanowire detectors have sufficient potential to be utilised for practical applications.

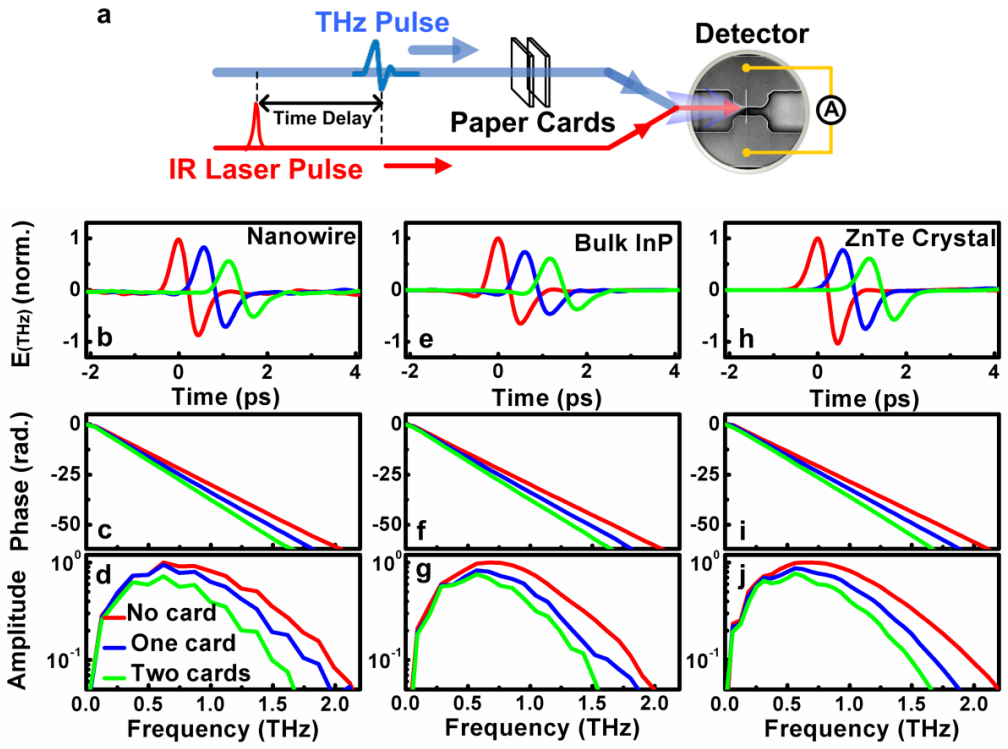

Figure 6.12: (a) Schematic representation of the transmission measurement in a THz-TDS system. (b) - (j) THz responses measured from three different types of detectors with and without the presence of paper cards (red solid line: no card; blue solid line: one card; green solid line: two cards); (b), (c), (d) a strip-line InP single nanowire THz detector; (e), (f), (g) a strip-line ion-implanted InP receiver; (h) (i), (j) a ZnTe electro-optic crystal. Top row: calculated time-domain electric field. Centre row: frequency-domain phase information. Bottom row: frequency-domain amplitude spectrum.

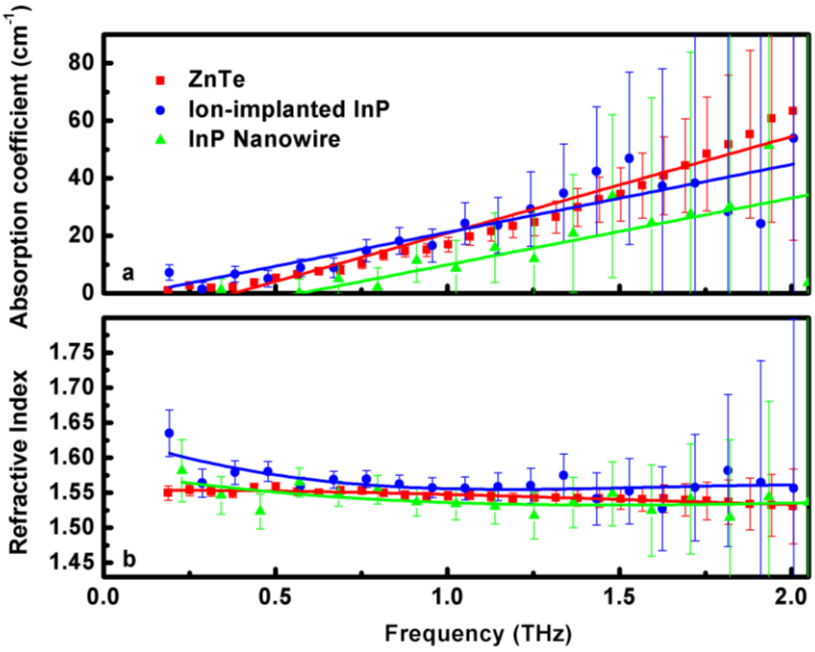

Figure 6.13: (a) Absorption coefficient and (b) refractive index spectra of a paper card measured by three different types of THz detectors. The solid lines are a guide to eye and the variations in adjacent points of data sets can be attributed to the noise.

6.5 Summary

Photoconductive THz detectors based on single InP nanowires were demonstrated in this Chapter. The InP nanowires exhibit higher crystal quality (core-only, stacking-fault free and pure WZ structure), higher carrier mobility (1260 ± 320 cm^2 V^{-1} s^{-1}) and relatively shorter carrier lifetime, compared to that of the best GaAs/AlGaAs nanowires (Sample A as described in Chapters 4 and 5), which is more desirable for THz detection. By using optimised device geometry designs, InP single nanowire detectors with a broad bandwidth (0.1-2.0 THz), high amplitude and phase sensitivity were achieved, which were found to be comparable to that of the traditional ion-implanted bulk InP receiver and the standard electro-optic ZnTe crystal THz detector. By further using these InP single nanowire detectors as microscopic coherent sensors in a THz-TDS system, the THz transmission spectra of paper cards were successfully measured showing excellent spectral and phase sensitivities and thus great potential for spectroscopic applications.

References

[1] I. Gyuro, "MOVPE for InP-based optoelectronic device application," *III-Vs Review,* vol. 9, pp. 30-35, 1996.

[2] H. J. Joyce, C. J. Docherty, Q. Gao, H. H. Tan, C. Jagadish, J. Lloyd-Hughes, L. M. Herz, and M. B. Johnston, "Electronic properties of GaAs, InAs and InP nanowires studied by terahertz spectroscopy," *Nanotechnology,* vol. 24, pp. 214006-214012, 2013.

[3] H. J. Joyce, J. Wong-Leung, C. K. Yong, C. J. Docherty, S. Paiman, Q. Gao, H. H. Tan, C. Jagadish, J. Lloyd-Hughes, L. M. Herz, and M. B. Johnston, "Ultralow surface recombination velocity in InP nanowires probed by terahertz spectroscopy," *Nano Letters,* vol. 12, pp. 5325-5330, 2012.

[4] Q. Gao, D. Saxena, F. Wang, L. Fu, S. Mokkapati, Y. A. Guo, L. Li, J. Wong-Leung, P. Caroff, H. H. Tan, and C. Jagadish, "Selective-area epitaxy of pure wurtzite InP nanowires: High quantum efficiency and room-temperature lasing," *Nano Letters,* vol. 14, pp. 5206-5211, 2014.

[5] A. Maharjan, K. Pemasiri, P. Kumar, A. Wade, L. M. Smith, H. E. Jackson, J. M. Yarrison-Rice, A. Kogan, S. Paiman, Q. Gao, H. H. Tan, and C. Jagadish, "Room temperature photocurrent spectroscopy of single zincblende and wurtzite InP nanowires," *Applied Physics Letters,* vol. 94, 193115, 2009.

[6] N. Jiang, Q. Gao, P. Parkinson, J. Wong-Leung, S. Mokkapati, S. Breuer, H. H. Tan, C. L. Zheng, J. Etheridge, and C. Jagadish, "Enhanced minority carrier lifetimes in GaAs/AlGaAs core-shell nanowires through shell growth optimization," *Nano Letters,* vol. 13, pp. 5135-5140, 2013.

[7] N. Jiang, P. Parkinson, Q. Gao, S. Breuer, H. H. Tan, J. Wong-Leung, and C. Jagadish, "Long minority carrier lifetime in Au-catalyzed GaAs/Al$_x$Ga$_{1-x}$As core-shell nanowires," *Applied Physics Letters,* vol. 101, 023111, 2012.

[8] F. Wang, Q. Gao, K. Peng, Z. Li, Z. Y. Li, Y. N. Guo, L. Fu, L. M. Smith, H. H. Tan, and C. Jagadish, "Spatially resolved doping concentration and nonradiative lifetime profiles in single Si-doped InP nanowires using photoluminescence mapping," *Nano*

Letters, vol. 15, pp. 3017-3023, 2015.

[9] G. L. Tuin, M. T. Borgström, J. Trägårdh, M. Ek, L. R. Wallenberg, L. Samuelson, and M.-E. Pistol, "Valence band splitting in wurtzite InP nanowires observed by photoluminescence and photoluminescence excitation spectroscopy," *Nano Research*, vol. 4, pp. 159-163, 2011.

[10] A. De and C. E. Pryor, "Predicted band structures of III-V semiconductors in the wurtzite phase," *Physical Review B*, vol. 81, 155210, 2010.

[11] J. Wallentin, N. Anttu, D. Asoli, M. Huffman, I. Åberg, M. H. Magnusson, G. Siefer, P. Fuss-Kailuweit, F. Dimroth, and B. Witzigmann, "InP nanowire array solar cells achieving 13.8% efficiency by exceeding the ray optics limit," *Science*, vol. 339, pp. 1057-1060, 2013.

[12] Y. Cui, J. Wang, S. R. Plissard, A. Cavalli, T. T. Vu, R. P. van Veldhoven, L. Gao, M. Trainor, M. A. Verheijen, and J. E. Haverkort, "Efficiency enhancement of InP nanowire solar cells by surface cleaning," *Nano Letters*, vol. 13, pp. 4113-4117, 2013.

[13] K. Peng, P. Parkinson, L. Fu, Q. Gao, N. Jiang, Y. N. Guo, F. Wang, H. J. Joyce, J. L. Boland, H. H. Tan, C. Jagadish, and M. B. Johnston, "Single nanowire photoconductive terahertz detectors," *Nano Letters*, vol. 15, pp. 206-210, 2015.

[14] J. L. Boland, S. Conesa-Boj, P. Parkinson, G. Tütüncüoglu, F. Matteini, D. Rüffer, A. Casadei, F. Amaduzzi, F. Jabeen, C. L. Davies, H. J. Joyce, L. M. Herz, A. Fontcuberta i Morral, and M. B. Johnston, "Modulation doping of GaAs/AlGaAs core-shell nanowires with effective defect passivation and high electron mobility," *Nano Letters*, vol. 15, pp. 1336-1342, 2015.

[15] J. L. Boland, S. Conesa-Boj, P. Parkinson, G. z. Tütüncüoglu, F. Matteini, D. Rüffer, A. Casadei, F. Amaduzzi, F. Jabeen, and C. L. Davies, "Modulation doping of GaAs/AlGaAs core–shell nanowires with effective defect passivation and high electron mobility," *Nano Letters*, vol. 15, pp. 1336-1342, 2015.

[16] E. Castro-Camus, L. Fu, J. Lloyd-Hughes, H. H. Tan, C. Jagadish, and M. B. Johnston, "Photoconductive response correction for detectors of terahertz radiation," *Journal of Applied Physics*, vol. 104, p. 053113, 2008.

[17] L. Duvillaret, F. Garet, and J. L. Coutaz, "A reliable method for extraction of material

parameters in terahertz time-domain spectroscopy," *IEEE Journal on Selected Topics in Quantum Electronics,* vol. 2, pp. 739-746, 1996.

[18] B. Hussain, M. Nawaz, M. Ahmed, and M. Y. A. Raja, "Measurement of thickness and refractive index using femtosecond and terahertz pulses," *Laser Physics Letters,* vol. 10, p. 055301, 2013.

[19] A. H. Cordes, D. H. Thomas, and J. P. von der Weid, "Phase measurements on terahertz waves," *Optics Letters,* vol. 38, pp. 3704-3707, 2013.

[20] T. Hattori, H. Kumon, and H. Tamazumi, "Terahertz spectroscopic characterization of paper," *35th International Conference on Infrared, Millimeter, and Terahertz Waves (Irmmw-Thz 2010),* pp. 1-2, 2010.

Chapter 7

Photoconductive Terahertz Detectors with Enhanced Sensitivity Based on Axial n^+-i-n^+ InP Nanowires

7.1 Introduction

Having optimised both active material system and device design in previous chapters, this chapter seeks to further improve the efficiency of nanowire detectors to compete with traditional detectors. In traditional photoconductive terahertz (THz) electronics, contact quality is known to play a significant role in determining device performance [1]. Lower contact resistance leads to higher output power in photoconductive emitters; similarly, for effective detection, Ohmic contacts are essential to ensure maximum detection sensitivity [2]. However, the undoped single InP nanowire detectors described in Chapter 6 exhibit a clear Schottky interface between the nanowire and metal contact (see Figure 6.5). It is therefore important and necessary to create high-quality Ohmic contacts to further improve the performance of single InP nanowire detectors.

Typical approaches to form Ohmic metal-semiconductor contacts include thermal alloying [3, 4] and ion-implantation [5] at the contact region, which are not suitable processes for semiconductor nanowires as the former may lead to material thermal decomposition while the latter is challenging and risks material damage. A careful choice of contact metals can help [4], for example, non-annealed contacts including Ti/Au contacts have been widely used for the low temperature grown GaAs photoconductive THz antennas to achieve Ohmic behavior [4, 6, 7]. However, the very limited contact surface area for single nanowire devices may still lead to significant device-to-device variation in the contact quality. In this chapter, design, growth and characterisation of modulated doped n^+-i-n^+ axial structure in nanowires are proposed. By making electrical contact to highly doped end regions of the nanowire, low contact-resistance

n^+-i-n^+ InP single nanowire devices can be realised for highly-sensitive THz detection.

7.1 Nanowire Doping

To achieve appropriate doping in the n^+-i-n^+ single InP nanowires, the relationship among nanowire growth, doping characteristics and resultant device contact quality was firstly studied. Undoped and uniformly n-type doped InP nanowires with different doping concentrations were grown for such an investigation. It is noted that effective characterisation of spatially varying carrier densities in a single nanowire is highly challenging due to the small volumes of material involved and thus limited techniques. An all-optical technique developed by the Australian National University group [8] was used to measure the local carrier density with diffraction-limited resolution. By correlating these measurements with 2- and 4-terminal contact electrical studies, the effectiveness of the modulation doping approach was evaluated and used for design/growth of the axial n^+-i-n^+ nanowire structure.

7.1.1 Growth of Uniformly-Doped InP Nanowires

The undoped and uniformly-doped InP nanowires were grown on bulk (111)A InP substrates, using the selective-area metalorganic vapour phase epitaxy (SA-MOVPE) technique in a commercial MOVPE reactor. The growth of undoped InP nanowires followed the same process as described in Section 6.2.1, which has been shown to produce unintentionally n-type doped, defect-free and pure wurtzite (WZ) InP nanowires [8, 9]. The unintentional doping in the undoped InP nanowires can be attributed to the background impurities in the MOVPE precursors [10]. For intentional (uniform) n^+ doping, gaseous silane ($SiH_{4)}$ was introduced during nanowire growth, with all other parameters being kept unchanged to produce, Si-doped n-type [11] InP nanowires. In order to investigate the effect of Si doping, the dopant flow rates were set from 5.1×10^{-8} to 1.0×10^{-6} mol/min to produce a series of uniformly-Si-doped InP nanowire samples with different doping concentrations.

7.1.2 Material Characterisation

7.1.2.1 Scanning/Transmission Electron Microscopy

Both undoped and uniformly-Si-doped InP nanowires were found to be structurally uniform, with a diameter in the range of 220-260 nm and a length of 8-12 μm. The scanning-electron-microscopy (SEM) image of a typical doped single InP nanowire studied in this work is shown in Figure 7.1(a). The effect of Si doping on crystal defect evolution in these InP nanowires was examined by transmission electron microscopy (TEM). Figures 7.1(b)-(d) display the TEM images for InP nanowires grown with SiH_4 flow rates of 0, 5.1×10^{-8}, 3.1×10^{-7} mol/min, which will be named as undoped, lightly-doped, heavily-doped InP nanowires, respectively. The TEM images show that all nanowires have WZ phase structures (Figure 7.1(e)) and are free of stacking faults. The presence of Si in InP nanowires was found to be below the energy-dispersive X-ray detection limit (~ 0.3 atomic percentage, equivalent to 1×10^{19} cm^{-3}) for all samples, which means the doping level for all Si-doped InP nanowires studied in this dissertation is lower than 1×10^{19} cm^{-3}.

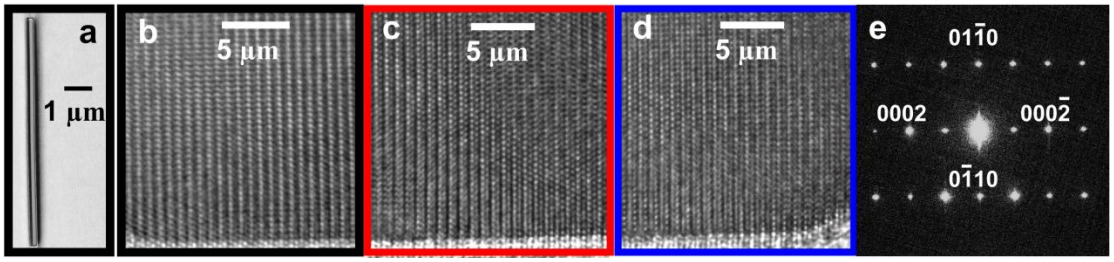

Figure 7.1: (a) A SEM image of a uniformly-Si-doped single InP nanowire studied in this work. (b) - (d) TEM images taken along [-2110] zone axis from the undoped, lightly-doped, heavily-doped InP nanowires, respectively. (e) Selected area electron diffraction pattern of a typical Si-doped InP nanowire confirming the WZ phase structure.

7.1.2.2 Spatially-Resolved Doping Concentration by Time- and Power-Dependent Photoluminescence

To measure the doping concentration and variation along the single InP nanowire axis, a novel optical technique [8] based on power-dependent photoluminescence (PL) and time-resolved PL measurements was employed. This technique was realised using a micro-PL spectroscopy setup incorporating both a PL spectroscopy and a time-correlated single photon counting system as described in Section 3.2.3. A linearly polarised pulsed laser (522 nm) with 300fs pulsed width, 20.8 MHz repetition rate and beam spot size of ~ 635 nm (in diameter) was used to photo-excite the nanowire. A neutral density filter wheel was employed to control the laser excitation power. A two-dimensional motorised translation stage with 200 nm minimum incremental step size was used to control the laser excitation position along the nanowire.

This optical method is based on the analysis of carrier rate equation, expressed by

$$\frac{\mathrm{d}n}{\mathrm{dt}} = G - \frac{n}{\tau_{nr}} - B(\mathrm{N}_D + n)n - \frac{4\mathrm{S}}{\mathrm{d}}n \qquad (7.1)$$

where $n(t)$ is the time-dependent carrier density, G is the carrier generation rate, τ_{nr} is the nonradiative recombination lifetime, B is the radiative recombination rate constant, N_D is the doping concentration, and S and d are the surface recombination velocity and diameter of the measured InP single nanowire, respectively. The Auger recombination rate is ignored in equation (7.1) due to the small excitation power used in measurements.

Under the excitation of a short pulsed laser, it is reasonable to assume that photo-induced carriers in the nanowire are generated as a delta function at $\mathrm{t} = 0$, and thus G is equal to zero in equation (7.1) as the initial carriers are only induced at t = 0. For the InP nanowires studied in this work, their surface recombination velocity has been found to be about 161 cm/s[8, 9] such that the surface related term $\frac{4\mathrm{S}}{\mathrm{d}}n$ can be ignored in equation (7.1) as it is far less than nonradiative recombination $\frac{n}{\tau_{nr}}$. By setting τ_{nr} as the system time and $N1 = 1/(B\tau_{nr})$ as carrier density unit, the equation (7.1) can be simplified as

$$\frac{dn'}{dt'} = -(1 + n_D)n' - (n')^2 \qquad (7.2)$$

where n' is the carrier density in units of $N1$; n_D is the doping density in units of $N1$; t' is the time unit of τ_{nr}. To solve equation (7.2), the power-dependent PL measurements were performed as shown in Figure 7.2(a). The power-dependent PL intensity curve can be expressed as

$$I(P) \propto n_{rad} = \log\left(\frac{1+n_D}{n_0}\right) - \log\left(\frac{1+n_0+n_D}{n_0}\right) + n_0 \qquad (7.3)$$

where n_{rad} is the carrier density involved in radiative recombination, n_0 is the initial carrier density that is proportional to incident laser power. By fitting the power-dependent PL intensity curves as shown in Figure 7.2(b), the doping concentration n_D in unit of $N1$ can be extracted.

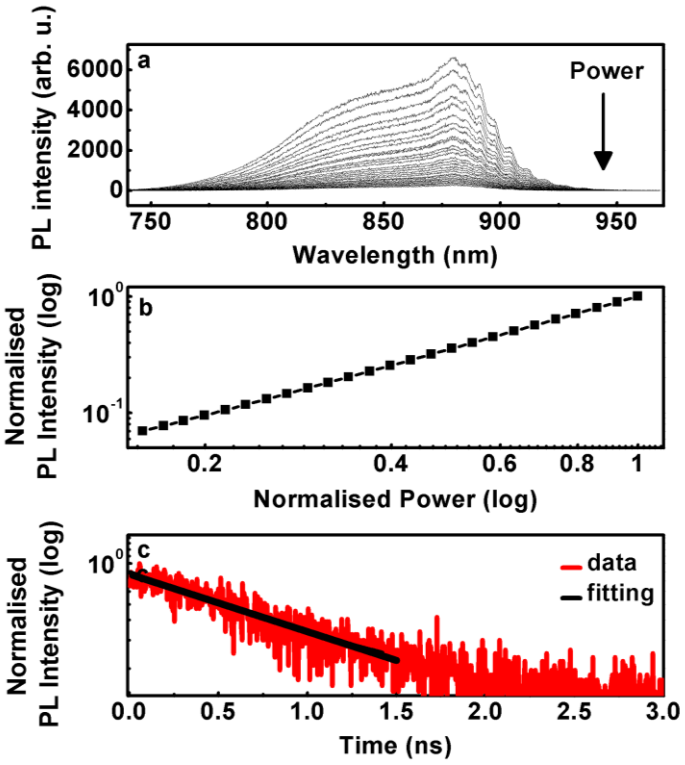

Figure 7.2: (a) Power-dependent PL spectra (with an incident power decreasing from the top to the bottom) taken from a single InP nanowire; (b) PL integrated intensity as a function of power obtained from (a); (c) PL intensity decay as function of time under a low excitation power in (a), fitted by a single exponential decay with lifetime of 0.92 ns for the InP nanowire.

Then using the extracted doping concentration n_D (in units of $N1$), the total carrier decay with respect to time in the nanowire can be calculated from

$$n'(t') = \frac{\frac{n_0}{1+n_D+n_0}(1+n_D)}{e^{(1+n_D)t'} - \frac{n_0}{1+n_D+n_0}} \tag{7.4}$$

which is proportional to the PL intensity decay (as shown in Figure 7.2(c)). By fitting equation (7.4) to the PL intensity decay as a function of time, the non-radiative lifetime τ_{nr} can be extracted. According to the value of τ_{nr} and B, the doping concentration N_D can be extracted as demonstrated in Figure 7.3.

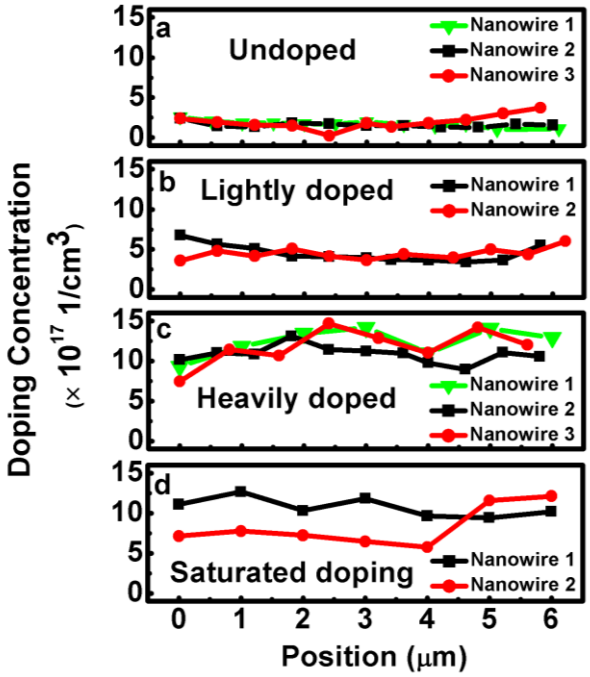

Figure 7.3: Doping profiles of single InP nanowires with (a) unintentional, (b) light, (c) heavy and (d) saturated doping measured using the technique described in this section.

Figure 7.3 shows the optically measured doping profiles along the length of undoped, lightly-doped, heavily-doped and saturated-doped InP single nanowires, respectively. Since inhomogeneity in a nanowire ensemble is known to lead to variations in doping concentration among nanowires, multiple sets of measurements were performed to evaluate an average

doping level for each growth condition. The average doping concentration for the undoped InP nanowires is ~ 0.17×10^{18} cm^{-3} and for the lightly doped nanowires is ~ 0.49×10^{18} cm^{-3}. However, by continuously increasing SiH_4 flow rate during growth, the Si incorporation became uncontrollable. The heavily-doped samples show some variation in doping concentration both among nanowires (with values ranging from 1.08×10^{18} to 1.76×10^{18} cm^{-3}) and along the single nanowire axis (see Figure 7.3(c)). With an increase of SiH_4 flow rate to 1.0×10^{-6} mol/min, Si doping concentration seems to be saturated, as suggested in Figure 7.3(d), where a doping level of only ~1×10^{18} cm^{-3} was achieved. The understanding of nanowire dopant is worthy of further study in the future. This chapter will focus on electrical characterisations of the undoped, lightly-doped and heavily-doped InP nanowires for subsequent growth design of the axial n^+-i-n^+ InP nanowire structure.

7.1.3 Electrical Characterisation

The uniformly-doped InP nanowires with different Si doping concentrations were fabricated into both 2-terminal and 4-terminal single nanowire devices for current-voltage (I-V) measurements to examine their contact quality. 2-terminal measurements reveal the overall behaviour including contact type (Schottky/Ohmic) and quality of the nanowire device. Furthermore, 4-terminal measurements allow the accurate measurement of nanowire resistivity without the influence of contact resistance [12] (see Section 3.4.3). The device geometry is shown as an inset image in Figure 7.4. Figure 7.4 displays the room-temperature 4-terminal dark I-V characteristics of the undoped, lightly-doped and heavily-doped InP single nanowires, respectively, showing a clear decrease in nanowire resistance with increasing of Si doping, consistent with their doping concentration analysis shown in Figures 7.3 (a)-(c). The resistance between the 2 internal contacts (separated by 1.5 μm distance), obtained by 4-terminal measurements, is found to be approximately 4×10^{10} Ω, 1×10^{9} Ω and 2×10^{5} Ω for the undoped, lightly-doped and heavily-doped InP nanowires, respectively.

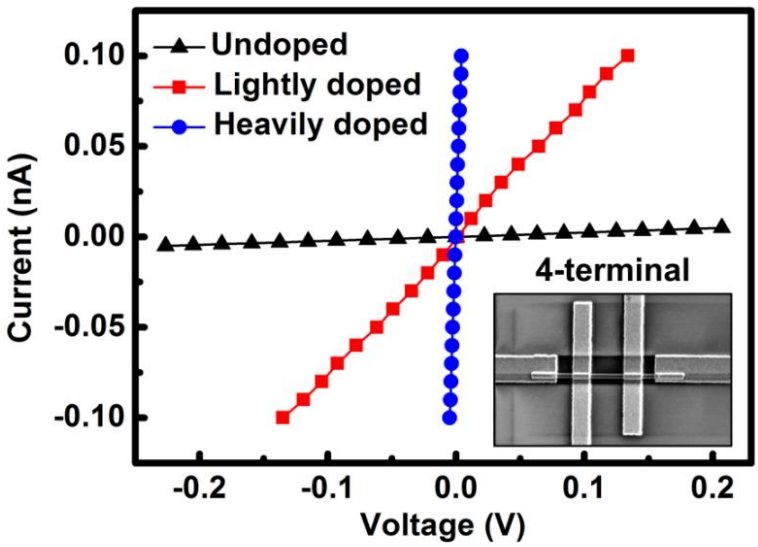

Figure 7.4: Dark I-V characteristics of the InP nanowires from the same growths as described in Figures 7.3(a) - (c) based on a 4-terminal contact (inset: SEM image of a single InP nanowire device having four-terminal contacts).

Figure 7.5(a) shows the room-temperature 2-terminal dark I-V characteristics of nanowire detectors from the undoped, lightly-doped and heavily-doped InP nanowires. The dynamic resistances of the undoped, lightly-doped and heavily-doped InP nanowires are one or two orders larger than those obtained in their 4-terminal measurements (see figure 7.5(b)-(d)). The difference between these two types of measurements highlights the large influence of contact resistances on nanowire device performance. It is also noted that in 2-terminal measurements, I-V characteristics for devices from undoped and lightly-doped single InP nanowires show typical Schottky behaviours, whereas the I-V characteristics for devices from heavily-doped single InP nanowires show (almost) Ohmic behaviour, indicating that Si doping above ~ 1×10^{18} cm^{-3} can create low-resistance contacts in the given geometry for InP nanowire devices [11].

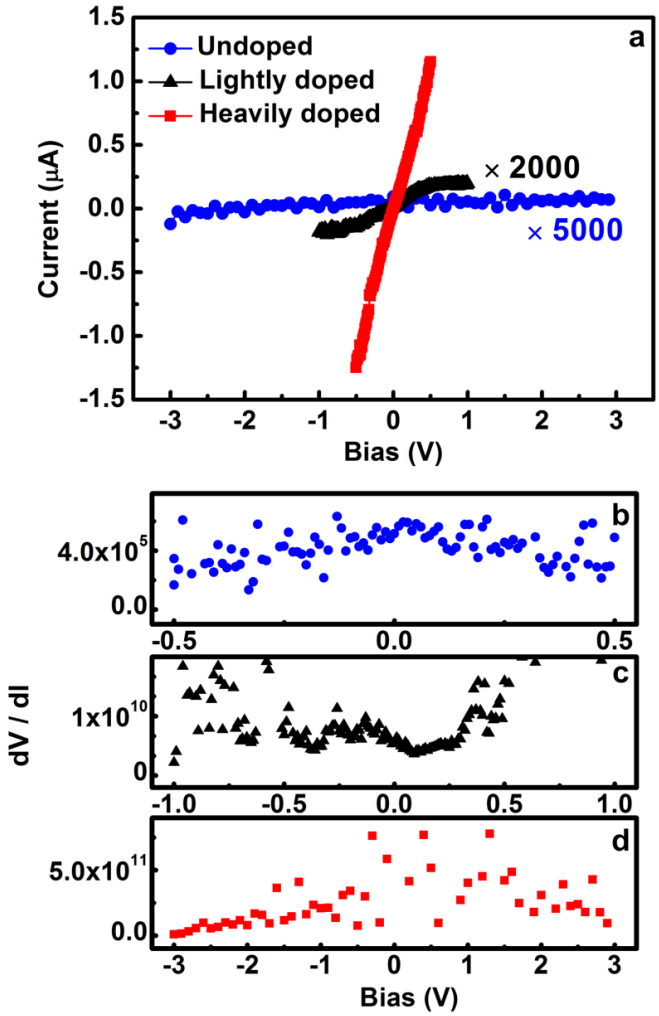

Figure 7.5: (a) 2-terminal dark I-V characteristics of single InP nanowires with unintentional, light and heavy doping. (b)-(d) The calculated dynamic resistances (dV/dI) from the data shown in (a).

7.1.4 Growth of n^+-i-n^+ InP Nanowires

Based on the understanding of the relationship between contact resistance and nanowire doping from the 2-terminal and 4-terminal I-V measurements, n^+-i-n^+ InP nanowire structure was designed to obtain Ohmic contacts to enhance device performance. To grow the n^+-i-n^+ nanowire structure, gaseous SiH_4 was introduced at the beginning of the growth, and shut off for i-section growth, and introduced again for the rest of growth. Each axial segment was grown for the same time (12 min), with the flow rates of SiH_4 set to 3.1×10^{-7}, 0 and 3.1×10^{-7}

mol/min, respectively, targeting a doping concentration profile of 1×10^{18}-1.5×10^{17}-1×10^{18} cm^{-3} along the single InP nanowire, with the nominal length of each section of ~ 3 μm.

7.1.5 Doping Profiling of n^+-i-n^+ InP Nanowires

The n^+-i-n^+ InP nanowires were characterised using the optical doping profiling technique [8] described earlier (see Section 7.1.2.2). Power-dependent PL spectra were measured point by point along the single n^+-i-n^+ nanowire. For each point, time-resolved PL intensity decay (under low excitation power condition) was recorded to extract a local PL lifetime for calculation of the doping concentration. The PL spectrum peak position profile along the nanowire was plotted in Figure 7.6(a), where both ends show a clear blue-shift in PL peak position, confirming they have a relatively high doping level of n-type [13] as designed. However, the PL peak position cannot be used to evaluate the doping level, since the PL peak position distribution is affected by excitation condition, intrinsic doping distribution and valence band splitting [8], which shows no linear relationship between PL peak position and doping concentration. The PL lifetime profile along the same nanowire is shown in Figure 7.6(b), indicating an asymmetric n^+-i-n^+ doping profile could have been formed within the single InP nanowire. Figure 7.6(c) displays the corresponding doping profile as determined by the optical technique. It can be clearly seen that the doping along the nanowire is also asymmetric, consistent with the PL lifetime profile. Nevertheless, the doping profile along the nanowire qualitatively follows the design of n^+-i-n^+ structure, with dopant levels ranging from 0.28×10^{18} to 1.48×10^{18} cm^{-3}, from the nominally undoped section to heavily-doped section. While the undoped section was found to be ~ 3 μm in length as expected, a significant difference in length of the other two sections was observed. This is attributed to the large variation in growth rate during nanowire growth, since it has been shown that SA-MOVPE InP nanowires grow much faster near the base [14]. Considering the three sections in the n^+-i-n^+ nanowires were grown for the same duration of time, it can be inferred that the end starting from 0 on the abscissa in Figures 7.6(a)-(c) is the base of nanowire. This region has a doping level of 1.05×10^{18} cm^{-3} with a slow transition profile from n^+-doped section to the undoped

section, likely due to being held at a high temperature during growth for a longer time, which led to diffusion of the Si dopant from the base. Accordingly, the other end with short growth length should be the tip of the nanowire, which has higher doping level of 1.48×10^{18} cm^{-3} and an abrupt doping profile next to the undoped section. This analysis on the base and tip of the nanowire has also been confirmed by SEM imaging of the nanowire as shown in Figure 7.6(d), where the tip end of the nanowire is easily identified by a flat surface profile and base end with a jagged profile (due to being broken off from the substrate). In order to obtain a symmetrical n^+-i-n^+ doping profile in the nanowire, such deviations should be accounted for by careful calibration of growth time for each segment and further optimisation of growth conditions to achieve a higher doping for n^+ region at the nanowire base.

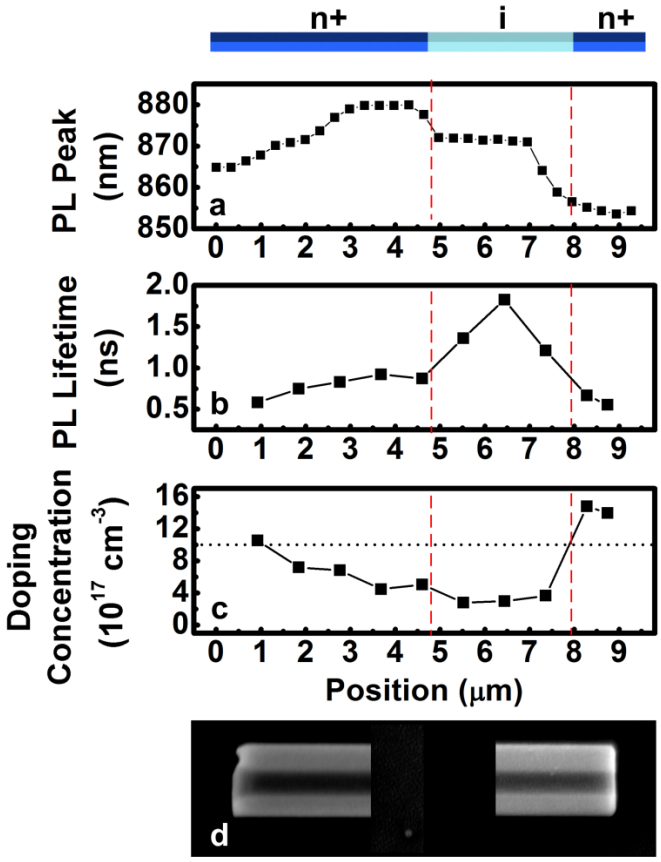

Figure 7.6: (a) PL spectrum peak position profile along a single n^+-i-n^+ InP nanowire studied in this work (position at 0 μm denotes the bottom of the nanowire where the growth starts). (b) The PL lifetime profile and (c) the corresponding doping profile along the same nanowire in (a). (d)The SEM images of the bottom (left) and top (right) parts of the InP nanowire.

7.2 Device Fabrication and Characterisation

7.2.1 Device Fabrication

Based on the doping profile analysis, Ti/Au (10 nm/300 nm) electrode contacts were fabricated onto the n^+-i-n^+ nanowires, covering each end with a length of ~ 1 μm (see Figure 7.7(a)). It was tested and found that a longer contact length (> 2 μm) would overlap with the undoped section and reduce the active area of the resultant device, while shorter contact length (< 800 nm) would reduce the contact area to the nanowire and degrade the contact quality. Conventional UV photolithography was employed to pattern the electrodes. An oxygen plasma etch was used to remove the photoresist residue on nanowires after development, followed by a 9.3% HCl chemical etching to remove native oxide layer around the nanowire surface. Ti/Au contacts were metallised using electron beam evaporation.

7.2.2 Photocurrent Mapping

In order to confirm the improvement of contact quality from the n^+-i-n^+ design, spatially-resolved photocurrent mapping of the single InP nanowire devices was performed under 532 nm continuous-wave laser excitation. Figure 7.7(b) shows photocurrent distribution scanned along an undoped InP single nanowire device as well as an n^+-i-n^+ InP single nanowire device under the biases of ± 0.5 V. It can be seen that the photocurrent predominantly originates from the central, intrinsic region of the nanowire in the n^+-i-n^+ nanowire device, while the photocurrent is mainly from the contact junctions in the undoped nanowire device (due to the formation of back-to-back Schottky contacts). This indicates that the n^+ section of the n^+-i-n^+ nanowire worked well as intended, lowering the contact barrier height, to form low-resistance contacts at both ends of the nanowire device. It is also noted that the photocurrent profile along the n^+-i-n^+ nanowire is in good agreement with the doping profiles shown in Figures 7.6(a)-(c), confirming that the photocurrent in the n^+-i-n^+ nanowire device mostly arises from the undoped section. Importantly, the n^+-i-n^+ nanowire device exhibits strong photosensitivity even under room light illumination, whereas the undoped nanowire

device barely has an observable photo-response under the same condition (Figure 3(d)). A quantitative photo-response comparison between the n^+-i-n^+ and undoped single nanowire devices is provided in Figures 7.7(c) and (d).

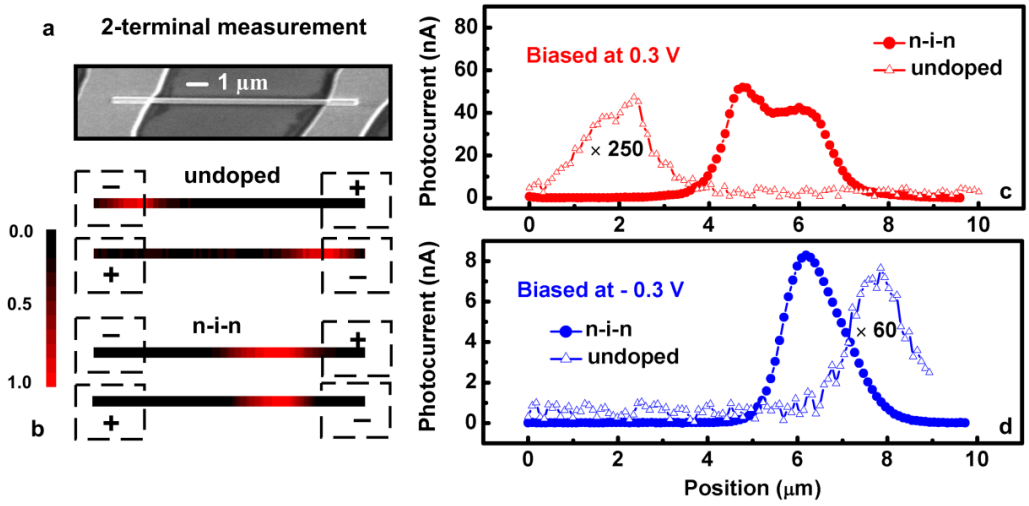

Figure 7.7: (a) SEM image of a typical 2-terminal n^+-i-n^+ single InP nanowire device fabricated in this study. (b) Photocurrent maps of an undoped (top) and an n^+-i-n^+ (bottom) single InP nanowire device at biases of ± 0.5 V scanned using a 532 nm continuous-wave laser with a beam spot size of ~ 720 nm (in diameter) and a scan step of 150 nm. The colour from red to black in the mapping corresponds to the (normalised) photocurrent intensity from maximum to the minimum for each device. (c) and (d) show the comparison of photocurrent profiles along an undoped and an n^+-i-n^+ single InP nanowire devices measured using a WITec alpha300S scanning microscopy system in (b). The two detectors were fabricated with the identical process and excited under the same laser illumination at a fluence of 56.3 nW/μm^2.

7.2.3 Power-Dependent Photocurrent

Under the similar setup as used for the photocurrent mapping measurements, power-dependent photocurrent measurements scanned along the n^+-i-n^+ nanowire device were also carried out and the results are plotted in Figure 7.8, indicating that the non-metallised n^+ sections also contribute to the total photocurrent. The Si doping at this section could be responsible for the reduced yield of photocurrents, since the free carrier absorption [15]

become significant when doping increasing which may compete with band to band absorption, thereby reducing the number of available photons to the device. For optimal photo-detection in the future, the length of n^+ sections in n^+-i-n^+ nanowires should be reduced and optimised for the main function of contacting.

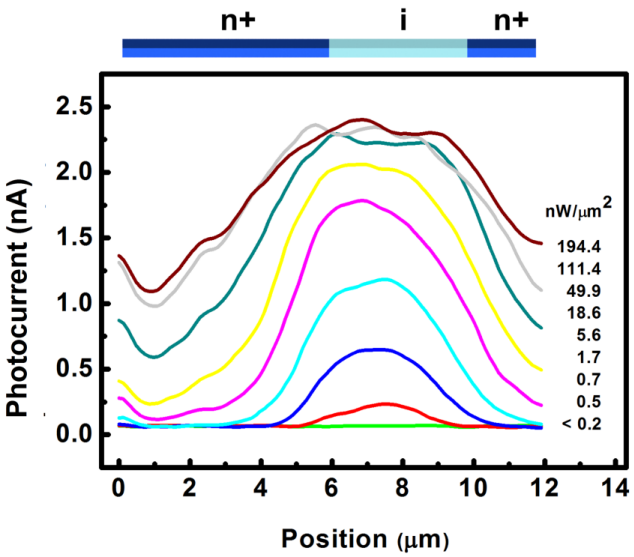

Figure 7.8: (a) Power-dependent photocurrents scanned along an n^+-i-n^+ InP single nanowire device under different excitation powers, where the device is biased at - 0.15 V.

7.2.4 Bias-Dependent Photocurrent

In order to examine the influence of doping asymmetry (observed in Figure 7.6) on device performance, bias-dependent photocurrent measurements along the single n^+-i-n^+ nanowire device were performed. It can be seen from Figure 7.9(a) that the photocurrent from the n^+-i-n^+ device shows a distinct difference in intensity under positive and negative bias. However, the spatial distribution of photocurrent is insensitive to the applied bias direction and always observed predominantly from the nominally undoped section.

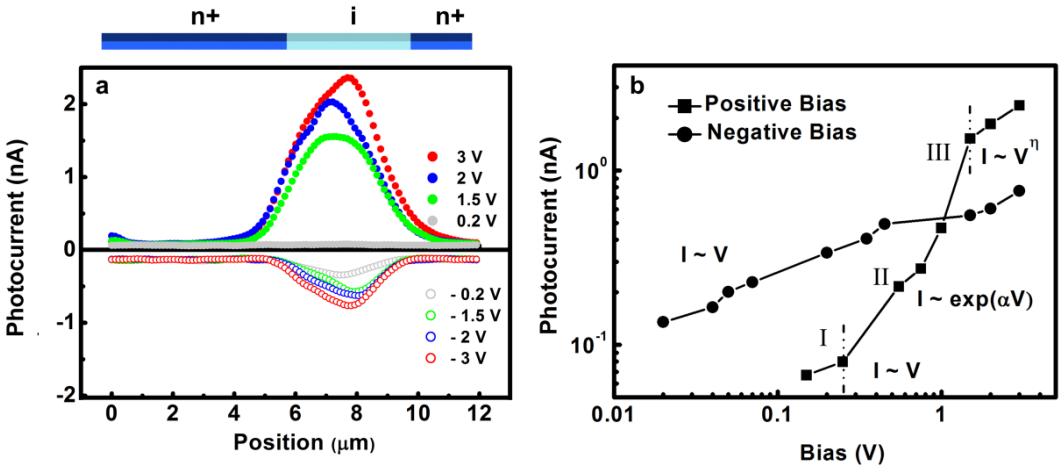

Figure 7.9: (a) Bias-dependent photocurrents scanned along an n^+-i-n^+ InP single nanowire device (under illumination of 532-nm laser at a fluence of 0.5 nW/μm^2 with a beam spot diameter of ~ 720 nm and a scan step of 150 nm). Positive bias means that the tip of the nanowire is positive relative to the base; accordingly, positive current means that the electron flows from the base towards the tip. (c) Photocurrent vs voltage on a log–log scale. The photocurrent data is extracted from the data in (a) at the position of ~ 7.7 μm (undoped section).

The I-V characteristics for the n^+-i-n^+ nanowire device are plotted in Figure 7.9(b). For the case of positive bias, the photocurrent increases with increasing bias voltage and can be described by three different carrier-transport regimes: (I) a linear behaviour at the very low voltage region, obeying Ohm's law; (II) an exponential behaviour at the medium voltage region, commonly occurring in the wide band gap p-n diodes due to a recombination tunnelling mechanism [16, 17]; and (III) a power-law behaviour at the high voltage region, resulting from space-charge-limited current [18]. The observation of the three regions indicates the presence of a typical Schottky barrier under positive bias in the device. For the case of negative bias, only one behaviour is observed: the photocurrent increases following a linear relationship, suggesting a very low Schottky barrier (hence a quasi-Ohmic contact) in the device under negative bias. The different barrier heights under positive and negative bias in the device can be ascribed to the difference in doping levels at the tip and the base of the n^+-i-n^+ InP nanowire. The contact at the base may be responsible for the higher barrier as it has lower doping

concentration (see Figure 7.6(c)). The imperfect Ohmic contacts for the n^+-i-n^+ nanowire devices indicate that there is still room for further growth optimisation. Nevertheless, both contact barrier heights in the n^+-i-n^+ device are already significantly reduced through such contact doping, since the n^+-i-n^+ InP nanowire device shows a much higher photo-response than the undoped nanowire device under the same measurement conditions (see Figures 7.6(c) and (d)).

7.2.5 Temperature-Dependent Photocurrent Spectrum

To study the influence of temperature on the spectral performance of the n^+-i-n^+ InP single nanowire device, temperature-dependent photocurrent spectrum measurements (at a bias of 0.1V) were performed and the results are displayed in Figure 7.10(a). The photocurrent spectra of the n^+-i-n^+ single InP nanowire device were measured under illumination of a while light source (halogen lamp) dispersed by a standard monochromator. The monochromatic light was normalised and its intensity was 0.17 nW/μm^2. The measured photocurrent spectra (calibrated against a standard Si photodiode) show a broad photo-response with a cut-off wavelength at ~ 876 nm (at room temperature), which matches well with the WZ InP band gap. A clear blue shift of the cut-off wavelength is observed in photocurrent spectra with decreasing temperature, which could be attributed to the blue shift of band gaps of the n^+-i-n^+ InP nanowire with temperature. By extracting the 50% long wavelength cut-off at each temperature, the temperature-dependent band-gap enegry of the n^+-i-n^+ single InP nanowire was obtained, which follows well with the Varshni's relation [19] (that is the band-gap energy of a semiconductor versus temperature relationship) as shown in Figure 7.10(b), again confirming the WZ structure of InP nanowires. The reduction in photocurrent intensity with decreasing temperature may be explained on the basis of trapping centres associated with native (point) defects in the n^+-i-n^+ InP nanowire. It is noted that the photocurrent can still be measurable at 77 K, confirming the high contact quality in the n^+-i-n^+ nanowire device allowing an operation at low temperature (77 K) and low applied voltage (0.1 V).

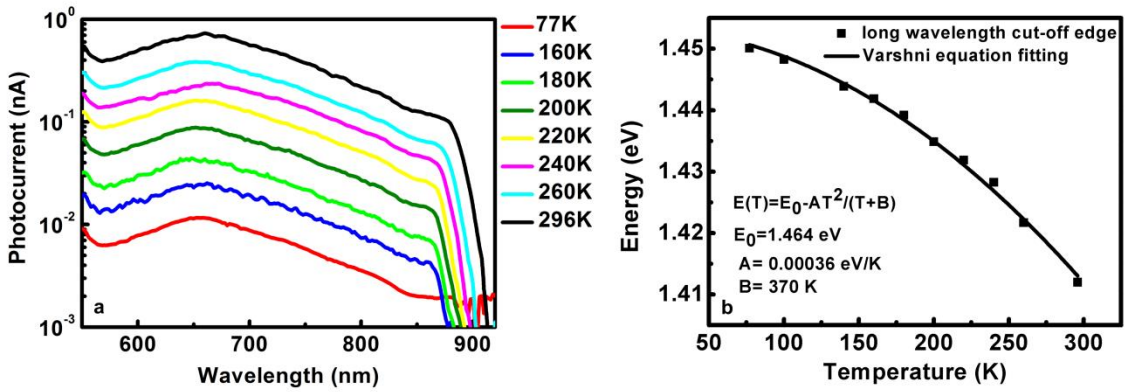

Figure 7.10: (a) Photocurrent spectra measured from an n^+-i-n^+ InP single nanowire device at temperatures ranging from 77 to 296 K . (b) Variation of the band-gap energy as a function of temperature of the n^+-i-n^+ InP single nanowire obtained from (a).

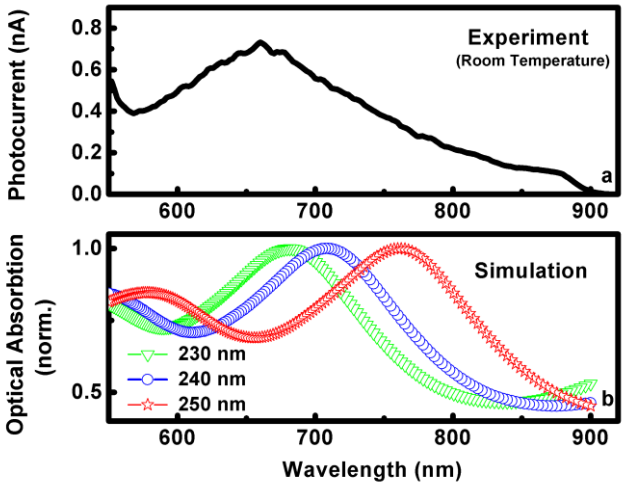

Figure 7.11: (a) Room-temperature photocurrent spectrum of an n^+-i-n^+ InP single nanowire. (b) Simulated optical absorption spectra of a single InP nanowire with a diameter of 230 nm (green), 240 nm (blue) and 250 nm (red) with resonant absorption peaks at 670, 710 and 760 nm, respectively. Absorption is normalised to incident source power.

A photocurrent peak at ~ 660 nm is observed in the spectrum (Figure 7.11(a)), and upon investigation of the resonant absorption cross-section in the single InP nanowire using finite-difference time-domain simulations, shows that it arises from the geometrical resonance effect (see Figures 7.11(b)). This simulation work was performed by a collaborator, Dr. Sudha

Mokkapati. The value of responsivity of the n^+-i-n^+ InP single nanowire device is calculated from the (room-temperature) photocurrent spectrum and found to be ~ 1.95 A/W at this resonant peak (see reference [20] for calculation details), which is comparable with the planar photodetectors [21, 22]. By increasing the nanowire diameter, the simulation results show that the resonant photocurrent peak is red shifted. Considering a femtosecond laser with centre wavelength of 800 nm is used in this work for THz measurements, single InP nanowires with diameter of 250 ~ 260 nm may be of better choices in the future to maximise the photo-absorption and further enhance the detection sensitivity.

7.3 Terahertz Measurements

7.3.1 Optical Pump-Terahertz Probe Spectroscopy

The photoconductivity lifetime and carrier mobility of an ensemble of n^+-i-n^+ InP nanowires were characterised using time-domain optical pump-THz probe (OPTP) spectroscopy [23, 24], as they have been shown in previous chapters as crucial for the material evaluation for photoconductive THz detection. The photoconductivity lifetime determines the signal processing technique and noise level in the detector while the carrier mobility determines its response level [25, 26]. It is found that the incorporation of n^+ sections in the InP nanowires has a small influence on the original material conductivity properties (see Figure 7.12). Photoconductivity lifetime of ~ 1.91 ns was obtained for n^+-i-n^+ nanowires, comparable with ~ 1.71 ns measured for the undoped ones. The electron mobility for n^+-i-n^+ InP nanowires was found to be approximately 950 ± 560 $cm^2 V^{-1}s^{-1}$, also comparable with 1260 ± 320 $cm^2 V^{-1} s^{-1}$ measured for the undoped InP nanowires. The differences in both photoconductivity lifetime and electron mobility could be due to the increased ionised impurity scattering in doped nanowires [27]. Despite that, it is still indicated that a high material quality is maintained in the doped nanowires.

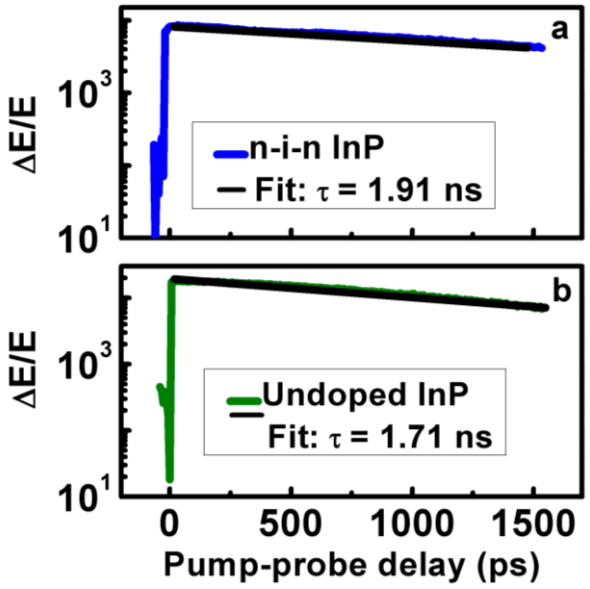

Figure 7.12: OPTP photoconductivity decays of (a) n^+-i-n^+ and (b) undoped InP nanowires.

7.3.2 Terahertz Detector Performance

Finally, the single nanowire THz detectors fabricated from n^+-i-n^+ InP nanowires were incorporated into a standard THz time-domain spectroscopy (THz-TDS) system (see Section 3.4.4) for characterisation. Figure 7.13 shows typical THz response obtained from an n^+-i-n^+ InP single nanowire detector, in comparison with an undoped InP single nanowire detector and a traditional (bulk) ion-implanted InP detector in the THz-TDS system, with the same strip-line electrode geometry. The n^+-i-n^+ nanowire detector shows a broad detection bandwidth in a range of 0.1-2.2 THz with good sensitivity and low noise level, similar to those of the undoped nanowire detector and the traditional bulk detector. As a demonstration, the n^+-i-n^+ nanowire detectors were also used to measure the refractive index (Figure 7.14(a)) and absorption coefficient (Figure 7.14(b)) of paper cards over the range from 0.5 to 1.5 THz in the THz-TDS system. The measured values using the n^+-i-n^+ nanowire detector are in good agreements with the literatures [30, 31] and those obtained using a conventional (bulk ion-implanted InP) THz detectors [24], again demonstrating the practicality of these n^+-i-n^+ InP single nanowire THz detectors.

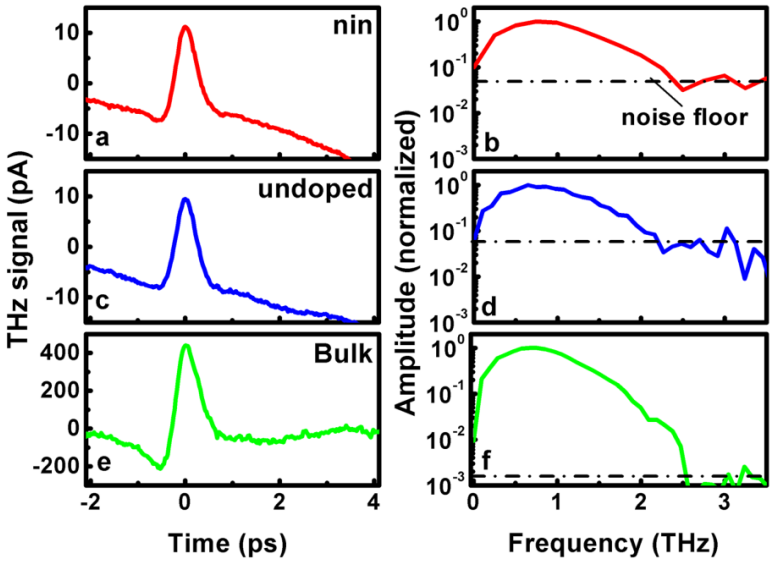

Figure 7.13: THz responses measured from a typical n^+-i-n^+ InP single nanowire detector (red), undoped InP single-nanowire detector (blue) and a traditional ion-implanted InP receiver (green) in a THz-TDS system. Left: unprocessed THz-induced current. Right: calculated amplitude spectrum.

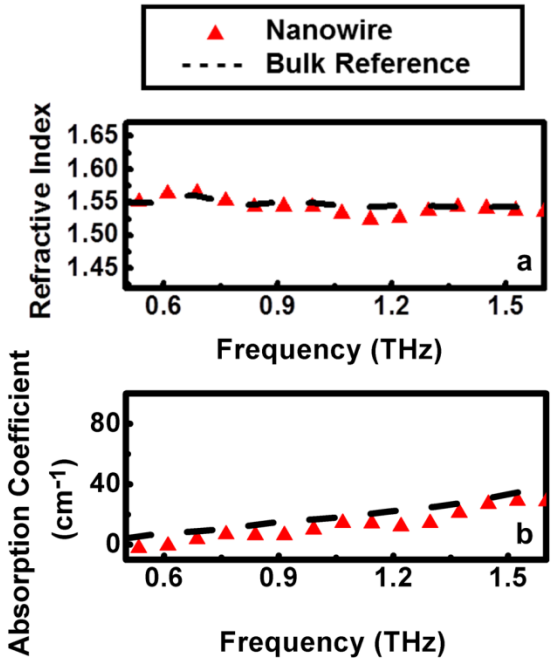

Figure 7.14: (a) Refractive index and (b) absorption coefficient spectra of a paper card obtained by characterisation in a THz-TDS system using an n^+-i-n^+ InP nanowire detector and a traditional bulk detector.

Table 7.1 displays a detailed comparison of device performance among the undoped InP single nanowire THz detector, n^+-i-n^+ InP single nanowire THz detector and traditional ion-implanted bulk InP THz receiver. The response spectral bandwidths of the three types of THz detectors are comparable however with some marginal differences (traditional detector ≳ n^+-i-n^+ nanowire detector ≳ undoped nanowire detector). Since the factors (such as laser pulse duration, bandwidth of THz source and electrode geometry [24]) which most strongly influence the detected bandwidth are kept the same for all detectors, the difference in the detected bandwidths for the three detectors can be mainly attributed to the difference in their noise floor level and signal-to-noise ratio (SNR) [26]. As a direct result of the improved contact quality, the n^+-i-n^+ nanowire detector shows a lower noise floor compared to the undoped nanowire detector, and thus exhibits an improved response bandwidth. The SNR of the n^+-i-n^+ nanowire detector increases by a factor of 2.5 to a value of 53 compared to the value of 21 of the undoped nanowire detector leading to a slightly broadened bandwidth (2.2 THz). Despite a significant difference in detection material volumes between the nanowire and bulk detector leads to a limited THz response current for the nanowire detectors (a few tens of pA), the n^+-i-n^+ nanowire detector still shows a comparable SNR to that of the bulk detector, indicating that doping engineering is an effective and promising tool for optimisation of single nanowire THz electronics.

Table 7.1: A comparison of device performance between InP nanowire detector and traditional ion-implanted InP photoconductive receiver.

Detector Type / **Performance**	**Photoconductive Antenna (strip lines)**		
	InP Single Nanowire		**InP Bulk**
	Undoped	**n-i-n**	**ion-implanted**
Detection Bandwidth (THz)	2	2.2	2.5
Signal-to-Noise Ratio	21	53	70
THz Induced Current (pA)	19.5	19.1	676.6

It is anticipated that further improvements in detector performance can be achieved through increasing the doping concentration in the n^+ section to achieve better Ohmic contacts to lower the noise, as well as performing a careful calibration of growth for producing a longer i section in the nanowire to increase the THz response current. It is interesting to note that the peak value of the THz response current obtained for the n^+-i-n^+ nanowire detector is very close to that of the undoped nanowire detector; this is given the difference observed in direct-current (DC) photocurrent measurements (see Figure 7.7(c) and (d)). Unlike the DC photocurrent measurement in this work, which requires an external bias (to produce a voltage drop across the contacts of device) to drive the photo-generated electron-hole pairs to form a current, the photoconductive detector for THz measurement requires no external bias to be applied for operation. The incident THz electric field couples into the detector and acts as an ultrashort alternating-current (AC) bias to drive the photo-generated carriers to the contacts. For the former case, the response current is strongly dependent on its contact quality, as non-Ohmic contact introduces a parasitic resistance to the current flow. For the latter, the photo-excited carrier density in the detection material determines the current flow, as THz electric field is distributed uniformly inside the detector and drives the current directly without voltage loss (in the contacts). However, it is important to achieve two Ohmic contacts in photoconductive THz detector, as Schottky contacts have been shown to lead to a THz rectification behaviour [30]. It has been known that rectification is highly non-linear, which can amplify small variations such as pulse-to-pulse or scan-to-scan noise, whereas Ohmic contacts are inherently linear leading to a more stable and accurate current response of the detector and thus higher SNR and detection sensitivity. This explains why the n^+-i-n^+ nanowire detector shows an improved SNR while having a comparable response current level to the undoped detector, as they possess a similar detection material volume but different contact quality. It is worth mentioning that, the photoconductive detector may be further modified for use as a photoconductive emitter (to generate THz radiation) in a THz-TDS system. However, photoconductive THz generation is in a sense an opposite process to photoconductive detection, in which an externally applied DC bias is required for operation. The external bias field distribution inside the emitter with Schottky contact electrodes will be localised close to the contacts, which may largely limit the THz emission efficiency. Therefore, forming Ohmic contacts is not only important for

photoconductive THz detectors but also essential for development of photoconductive THz emitters with low voltage [31] operation and high output powers. With both high-performance THz single nanowire detectors and emitters (to be developed in the future), more advanced THz-TDS systems [32, 33] can be realised.

7.4 Summary

In this chapter, n^+-i-n^+ nanowire structure was proposed to achieve photoconductive detectors with low contact resistance for highly sensitive THz detection. A novel and simple optical technique was used to profile the doping concentration along the nanowire for design and growth optimisation of the n^+-i-n^+ InP nanowire structure, leading to significant improvement of SNR of the device performance, comparable to traditional bulk THz detectors. The excellent detecting capability of n^+-i-n^+ InP single nanowire THz detectors further prove the suitability of III-V nanowires for application in THz-TDS systems. It is anticipated that such n^+-i-n^+ nanowire design could help address the common issues for nanowire-based devices including wire-to-wire variation and device-to-device variation for improved device reproducibility and reliability, and bring the promise of nanowire THz electronics closer to industrial applications. Moreover, the doping design used in this chapter may be also applicable for highly-efficient single nanowire photoconductive emitters, leading to development of more advanced nanowire-based THz systems for a broad range of applications.

References

[1] W. Shi, L. Hou, and X. Wang, "High effective terahertz radiation from semi-insulating-GaAs photoconductive antennas with ohmic contact electrodes," *Journal of Applied Physics*, vol. 110, 023111, 2011.

[2] M. Mikulics, M. Marso, S. Wu, A. Fox, M. Lepsa, D. Grutzmacher, R. Sobolewski, and P. Kordos, " Sensitivity enhancement of metal-semiconductor-metal photodetectors on Low-temperature grown GaAs using alloyed contacts," *IEEE*

photonics technology letters, vol. 20, pp. 1054-1056, 2008.

[3] A. Baca, F. Ren, J. Zolper, R. Briggs, and S. Pearton, "A survey of ohmic contacts to III-V compound semiconductors," *Thin Solid Films*, vol. 308, pp. 599-606, 1997.

[4] N. Vieweg, M. Mikulics, M. Scheller, K. Ezdi, R. Wilk, H.-W. Hübers, and M. Koch, "Impact of the contact metallization on the performance of photoconductive THz antennas," *Optics Express*, vol. 16, pp. 19695-19705, 2008.

[5] H. J. Yu, L. McCarthy, H. Xing, H. Waltereit, L. Shen, S. Keller, S. P. Denbaars, J. S. Speck, and U. K. Mishra, "Dopant activation and ultralow resistance Ohmic contacts to Si-ion-implanted GaN using pressurized rapid thermal annealing," *Applied Physics Letters*, vol. 85, pp. 5254-5256, 2004.

[6] N. Zamdmer, Q. Hu, K. A. McIntosh, and S. Verghese, "Increase in response time of low-temperature-grown GaAs photoconductive switches at high voltage bias," *Applied Physics Letters*, vol. 75, pp. 2313-2315, 1999.

[7] M. Mikulics, S. Wu, M. Marso, R. Adam, A. Forster, A. Van Der Hart, P. Kordos, H. Luth, and R. Sobolewski, "Ultrafast and highly sensitive photodetectors with recessed electrodes fabricated on low-temperature-grown GaAs," *IEEE photonics technology letters*, vol. 18, pp. 820-822, 2006.

[8] F. Wang, Q. Gao, K. Peng, Z. Li, Z. Y. Li, Y. N. Guo, L. Fu, L. M. Smith, H. H. Tan, and C. Jagadish, "Spatially resolved doping concentration and nonradiative lifetime profiles in single Si-doped InP nanowires using photoluminescence mapping," *Nano Letters*, vol. 15, pp. 3017-3023, 2015.

[9] Q. Gao, D. Saxena, F. Wang, L. Fu, S. Mokkapati, Y. A. Guo, L. Li, J. Wong-Leung, P. Caroff, H. H. Tan, and C. Jagadish, "Selective-area epitaxy of pure wurtzite InP nanowires: High quantum efficiency and room-temperature lasing," *Nano Letters*, vol. 14, pp. 5206-5211, 2014.

[10] T. Yoshikazu, A. Soichiro, N. Susumu, and S. Akio, "Characterization of InP grown by MOVPE using tertiary-butylphosphine for the phosphorous source," *Japanese Journal of Applied Physics*, vol. 29, pp. 11-18, 1990.

[11] L. Rigutti, A. D. Bugallo, M. Tchernycheva, G. Jacopin, F. H. Julien, G. Cirlin, G. Patriarche, D. Lucot, L. Travers, and J. C. Harmand, "Si incorporation in InP

nanowires grown by Au-Assisted molecular beam epitaxy," *Journal of Nanomaterials*, 435451, 2009.

[12] M. B. Heaney, "Electrical conductivity and resistivity," *The measurement, instrumentation and sensors handbook*, pp. 1332-1345, 2000.

[13] M. Bugajski and W. Lewandowski, "Concentration-dependent absorption and photoluminescence of n-type InP," *Journal of Applied Physics*, vol. 57, pp. 521-530, 1985.

[14] Q. Gao, V. G. Dubrovskii, P. Caroff, J. Wong-Leung, L. Li, Y. Guo, L. Fu, H. H. Tan, and C. Jagadish, "Simultaneous selective-area and vapor-liquid-solid growth of InP nanowire arrays," *Nano Letters*, vol. 16, pp. 4361-4367, 2016.

[15] W. Walukiewicz, J. Lagowski, L. Jastrzebski, P. Rava, M. Lichtensteiger, C. Gatos, and H. Gatos, "Electron mobility and free-carrier absorption in InP; determination of the compensation ratio," *Journal of Applied Physics*, vol. 51, pp. 2659-2668, 1980.

[16] J. B. Fedison, T. P. Chow, H. Lu, and I. B. Bhat, "Electrical characteristics of magnesium-doped gallium nitride junction diodes," *Applied Physics Letters*, vol. 72, pp. 2841-2843, 1998.

[17] M. Kumar, T. N. Bhat, M. K. Rajpalke, B. Roul, A. T. Kalghatgi, and S. B. Krupanidhi, "Transport and infrared photoresponse properties of InN nanorods/Si heterojunction," *Nanoscale Research Letters*, vol. 6, 609, 2011.

[18] R. Ghosh and D. Basak, "Electrical and ultraviolet photoresponse properties of quasialigned ZnO nanowires/p-Si heterojunction," *Applied Physics Letters*, vol. 90, 243106, 2007.

[19] K. P. Odonnell and X. Chen, "Temperature-dependence of semiconductor band-gaps," *Applied Physics Letters*, vol. 58, pp. 2924-2926, 1991.

[20] L. Ziyuan, Y. Xiaoming, F. Lan, P. Kun, W. Fan, F. Xiao, C. Philippe, P. W. Thomas, T. Hark Hoe, and J. Chennupati, "Room temperature GaAsSb single nanowire infrared photodetectors," *Nanotechnology*, vol. 26, 445202, 2015.

[21] A. Beling and J. C. Campbell, "InP-based high-speed photodetectors," *Journal of Lightwave Technology*, vol. 27, pp. 343-355, 2009.

[22] P. S. Shaw, T. C. Larason, R. Gupta, S. W. Brown, and K. R. Lykke, "Improved

near-infrared spectral responsivity scale," *Journal of Research of the National Institute of Standards and Technology,* vol. 105, pp. 689-700, 2000.

[23] K. Peng, P. Parkinson, L. Fu, Q. Gao, N. Jiang, Y.-N. Guo, F. Wang, H. J. Joyce, J. L. Boland, H. H. Tan, C. Jagadish, and M. B. Johnston, "Single nanowire photoconductive terahertz detectors," *Nano Letters,* vol. 15, pp. 206-210, 2015.

[24] K. Peng, P. Parkinson, J. L. Boland, Q. Gao, Y. C. Wenas, C. L. Davies, Z. Li, L. Fu, M. B. Johnston, H. H. Tan, and C. Jagadish, "Broadband phase-sensitive single InP nanowire photoconductive terahertz detectors," *Nano Letters,* vol. 16, pp. 4925-4931, 2016.

[25] E. Castro-Camus, J. Lloyd-Hughes, L. Fu, H. H. Tan, C. Jagadish, and M. B. Johnston, "An ion-implanted InP receiver for polarization resolved terahertz spectroscopy," *Optics Express,* vol. 15, pp. 7047-7057, 2007.

[26] E. Castro-Camus, L. Fu, J. Lloyd-Hughes, H. H. Tan, C. Jagadish, and M. B. Johnston, "Photoconductive response correction for detectors of terahertz radiation," *Journal of Applied Physics,* vol. 104, 053113, 2008.

[27] J. L. Boland, A. Casadei, G. z. Tütüncüoglu, F. Matteini, C. L. Davies, F. Jabeen, H. J. Joyce, L. M. Herz, A. Fontcuberta i Morral, and M. B. Johnston, "Increased photoconductivity lifetime in GaAs nanowires by controlled n-Type and p-Type doping," *ACS nano,* vol. 10, pp. 4219-4227, 2016.

[28] T. Hattori, H. Kumon, and H. Tamazumi, "Terahertz spectroscopic characterization of paper," *35th International Conference on Infrared, Millimeter, and Terahertz Waves (Irmmw-Thz 2010),* pp. 1-2, 2010.

[29] B. Hussain, M. Nawaz, M. Ahmed, and M. Y. A. Raja, "Measurement of thickness and refractive index using femtosecond and terahertz pulses," *Laser Physics Letters,* vol. 10, 055301, 2013.

[30] C. T. Que, M. Tani, F. Miyamaru, and M. Hangyo, "Detection of THz radiation with Schottky photoconductive antenna," in *2005 Joint 30th International Conference on Infrared and Millimeter Waves and 13th International Conference on Terahertz Electronics*, vol. 2, pp. 628-629, 2005.

[31] J.-K. Sheu, J. Tsai, S.-C. Shei, W.-C. Lai, T.-C. Wen, C. Kou, Y.-K. Su, S.-J. Chang,

and G.-C. Chi, "Low-operation voltage of InGaN-GaN light-emitting diodes with Si-doped $In_{0.3}Ga_{0.7}N$/GaN short-period superlattice tunneling contact layer," *IEEE Electron device letters,* vol. 22, pp. 460-462, 2001.

[32] C. Wood, J. Cunningham, I. Hunter, P. Tosch, E. Linfield, and A. Davies, "On-chip pulsed terahertz systems and their applications," *International journal of infrared and millimeter waves,* vol. 27, pp. 557-569, 2006.

[33] J. Cunningham, M. Byrne, C. Wood, and L. Dazhang, "On-chip terahertz systems for spectroscopy and imaging," *Electronics Letters,* vol. 46, pp. s34-s37, 2010.

Chapter 8

Conclusions and Future Work

8.1 Conclusions

Terahertz time-domain spectroscopy (THz-TDS) systems with reduced size, higher level of integration and improved performance (i.e. nanoscale resolution and broadband spectroscopic detection) are highly desirable for numerous applications spanning the fields across homeland security, pharmaceuticals, environmental control, medical diagnostic and fundamental science. THz electronics based on semiconductor nanowires are considered as ideal sub-wavelength elements for design of such advanced THz systems. This dissertation has successfully demonstrated photoconductive THz detectors based on III-V semiconductor single nanowires for use in THz-TDS, showing a great promise for development of future advanced nanowire-based THz-TDS systems. Nano-detector design, fabrication, characterisation and related optical simulations were employed to provide a deep insight into the characteristics of the single nanowire detectors for guidance of future work.

Firstly, in Chapter 4 GaAs/AlGaAs core-shell single nanowires were studied and fabricated into microscopic detectors to detect the pulsed THz signal in a THz-TDS system via photoconductive switching technique. In order to obtain the sufficient response level while having the minimal noise, ultrashort charge carrier lifetime and high carrier mobility in the detection material are required. It has been found that the carrier lifetime and carrier mobility in GaAs nanowires can be tuned through a careful control of the crystal quality and surface passivation via AlGaAs shell growth. Therefore, by adjusting growth parameters, nanowire core diameter and shell thickness, a series of GaAs/AlGaAs core-shell nanowires was grown by metalorganic vapour phase epitaxy (MOVPE) via Au-catalysed vapour-liquid-solid (VLS) mechanism. These GaAs/AlGaAs nanowires were characterised, compared, selected and fabricated into single nanowire detectors and incorporated into a THz-TDS system. The GaAs/AlGaAs single nanowire THz detectors all produced good THz responses however with

narrow bandwidth of ~ 0.6 THz. Finite-difference time-domain (FDTD) simulations were carried out revealing the origin of the limited bandwidth of the GaAs/AlGaAs single nanowire THz detectors, which can be attributed to the resonant characteristics of device geometry (electrode/antenna design) to THz radiation.

The relationship between device (electrode) geometry and its resonant characteristics in THz regime was subsequently studied in more details via FDTD simulations in Chapter 5. The tunability of the resonant frequency range resulting from electrode (antenna) design, may lead to more potential applications for THz devices, for example, THz amplitude modulator/switches and tunable bandwidth THz emitter/detectors. As a result of detector geometry optimisation, GaAs/AlGaAs single nanowire photoconductive THz detectors with broad detection bandwidth ranging from 0.1 to 1.6 THz were achieved. Moreover, it is also found that the thin GaAs cap used to prevent the oxidation of AlGaAs shell in GaAs/AlGaAs nanowires plays a more important role (than expected) in the detector response performance, causing multiple sampling modes during detector operation. The major sampling mode is the integrating mode dominated by the GaAs core and the minor sampling mode is the direct sampling mode dominated by the GaAs capping layer. Additionally, it is also noted that the nano-size detection material volume (a single nanowire in this work) combined with an insulating substrate (quartz) greatly reduces the noise current in the single nanowire detector, resulting in a relaxed requirement on the material properties (i.e. an ultra-short carrier lifetime) for THz detection. As such, other III-V nanowire systems can be chosen for photoconductive THz detection.

A follow-up study on photoconductive THz detectors developed from single InP nanowires was described in Chapter 6. These InP nanowires were grown using selective-area metalorganic vapour phase epitaxy (SA-MOVPE) technique. Compared to the Au-catalysed VLS growth used for producing GaAs/AlGaAs nanowires, the SA-MOVPE growth are capable of producing semiconductor nanowires with improved structural and crystallographic uniformity and thus superior optoelectronic properties, while eliminating the potential metal catalyst contamination in nanowires. Pure wurtzite and stacking fault-free InP nanowires were synthesised in this work. The core-only InP nanowires have high photosensitivity due to suppressed non-radiative recombination originating from their intrinsically low surface

recombination velocity. As a result, broadband (0.1-2.0 THz) InP single nanowire THz detectors with high sensitivity were demonstrated. These detectors were shown to be able to produce high-quality time-domain spectra for real material characterisation in the THz-TDS system. Furthermore, the response characteristics of the InP single nanowire photoconductive THz detectors perfectly matched the simulation results, and were found to not only have a low-noise nature but also a long time-domain sampling window compared to the traditional (bulk) THz photoconduction detectors, all of which are beneficial for achieving higher spectral resolutions in THz-TDS.

A further improvement of the InP single nanowire photoconductive detector was achieved in Chapter 7 by implementing an axially doped n^+-i-n^+ nanowire structure to minimise the contact resistances through the introduction of contact doping. In order to grow the appropriate n^+-i-n^+ nanowire structure, undoped InP nanowires and a series of uniformly-Si-doped (n-type) InP nanowires with different doping concentration were investigated to examine the relationship between nanowire growth, doping characteristics and resultant device contact quality. It is noted that effective characterisation of spatially varying carrier concentrations in a single nanowire has been highly challenging due to the small volumes of material involved. As such, a simple all-optical technique (combining both power-dependent photoluminescence and time-resolved photoluminescence measurements to profile the doping concentration along the length of single nanowires) was employed to measure the local carrier density with diffraction-limited resolution. By correlating these optical measurements with 2- and 4-terminal current-voltage (I-V) measurements, axial n^+-i-n^+ InP nanowires were then designed and synthesised. The n^+-i-n^+ InP nanowires were characterised using the optical microscopy technique for axial doping profiling to confirm the electrical contact design. Finally, the as-fabricated n^+-i-n^+ InP single nanowire detectors were incorporated in a THz-TDS system and their performance was compared with the undoped nanowire detectors. The n^+-i-n^+ InP single nanowire detectors are shown to be superior to undoped nanowire detectors for use in THz-TDS, with a significantly enhancement in device performance including an increased detection bandwidth and a 2.5 increased signal-to-noise ratio. Despite having only a nano-size active volume (and hence a pA-level response current), the n^+-i-n^+ nanowire detector performs comparably to the conventional bulk InP THz detectors, exhibiting a great potential for future

implementation in advanced THz systems.

8.2 Future Work

As clearly demonstrated by this thesis, III-V semiconductor nanowires such as GaAs and InP nanowires combined with proper detector geometry design are highly suitable for THz spectroscopy and imaging applications with high spectral and spatial resolution. The next step is to further employ these single nanowire detectors with new device/system designs for more advanced applications, including:

- A compact THz-TDS system by coupling a fibre laser system with a single nanowire THz detector
- An integrated two-single-nanowire based polarisation-sensitive THz detectors,
- Single nanowire based on-chip THz spectrometer.

8.2.1 Fibre-Coupled Terahertz Time-Domain Spectroscopy System

Commonly, a mode-locked Ti: Sapphire laser [1] is used in THz-TDS, which allows for production of femtosecond laser pulses at around 800 nm wavelength to photo-excite the THz emitter and detector. However, this type of solid state laser is bulky, costly and inconvenient for integrating into a compact THz system. In recent years, mode-locked femtosecond fibre lasers [2, 3] have been well developed, which have many advantages such as compact size, low cost and high efficiency. This type of laser has been proven suitable as optical source to be incorporated into THz-TDS systems, which allows for a reduction in the number of expensive optical components for system building, large cost reduction and ease of optical alignment while minimising the influences of external disturbances in measurement. The implementation of single nanowire devices in such a fibre-coupled THz-TDS system may result in the most compact THz system.

Currently, high-intensity mode-locked femtosecond fibre lasers are commercially available operating at 780 nm ~ 1.56 μm wavelength bands [4]. Among these, the 1.3 μm and 1.5 μm

femtosecond fibre lasers [5, 6] are considered as the most promising optical sources to develop fibre-coupled THz-TDS systems, owing to their low manufacturing cost and low loss for silica fibre. In order to realise such nanowire-based fibre-coupled THz-TDS system, new III-V nanowire systems are required, whose band gap should match the operating wavelength of 1.3 or 1.5 μm (to maximise the photon-to-carrier generation efficiency). III-V ternary semiconductor nanowires with tunable band gap (from ultraviolet to mid/far infrared range by adjusting their alloy composition), are strongly suggested as candidates for use in optical fibre-coupled THz-TDS. Bulk $In_xGa_{1-x}As$ photodetectors [7, 8] have been shown to offer a broadband response from 900 nm to 2.6 μm, and successfully used in fibre-coupled THz-TDS systems [9]. Accordingly, $In_xGa_{1-x}As$ single nanowire detectors could also be suited for use in fibre-coupled THz-TDS systems. A project regarding the growth study of $In_xGa_{1-x}As$ nanowires is being conducted in the Australian National University group. Figure 8.1(a) shows that structurally-uniform $In_xGa_{1-x}As$ nanowires have been achieved [10]. These $In_xGa_{1-x}As$ nanowires were fabricated into single nanowire detectors for basic electrical characterisation, showing a good photo-response and low dark current (see Figure 8.1(b)), which are desirable for low-noise photoconductive detection. A precise composition control of these $In_xGa_{1-x}As$ nanowires for the required band gap (for operational wavelength at 1.3 or 1.5 μm) remains challenging. However it is worth pushing further to develop $In_xGa_{1-x}As$ nanowires to realise nanowire-based fibre-coupled THz-TDS systems.

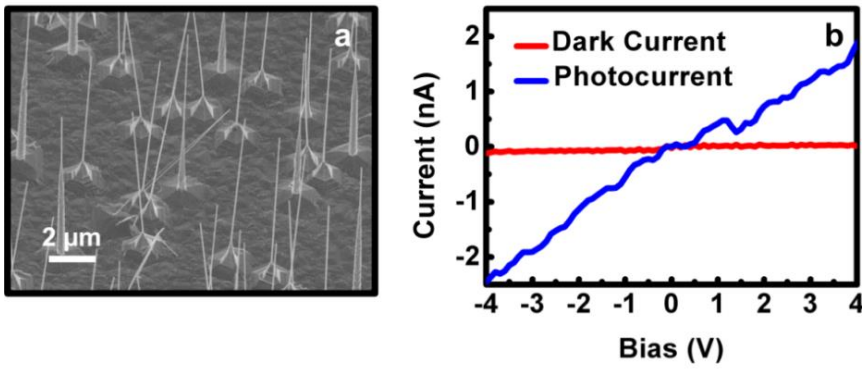

Figure 8.1: (a) A scanning-electron-microscopy image of the as-grown InGaAs nanowires. (b) Dark/photocurrent I-V characteristics of a single InGaAs nanowire device (under the excitation of a pulsed green laser).

8.2.2 Polarisation-Resolved Terahertz Detection

In addition to the capability of characterising complex optical constants of a material [11, 12], polarisation states of the THz radiation can also be probed using THz-TDS [13-15], and thus allow characterisation of the anisotropic properties of the material [16] (i.e. birefringence and optical activity). The anisotropic characteristics of a material are affected by many factors, including surface topography, crystal structure, stress and magnetic fields. Hence polarisation-sensitive THz-TDS measurements can offer a more thorough understanding of those important material properties.

At present, polarisation detection in THz-TDS can be realised using THz polarisers[17] (which have low sensitivity and limited bandwidth) or using polarisation-sensitive detectors (such as electro-optic crystal detector [18] or multi-pole photoconductive detectors [13, 19, 20]). Amongst them, multi-pole photoconductive detectors (see Figure 8.2) stand out due to their high sensitivity and angular resolution [21]. Multi-pole photoconductive detectors are capable of simultaneously measuring the electric field (phase and amplitude) and polarisation state of a THz pulse through a single time-domain scan in THz-TDS measurement. Figure 8.2 shows three different multi-pole photoconductive detectors that have been reported for polarisation-resolved THZ-TDS measurements.

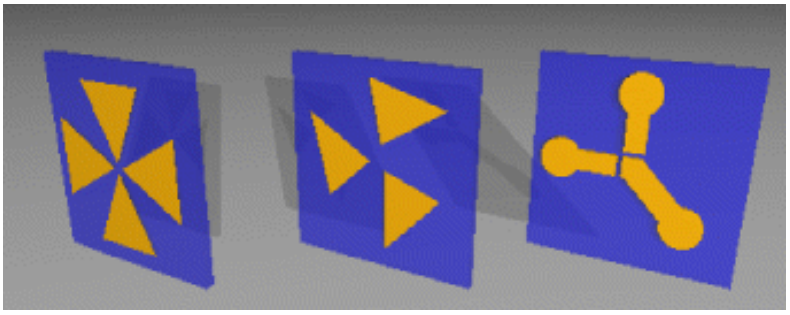

Figure 8.2: Three different polarisation-sensitive photoconductive detector designs (from Castro-Camus et al. [15]). From left to right designs published by Hussain et al. [20], Makabe et al. [13] and Castro-Camus et al. [19].

Taking advantages of their one-dimensional geometry, III-V semiconductor nanowires are more suitable for polarisation-resolved THz measurements. Single nanowire photoconductive THz detectors are intrinsically highly polarisation-sensitive detectors, which have proven to be able to measure one electric field component of the THz pulse with polarisation (only) parallel to nanowire axis (see Section 4.4.6). Simply, by rotating the nanowire detector, the other components of the THz pulse can be measured. In order to further improve the measurement accuracy while reducing data acquisition time, advanced polarisation-sensitive nanowire detector in combination of a multi-contact geometry (similar as the ones shown in Figure 8.2) can be explored. By fabricating a photoconductive detector using two crossed nanowires (preferably orthogonal) with multi-pole contacts, polarisation-sensitive nanowire detectors capable of simultaneously measuring two components of the THz pulse may be realised as the measured polarisation is confined by the axis of the two nanowires.

The main challenge for this work is device fabrication. On the one hand, precisely positioning nanowires and making them cross over each other with designated angle is difficult. In many published reports, the crossed nanowires were obtained by distributing them randomly. On the other hand, the two crossed nanowires must be electrically isolated from each other for device operation. A silicon oxide coating on the bottom nanowire or other methods could be used to realise such isolation, which will involve multiple fabrication steps. In addition, based on the feature size of the detector electrodes and the substrate (commonly z-cut quartz substrates for THz detection), device patterning technique (i.e. electron beam lithography and/or ultraviolet photolithography) need to be carefully chosen and implemented.

8.2.3 On-Chip Terahertz Spectrometer

The spatial resolution of a typical THz system is restricted by the wavelengths of generated THz waves (around several hundred micrometers, as 1 THz is equivalent to 300 μm), due to diffraction effects. A problem arises when the size or features of the target sample is far smaller than THz wavelengths involved. A sub-wavelength aperture or tip induced technique [22, 23] can overcome the diffraction limit in the near field, however, such methods significantly reduce the strength of the electric field measured and may induce a distortion of the waveform.

Another approach, in which the source or/and detector size is reduced to the sub-wavelength range, has been investigated, and 'on-chip THz system' was proposed [24, 25]. In 2010, Cunningham and colleagues published a review [26] to trace the history of on-chip THz systems. Their group built an integrated THz system with photoconductive emitter and detector coupled by a THz waveguide on a chip. In comparison with the free-space THz system, a piece of lactose was measured in both systems. The on-chip system, having one thousand times less interacting energy, showed comparable spectral sensitivity and frequency resolution. Further work based on a similar on-chip system achieved a good imaging (100 and 20 μm in x and y resolution, respectively) of a GaAs sample. It is anticipated that one-dimensional semiconductor nanowires could be potential candidates to build such on-chip THz systems. In 2012, Erhard and co-workers [27] reported the incorporation of a single InAs nanowire in an on-chip photocurrent pump-probe THz spectroscopy system for THz emission (based on photo-Dember effect [28]), as shown in Figure 8.3. A 200 nm-thick layer of ion implanted silicon was used for THz detection in this system. By replacing this silicon detector with a single nanowire detector (as developed in this thesis), nanowire-based integrated THz photonic system could be achieved. It is worth mentioning that the photoconductive THz antenna introduced in this thesis can work either as an emitter or a detector (see Section 2.3), dependent on the operation settings. As such, two single nanowire photoconductive antennas (one served as the emitter and the other as the detector) could be potentially coupled through a THz waveguide to form an on-chip THz-TDS spectrometer, similar to that in Cunningham's work.

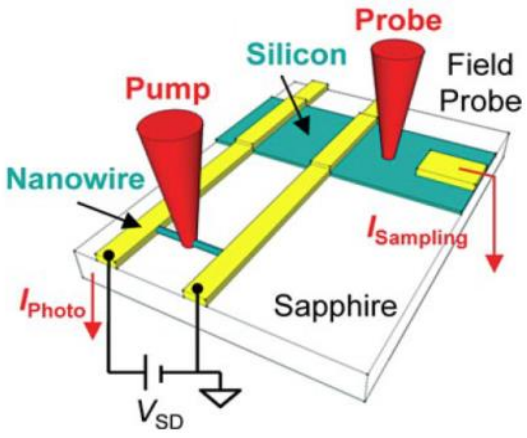

Figure 8.3 Schematic of a pump-probe circuit and device geometry of a single InAs nanowires THz emitter (from reference [27]).

The key challenges to realise such nanowire-based on-chip THz systems are (1) to develop THz waveguides for minimal transmission loss and dispersion, (2) to design/optimise both antenna (electrodes) structure and nanowire material system for high-intensity photoconductive THz emission and high-sensitivity detection, and (3) to design/optimise the system with good coupling efficiency between the THz emitter, waveguide and detector. As an important initial step for future work, modelling will be essential for the design of the waveguide and its coupling with the nanowire THz emitter and detector respectively. Additionally, array-based nanowire emitter or detector may be further explored to address single nanowire related low THz response issue and furthermore, to achieve nanowire-based THz emitter/detector integrated on-chip system.

8.3 Summary

This work has made considerable progress in the design, fabrication and development of photoconductive THz detectors based on III-V semiconductor single nanowires including GaAs/AlGaAs and InP nanowires. The nano-size nature of nanowire detectors with very little active material volume and the device being fabricated on insulating quartz substrate enables the detectors with low-noise, long time-delay sampling window and tunable detection bandwidth (which can be adjusted by using specific detector geometry design). It is anticipated that, with further advances in III–V nanowire growth, device geometry optimisation and device contact improvement, single nanowire detectors will become crucial nano-components for future advanced THz systems for applications such as nanostructured material characterisation or sub-wavelength imaging.

References

[1] C. Christov, *Biomolecular Spectroscopy: Advances from Integrating Experiments and Theory,* vol. 93: Elsevier, 2013.

[2] F. Ellrich, T. Weinland, D. Molter, J. Jonuscheit, and R. Beigang, "Compact

fiber-coupled terahertz spectroscopy system pumped at 800 nm wavelength," *Review of Scientific Instruments*, vol. 82, 053102, 2011.

[3] A. Barh, B. P. Pal, G. P. Agrawal, R. K. Varshney, and B. M. A. Rahman, "Specialty fibers for terahertz generation and transmission: A Review," *Ieee Journal of Selected Topics in Quantum Electronics*, vol. 22, pp. 365-379, 2016.

[4] W. Sibbett, A. Lagatsky, and C. Brown, "The development and application of femtosecond laser systems," *Optics Express*, vol. 20, pp. 6989-7001, 2012.

[5] M. Suzuki, K. Fujii, and M. Tonouchi, "THz-TDS systems for 1560-nm-wavelength-laser operation," *IRMMW-THz 2005: The Joint 30th International Conference on Infrared and Millimeter Waves and 13th International Conference on Terahertz Electronics*, Vols 1 and 2, pp. 251-252, 2005.

[6] Y. Yao, G. P. Agrawal, and W. H. Knox, "Yb: fiber laser-based, spectrally coherent and efficient generation of femtosecond 1.3-μm pulses from a fiber with two zero-dispersion wavelengths," *Optics Letters*, vol. 40, pp. 3631-3634, 2015.

[7] C. Nuese and G. Olsen, "Room-temperature heterojunction laser diodes of $In_xGa_{1-x}As/In_yGa_{1-y}P$ with emission wavelength between 0.9 and 1.15 μm," *Applied Physics Letters*, vol. 26, pp. 528-531, 1975.

[8] J. Kaniewski and J. Piotrowski, "InGaAs for infrared photodetectors: Physics and technology," *Opto-Electronics Review*, vol. 12, pp. 139-148, 2004.

[9] S.-P. Han, H. Ko, N. Kim, H.-C. Ryu, C. W. Lee, Y. A. Leem, D. Lee, M. Y. Jeon, S. K. Noh, and H. S. Chun, "Optical fiber-coupled InGaAs-based terahertz time–domain spectroscopy system," *Optics Letters*, vol. 36, pp. 3094-3096, 2011.

[10] A. S. Ameruddin, H. A. Fonseka, P. Caroff, J. Wong-Leung, R. L. O. het Veld, J. L. Boland, M. B. Johnston, H. H. Tan, and C. Jagadish, "$In_xGa_{1-x}As$ nanowires with uniform composition, pure wurtzite crystal phase and taper-free morphology," *Nanotechnology*, vol. 26, 205604, 2015.

[11] Y.-S. Jin, G.-J. Kim, and S.-G. Jeon, "Terahertz dielectric properties of polymers," *Journal of the Korean Physical Society*, vol. 49, pp. 513-517, 2006.

[12] Y.-S. Lee, *Principles of Terahertz Science and Technology*, vol. 170: Springer Science & Business Media, 2009.

[13] H. Makabe, Y. Hirota, M. Tani, and M. Hangyo, "Polarization state measurement of terahertz electromagnetic radiation by three-contact photoconductive antenna," *Optics Express*, vol. 15, pp. 11650-11657, 2007.

[14] H. Dong, Y. Gong, V. Paulose, and M. Hong, "Polarization state and Mueller matrix measurements in terahertz-time domain spectroscopy," *Optics Communications*, vol. 282, pp. 3671-3675, 2009.

[15] E. Castro-Camus, "Polarization-resolved terahertz time-domain spectroscopy," *Journal of Infrared, Millimeter, and Terahertz Waves*, vol. 33, pp. 418-430, 2012.

[16] J. Lloyd-Hughes, S. Jones, E. Castro-Camus, K. Doig, and J. MacManus-Driscoll, "Modifying the polarization state of terahertz radiation using anisotropic twin-domains in $LaAlO_3$," *Optics Letters*, vol. 39, pp. 1121-1124, 2014.

[17] F. Yan, C. Yu, H. Park, E. P. J. Parrott, and E. Pickwell-MacPherson, "Advances in polarizer technology for terahertz frequency applications," *Journal of Infrared, Millimeter, and Terahertz Waves*, vol. 34, pp. 489-499, 2013.

[18] N. Yasumatsu, A. Kasatani, K. Oguchi, and S. Watanabe, "High-speed terahertz time-domain polarimeter based on an electro-optic modulation technique," *Applied Physics Express*, vol. 7, 092401, 2014.

[19] E. Castro-Camus, J. Lloyd-Hughes, L. Fu, H. H. Tan, C. Jagadish, and M. B. Johnston, "An ion-implanted InP receiver for polarization resolved terahertz spectroscopy," *Optics Express*, vol. 15, pp. 7047-7057, 2007.

[20] A. Hussain and S. R. Andrews, "Ultrabroadband polarization analysis of terahertz pulses," *Optics Express*, vol. 16, pp. 7251-7257, 2008.

[21] C. M. Morris, R. V. Aguilar, A. V. Stier, and N. P. Armitage, "Polarization modulation time-domain terahertz polarimetry," *Optics Express*, vol. 20, pp. 12303-12317, 21 2012.

[22] A. Adam, "Review of near-field terahertz measurement methods and their applications," *Journal of Infrared, Millimeter, and Terahertz Waves*, vol. 32, pp. 976-1019, 2011.

[23] T. L. Cocker, V. Jelic, M. Gupta, S. J. Molesky, J. A. J. Burgess, G. De Los Reyes, L. V. Titova, Y. Y. Tsui, M. R. Freeman, and F. A. Hegmann, "An ultrafast terahertz scanning

tunnelling microscope," *Nature Photonics*, vol. 7, pp. 620-625, Aug 2013.

[24] C. Wood, J. Cunningham, I. Hunter, P. Tosch, E. Linfield, and A. Davies, "On-chip pulsed terahertz systems and their applications," *International journal of infrared and millimeter waves*, vol. 27, pp. 557-569, 2006.

[25] Y. Kawano and K. Ishibashi, "An on-chip near-field terahertz probe and detector," *Nat Photon*, vol. 2, pp. 618-621, 2008.

[26] J. Cunningham, M. Byrne, C. Wood, and L. Dazhang, "On-chip terahertz systems for spectroscopy and imaging," *Electronics Letters*, vol. 46, pp. s34-s37, 2010.

[27] N. Erhard, P. Seifert, L. Prechtel, S. Hertenberger, H. Karl, G. Abstreiter, G. Koblmüller, and A. W. Holleitner, "Ultrafast photocurrents and THz generation in single InAs-nanowires," *Annalen der Physik*, vol. 525, pp. 180-188, 2013.

[28] V. Apostolopoulos and M. Barnes, "THz emitters based on the photo-Dember effect," *Journal of Physics D: Applied Physics*, vol. 47, 374002, 2014.